Understanding the effect of aluminium on the microstructure on low level nitrogen steel

By

Yahya Palizdar

Submitted in accordance with the requirements for the degree of
Doctor of Philosophy

The University of Leeds

School of Process, Environmental and Materials Engineering

April 2011

The candidate confirms that the work submitted is his own and that appropriate credit has been given where reference has been made to the work of others.

The candidate confirms that the thesis is his own work, except where work which has formed part of jointly-authored publications has been included. The contribution of the candidate and the other authors has been indicated clearly below. The candidate confirms that appropriate credit has been given within the thesis where reference has been made to the work of others.

The details of chapters 3 (2 papers), 4 and 5 of the thesis are based on the following journals papers, respectively:

- Understanding the effect of aluminium on microstructure in low level nitrogen steels, MATERIALS SCIENCE AND TECHNOLOG, Palizdar, Y. Scott, A. J. Cochrane, R. C. Brydson, R; Volume: 25, Pages: 1243-1248

- The effect of deliberate aluminium additions on the microstructure of rolled steel plate characterized using EBSD; MATERIALS CHARACTERIZATION, Palizdar, Y. Cochrane, R. C. Brydson, R. Crowther, D. San Martin, D. Scott, A. J; Volume: 61, Pages: 159-167

- Influence of aluminum alloying and heating rate on austenite formation in low carbon-manganese steels, METALL MATER TRANS A, San Martín, D. Palizdar, Y. García-Mateo, C. Cochrane, R.C. Brydson, R. Scott ,A.J; in press

- Demonstration of elemental partitioning during austenite formation in low-carbon aluminium alloyed steel JOURNAL OF MATERIALS SCIENCE, Palizdar, Y. San Martin, D. Brown, A. P. Ward, M. Cochrane, R. C. Brydson, D. Scott, A. J; Volume 46, Number 7, Pages : 2384-2388

The candidate (Y. Palizdar) performed the main experimental, wrote the initial and final draft of the papers. The co-authors, Dr. Andrew Scott, Prof. Rik Brydson and Prof. Bob Cochran were supervised the entire project. The Co-authors Dr. David San Martin, Carlos García-Mateo and David Crowther contributed in some of the experimental works mainly carried out by dilatometer. The co-authors Dr. Andy Brown and Dr. Mike Ward helped in performing high resolution TEM.

To:

Baba Ali

Maman Noriyeh

Somayeh

Amir Hossein and Narges

Acknowledgments

I would like to take this opportunity to express my gratitude to Dr. A.J. Scott, Prof. R. Brydson and Prof. R.C. Cochrane my friends and supervisors for the support given during this project.

I would also like to acknowledge the valuable technical supports given during this PhD project by my friend Dr D. San Martin from CENIM-CSIC, Madrid and also Dr. D. Crowther from Corus.

Special thanks must go to my wife, Somayeh, for keeping me going through the difficult periods during my PhD project.

The biggest thank must go to my parent, Baba Ali and Maman Noriyeh, for giving me this opportunity to be able to go through different stages of my study and finally getting my PhD.

ABSTRACT

Aluminium has been used as a de-oxidant and grain refiner element for more than 100 years, however, the use of aluminium as a deliberate alloying addition in steels has attracted increased attention recently as a possible replacement for Si in Transformation Induced Plasticity (TRIP) steels. Although the effect of substitutional elements such as manganese and chromium has been investigated in detail in the last few decades, there has been little research concerned with the effect of Al as a substitutional element in steel in amounts higher than 0.1 wt%. This could be due to the previous lack of industrial interest and also technological concerns over the production of high Al-content steels.

Work was carried out on three low carbon (0.02 wt%) manganese (1.4 wt%) steels with very low levels of nitrogen (10 ppm) which have been alloyed with very different aluminium contents (0.02, 0.48 and 0.94 wt%). Electron back scatter diffraction (EBSD) was employed to study the effect of excess aluminium (apart from aluminium nitride) on the final ferritic microstructure. In order to have a better understanding in relation to the role of excess aluminium in ferritic microstructure it required an investigation of the austenite to ferrite transformation. Prior to investigation of the influence of aluminium on austenite to ferrite transformation, attempts were made to reveal the role of excess aluminium in austenite formation. The results obtained from the latter part of the research enabled the author to better understand the role of excess aluminium in austenite grain formation and growth.

From this study, it may be concluded that excess aluminium has a significant influence on as rolled ferritic structure which could be the result of changes in austenite to ferrite transformation kinetics. In addition, the results obtained from this research show a significant effect of excess aluminium on austenite formation and growth.

Figures

Tables

List of Abbreviations and Symbols

TRIP	Transformation-Induced Plasticity
TTT	Time–Temperature–Transformation
GBA	Grain boundary allotriomorphs
WP	Widmanestatten ferrite plates
IT	Intragranular idiomorphs
IP	Intragranular plates
Γ	Austenite
A	Ferrite
c_α	Fractional concentration of an alloying element in α
c_γ	Fractional concentration of an alloying element in γ
ΔH	Enthalpy change
PLE	Partitioning Local Equilibrium
NPLE	Negligible Partitioning Local Equilibrium
PE	Para equilibrium
K	Solubility product
Q	Activation energy
R	Gas constant
T	Temperature
UHCS	Ultra High Carbon Steel
IF	Interstitial Free
UTS	Ultra Tensile Strength
TWIP	Twining Induced Plasticity
A_{e3}-A_{e1}	Equilibrium transformation temperature
HR	Hot Rolled
CR	Control Rolled
FRT	Finish Rolling Temperature
A_{r1},-A_{r3}	transformation temperatures on cooling
A_{c1},-A_{c3}	transformation temperatures on heating
CHT	Continuous Heating Transformation
EBSD	Electron Backscattered Diffraction
FEGSEM	Field Emission Gun Scanning Electron Microscope
BSE	Backscattered Electron
SE	Secondary Electron
Λ	Wavelength of the electron beam
D	The spacing between the crystalline planes
Θ	Diffraction angle
TEM	Transmission Electron Microscopy
SEM	Scanning Electron Microscopy
FIB	Focussed Ion Beam
GB	Grain Boundary
FGAD	Ferrite Grain Area Distribution
GMOD	Grain Misorientation Distribution
Ac_Θ	Dissolution of pearlite
$C^{\alpha}_{\max}$	Maximum solubility of carbon in ferrite
$C^{\gamma}_{\max}$	Maximum solubility of carbon in austenite
f_p	Volume fraction of pearlite colonies
$\Delta l/l_0$	Relative change in length
FGB	Ferrite Grain Boundary

EMPA	Electron Probe Microanalysis
PAGS	Prior Austenite Grain Size
G	Growth rate
I	Nucleation rate
ΔT	Undercooling

Contents

Introduction

Aluminium traditionally has been used for nearly 100 years as a deoxidising element in the steel industry. It is common practice to add more than sufficient aluminium to steel at the end of the steel making process, to combine with oxygen to ensure that the desired cleanness level of the steel is achieved. Any excess Al will combine with nitrogen to form aluminium nitride, which then often plays a significant role in grain size control during the subsequent processing.

Although the effect of substitutional elements such as manganese and chromium has been investigated in detail over the last few decades, there has been little research concerned with the effect of Al as a substitutional element in steel in amounts higher than 0.1 wt%. This could be due to the previous lack of industrial interest and also technological concerns over the production of high Al-content steels.

Recently, however, there has been great commercial interest in Al additions, of the order of 1-2 wt%, to high strength, low carbon strip steels to produce a highly desirable dual phase microstructure containing retained austenite for cold forming applications. These steels rely on conventional strip mill processing to produce a microstructure of ferrite, austenite and martensite which can then be used to develop a combination of high strength and ductility by transformation-induced plasticity (TRIP), i.e. transformation of austenite to martensite during plastic deformation, for optimum forming response. However, inappropriate processing of such steels is known to produce a ferrite/martensite microstructure with very poor formability behaviour and toughness. Substitution of silicon, which reduces the galvanizability of steel by formation of silicon oxide on the surface, by aluminium to improve the galvanizability of steel, has drawn much attention to aluminium additions to TRIP steels. However, it should be noted that most of the research concerned with the role of aluminium in steel has been confined to factors influencing the mechanical properties with comparatively little work on the role of Al on steel microstructure.

The broad aim of this investigation is to study the role of aluminium as a deliberate solid solution addition in controlling the microstructure of low carbon steel. To

achieve the aim of the project, systematic research concerned with the role of aluminium in effecting ferrite grain size and ferrite grain distribution was performed by studying the as rolled microstructure in steels with Al additions between 0.02 and 0.94 wt%. It was shown that aluminium, present particularly as aluminium nitride, has a considerable influence on grain structure. Therefore, additional experiments were designed to establish the mechanisms by which aluminium may affect the development of the grain structure. Subsequently, the influence of aluminium on austenite formation and austenite grain growth and hence the influence of aluminium in austenite on the ferrite transformation was investigated.

Chapter 1: Literature review

Introduction

Aluminium has been widely used as a de-oxidant element in steels for more than 100 years. De-oxidation of steel with aluminium is very commonplace today and plays a crucial role in ladle metallurgy. Aluminium forms aluminium oxide and decreases the amount of oxygen in the steel and facilitates the production of killed steels. The addition of aluminium not only results in formation of alumina inclusions but also affects the inclusion chemistry [1]. As with other metallic elements such as vanadium, titanium and niobium, aluminium, in the presence of nitrogen, can form aluminium nitride. AlN can exhibit either an hexagonal structure with a=0.311 nm and c=0.4978 nm (the stable form of aluminium nitride at room temperature) or a meta stable cubic, NaCl type structure with the cell length ranging from 0.4045 to 0.417 nm [2]. It is worth noting that nitrogen can also form an iron nitride below 350ºC which dissolves at 500 ºC [3].

Although AlN does not contribute greatly to precipitation hardening, it is well known that it has a strong effect on grain refinement by inhibiting grain growth in steels, leading to improved mechanical properties [4, 5]. Aluminium nitride differs from other microalloy precipitates such as VN, TiN and NbN in structure and as such it cannot co-precipitate with other elements and it has little or no solubility for other microalloying elements [6].

Although the main focus of present study is based on the effect of Al in solid solution, the effect of Al as AlN in steel microstructure could not be ruled out even at the very low level of nitrogen which is the case in this study. Therefore, the effect of Al as AlN will be discussed later on in this chapter and also in chapter 5.

Prior to focussing on the role of aluminium in steel it is worthwhile briefly discussing the role of other alloying elements in steel on the steel microstructure.

1.1 Iron – Carbon Phase Diagram

Regarding the role of alloying elements on steel properties and microstructure, carbon can be considered as the most important element in steel. Dependent on temperature, pure iron exists as two crystal structures, bcc (body centred cubic) and fcc (face centred cubic) at atmospheric pressure. The body centred cubic structure (α-iron, ferrite) remains the stable structure up to 910ºC (A_3 point) and above this temperature it transforms to a face centred cubic structure (γ-iron austenite) which is stable up to 1390 ºC, (A_4 point) when it reverts to another bcc form, which is called δ-iron and is stable up to the melting point (1536ºC). It should be noted that it is also possible to obtain a hexagonal close packed form of iron (ε-iron) above 130 kbar pressure.

The addition of carbon to iron forms steel. It is significant that adding even a small concentration of carbon, for instance 0.1–0.2 wt%, has a great strengthening effect on iron [7].

To understand the behaviour of the iron – carbon system, we should study the iron-carbon equilibrium phase diagram. It should be noted that the commonly shown iron – carbon phase diagram represents the metastable equilibrium between iron and iron carbide (cementite). The largest solid solubility of carbon in ferrite is 0.02 wt% at 723ºC and consequently excess carbon forms a second phase which is called cementite. Figure 1.1 shows the equilibrium iron-carbon (cementite) diagram. As it illustrates, there are 4 stable phases present between the melting point and room temperature. The iron – carbon equilibrium phase diagram consists of two essential transformations. The most important one is the eutectoid transformation which occurs at 723^{o}C. The eutectoid transformation transforms γ-iron containing, 0.77 wt% carbon, to ferrite and cementite. The product of eutectoid transformation in carbon compositions below eutectoid composition is pro eutectoid ferrite while in carbon compositions above eutectoid composition is pro eutectoid cementite.

It should be noted that the eutectoid transformation takes place at equilibrium or near to equilibrium conditions and if rapid quenching is performed phase transformation results in a metastable structure called martensite.

It should be noted that the effect of time is ignored in the equilibrium diagram. By considering time in the transformation, TTT diagrams (Time–Temperature–Transformation) may be produced which represent fully the transformation behaviour of the steel (Fig. 1.2). In the simple case of a eutectoid plain carbon steel, the curve is roughly 'C' shaped (Fig 1.2a) while it becomes more complex for hypo or hyper eutectoid concentrations [7, 8] (Fig. 1.2b)

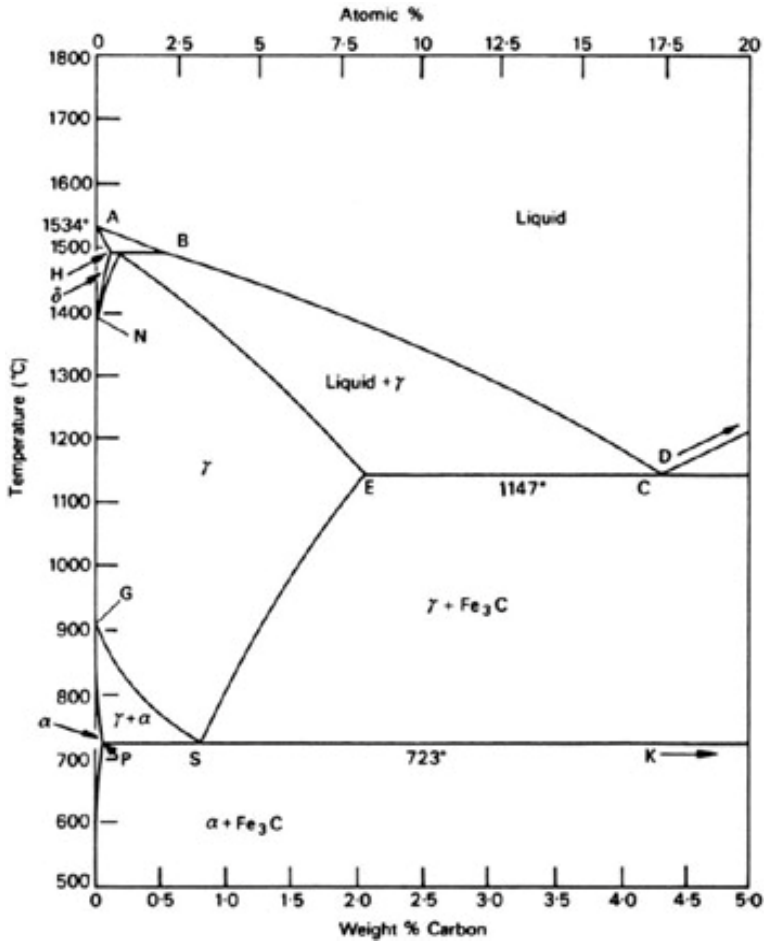

Figure 1.1 Iron-Carbon equilibrium phase transformation diagram [7]

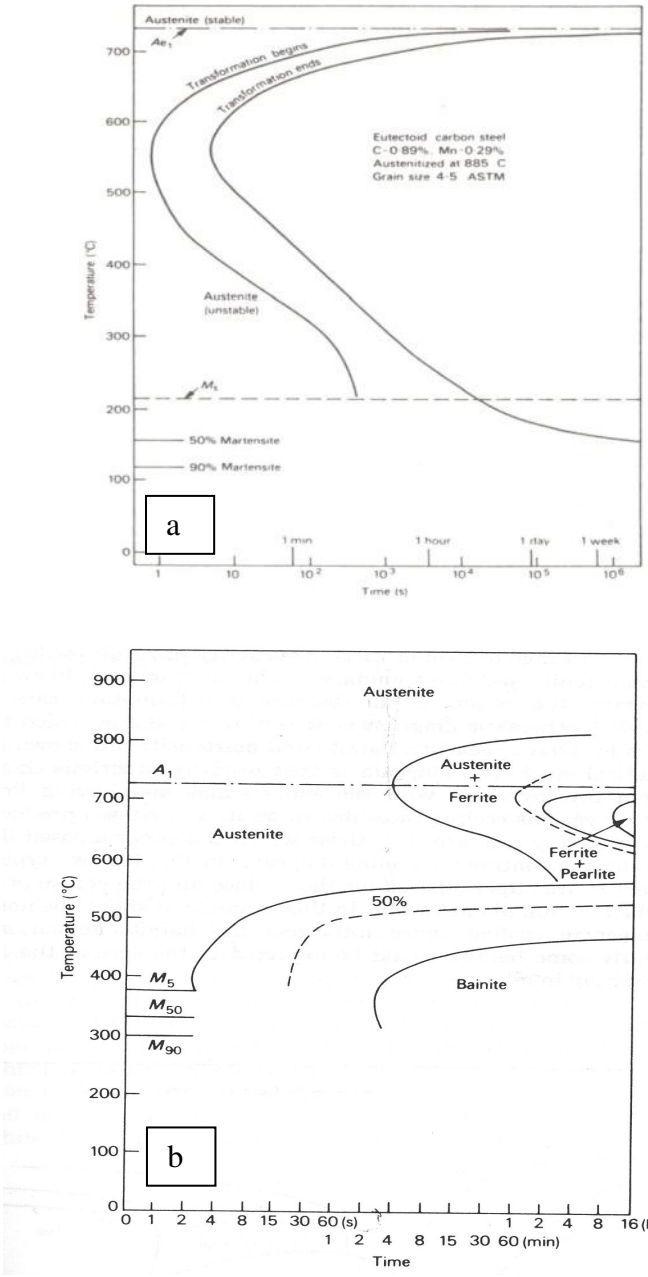

Figure 1.2 a) TTT diagram for a 0.89 wt%carbon steel b) TTT diagram for 0.3 wt% carbon, 2.0 wt% Mo steel [1]

1.2 The proeutectoid transformation of austenite

As already mentioned, the microstructures obtained when steel is slowly cooled from the austenite phase depend on the carbon concentration of the steel. The microstructure will contain two primary constituents: proeutectoid ferrite and pearlite if the carbon concentration is less than 0.77 wt%. Both proeutectoid ferrite and cementite preferentially nucleate on the austenite grain boundaries because they are regions where the diffusion rates are higher and contain energetically favourable sites for nucleation. The proeutectoid ferrite morphology can be divided into four groups [7]:

- **Grain boundary allotriomorphs (GBA)**: an allotriomorph has a shape which does not reflect its internal crystalline symmetry. The grain boundary allotriomorph ferrite is in contact with at least two of the austenite grains (Fig. 1.3a).

- **Widmanstatten ferrite plates or laths (WP)**: these plates grow along well-defined planes of the austenite and do not grow across grain boundaries. Primary Widmanstatten ferrite grows directly from the austenite grain surface, whereas secondary Widmanstatten ferrite develops from allotriomorph ferrite already present in the microstructure (Fig. 1.3b).

- **Intragranular idiomorphs (IT)**: these are equi-axed crystals which nucleate inside the austenite grains. This group of ferrite morphology form without contact with the austenite grain surface usually on non-metallic inclusions in the steel (Fig. 1.3c).

-**Intragranular plates (IP)**: this form of ferrite is similar to those growing from the grain boundaries, but they nucleate entirely within the austenite grains (Fig. 1.3d).

It should be noted that the appearance of each form of ferrite depends on the steel composition and cooling conditions.

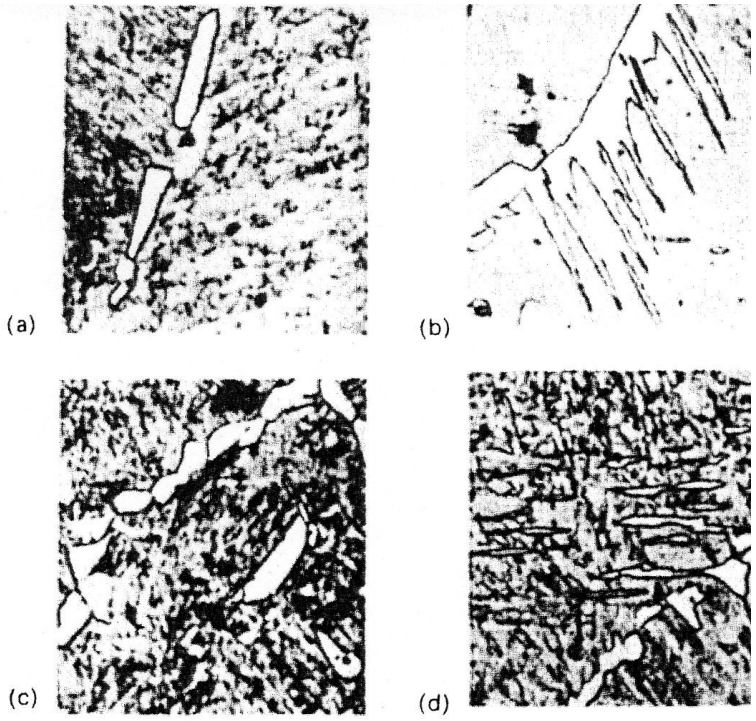

Figure 1.3 Different proeutectoid ferrite morphology [7]

1.2.1 The effect of alloying elements on the Fe-C equilibrium diagram

It should be noted that additional alloying alters the Iron-Carbon diagram. Basically, an alloying element can influence the Fe-C diagram in two ways [7]:

1- By encouraging the formation of ferrite, α-iron, over wider compositional limits, and contracting the austenite, γ-iron, region. These α-stabilizer elements can be divided into two categories, closed γ-field and contracted γ-field (Fig. 1.4).

a) Closed γ-field: this category consists of many elements which restrict the formation of γ-Fe, causing the γ area of the diagram to contract to a small area referred to as the gamma loop. In other words, these elements encourage the formation of α-Fe, and one result is that α and γ phase fields become continuous. Silicon, aluminium, beryllium, and phosphorus belong to this category, together with strong carbide formation elements such as titanium, vanadium and molybdenum. For instance, Fig. 1.5 shows the Al-Fe equilibrium diagram. The presence of Al causes the γ field within the phase diagram to be limited.

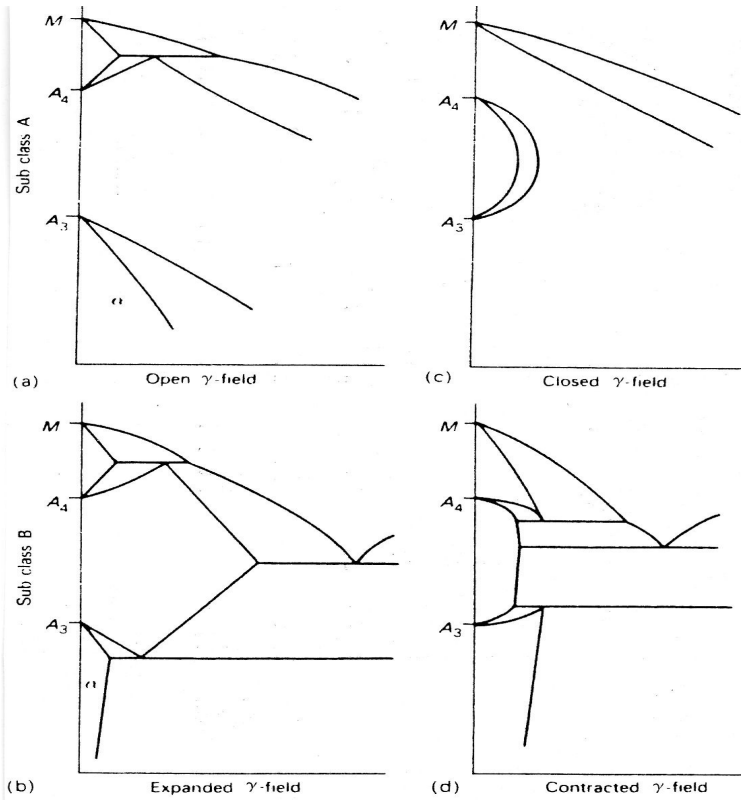

Figure 1.4 classification of iron alloy phase diagram [7]

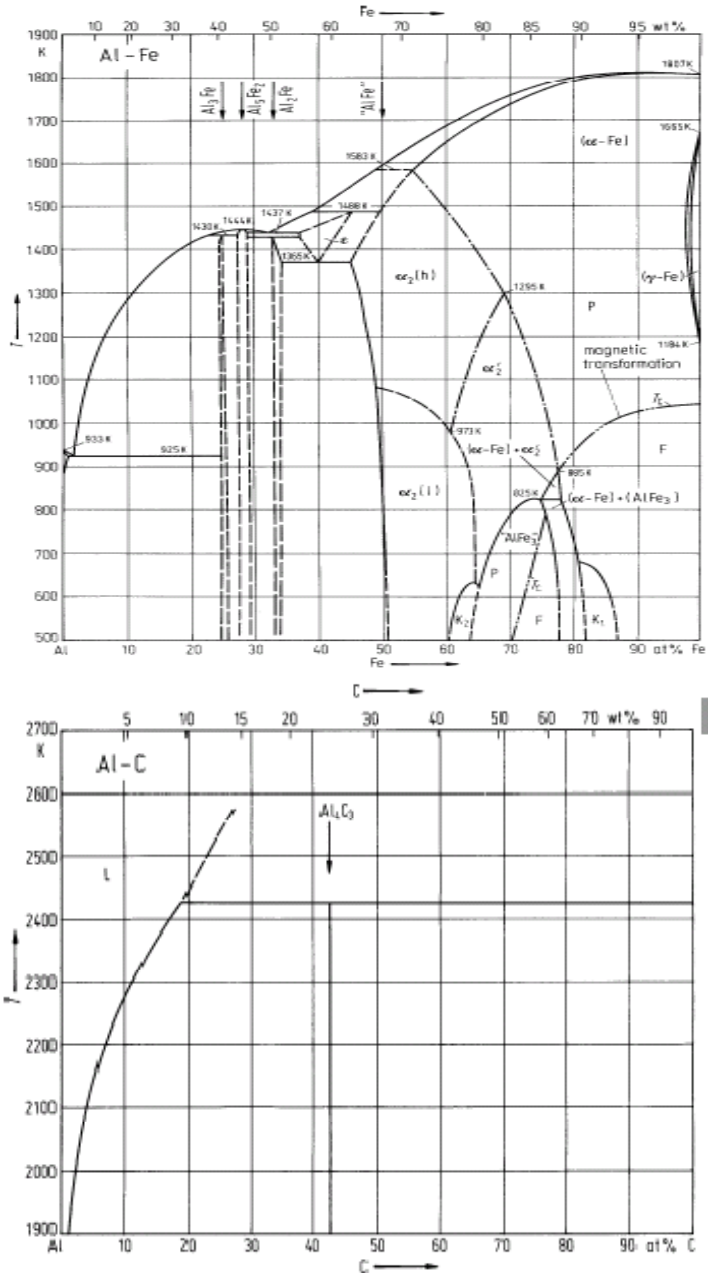

Figure 1.5 the equilibrium phase diagram Al-C and Al-Fe [9]

b) Contracted γ- field: the γ loop is strongly contracted, but is accompanied by compound formation. Boron, together with carbide forming elements such as niobium and zirconium, falls into this category.

2- By encouraging the forming of austenite over wider compositional limits and expanding the γ- field. These elements can be divided into two categories:

a) Open γ- field: These elements can eliminate the α-Fe phase and substitute with the γ-Fe phase. Nickel and manganese, as well as cobalt, belong to this category. In other words, these elements would be able to depress the phase transformation from γ to α to lower temperature.

b) Expanded γ-field: Carbon and nitrogen are the most important elements in this group. The γ-phase field is expanded, but its range of existence is cut short by compound formation.

The overall behaviour is the best described in thermodynamic terms along the lines developed by Zener and by Andrews. If c_α and c_γ are the fractional concentration of an alloying element in α and γ- phases, the following relation holds:

$$\frac{c_\alpha}{c_\gamma} = \beta\, e^{\Delta H / RT} \qquad \text{(Equation 1.1)}$$

Where ΔH is the enthalpy change which is the heat absorbed per unit of solute dissolving in γ-phase minus the heat absorbed per unit of solute dissolving in α-phase. The ferrite formers have positive ΔH which means $H_\alpha < H_\gamma$ and austenite stabilizers have negative ΔH which means $H_\alpha > H_\gamma$. β is constant (Fig. 1.6).

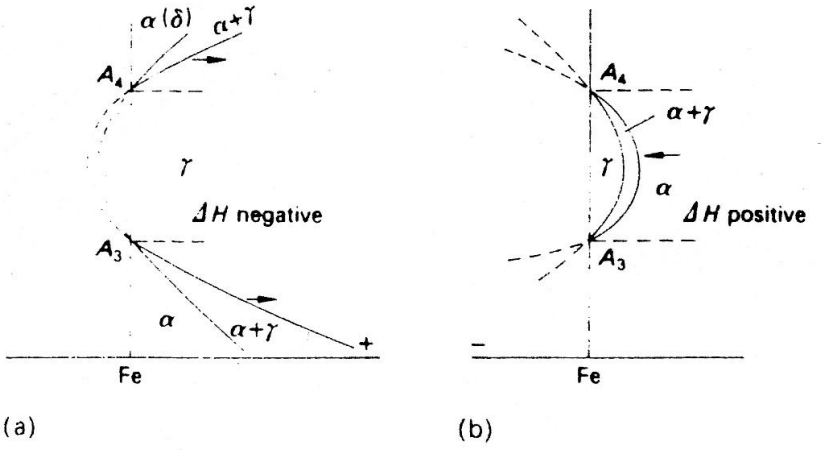

Figure 1.6 two basic phase diagrams: (a) ΔH negative, (b) ΔH positive [7]

1.2.2 The effect of different elements on the ferrite reaction

Austenite has higher solubility for carbon than ferrite. Therefore, during the austenite/ ferrite transformation carbon is partitioned into the austenite. As

transformation proceeds, so does the extension of the carbon diffusion field in the austenite. This process decelerates ferrite growth since the solute then has to diffuse over ever larger distances. In other words, the growth rate slows down as time increases. Therefore, the ferrite growth rate is controlled by carbon diffusion in plain carbon steels; however, addition of substitutional elements such as Mn or Mo may alter this process due to the significant difference in diffusivity of carbon and those substitutional elements [7].

The effect of alloying elements on austenite to ferrite transformation has been the subject of academic and industrial researches for more than a century. Generally speaking there are three modes of growth of pro-eutectoid ferrite in austenite that have been proposed in Fe-C-X alloys. The growth can follow any of these modes subject to composition and also temperature [10]. The modes are:

1) Full equilibrium at α/γ boundaries with partition of X and C between γ and α; partitioning local equilibrium (PLE). This condition may occur over a temperature range close to the A_{e3} i.e. at low supersaturation of the additional alloying element. At this condition the austenite/ ferrite boundary may migrate with significant partitioning of the additional alloying element "X" between ferrite and austenite to equilibrate the chemical potential of both interstitial and substitutional elements. In this case the growth is controlled by diffusion of "X" in austenite.

2) Local equilibrium without bulk partition of X between the two phases but with a "pile up" of X at the advancing γ/α boundary; negligible partitioning local equilibrium (NPLE). At this condition the boundary may migrate with an equilibrium interface composition, so called "solute drag", however there is no bulk partitioning of element "X" between the two phases.

3) Para equilibrium at the α/γ boundaries with only partition of carbon. In this condition there is no partitioning of alloy "X" at all. It occurs at temperatures where the diffusion of substitutional solutes is not possible.

In this mode the growth is controlled by carbon diffusion in austenite since the chemical composition of carbon equilibrate across the boundary.

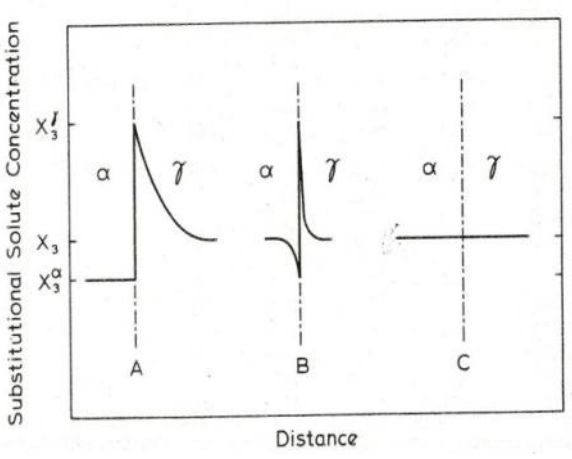

Figure 1.7 A schematic representation of alloying element X distribution during ferrite growth for each mode [10, 11].

As stated above, the austenite to ferrite transformation is the function of diffusion, specifically in formation of allotriomorphic ferrite; however, the kinetics depends on whether substitutional atoms are partitioned between the austenite and growing ferrite. The interaction between the solute atoms and carbon, as well as binding between solute atoms and the ferrite/austenite interface, also needs to be taken into account. For instance, when X tends to form a carbide, further complexity such as the retardation of the interface by precipitates needs to be taken into account to understand the effect of additional alloying elements on ferrite growth. Ranking of solute elements not only in terms of interaction between X and C but also between the austenite / ferrite interface and X has recently been studied by Aaronson [12]. In relation to C-X interaction, Co, Ni, Al and Mn can be classified as those elements which barely have any interaction with carbon. In contrast, V, Ti and Nb have a strong tendency to form carbides. According to the estimated binding energy between X and the interface, Aaronson [12] has suggested that Co, Ni and Al have a very weak, almost negligible interaction with the interface, however, Mo and Nb have a very strong interaction with austenite / ferrite interfaces. This means that, for example, in the case of Ni and Co as solute elements, the solute drag effect, if any, would be insignificant, however the effect of Mo would be expected to be larger because of the stronger interaction between the Mo atoms and interface [13]. The

combination of partitioning effect and also interaction of solute with C and the interface determines the effect of substitutional solute elements on ferrite growth in austenite to ferrite transformation [13].

Partitioning of alloying elements also has drawn much attention in the last past few decades. One of the most comprehensive studies was conducted by Aaronson and Domian [14] who examined the alloy element concentration in ferrite at a relatively early stage in a series of Fe-C-X alloys. In addition, recently some of their results have been re-examined by Enomoto [15]. Enomoto has concluded that partitioning and consequently different growth mechanisms may happen at different temperatures and the growth mechanisms may vary at different temperatures and in the presence of different elements. For instance, he showed that there is a clear evidence of partitioning of Si at 820 ºC in Fe- 1.8 at.% C-3.3 at.% Si steel and therefore it will be expected that the growth of ferrite at the same temperature should be affected by the partition of Si. However, there is no clear evidence available for the partitioning of Si at 920 ºC in the Fe- 0.5 at.% C-3.6 at.% Si which has slightly higher Si levels. Similar results were also shown for Al additions steels. There is no clear evidence available of Al partitioning in Fe- 1.2 at% C-2.8 at.% Al alloy while Al partitionsin a Fe-C-Al alloy with higher carbon content.

Another recent investigation carried out by Aaronson and co-workers [16] on a Mn-Si low carbon steel showed that ferrite growth can be divided into three main stages. The first stage is where rapid growth occurs. No partitioning of Mn should be expected at this stage. In the second there is no partitioning but enrichment of Mn and presumably Si at the interface. In the third and final stage there is significant partitioning of Mn and possibly Si. This work supports the idea of changes in growth mechanisms in the ferrite transformation from PE to NPLE and then to PLE proposed by both Aaronson [17] and Hutchinson[13].

1.3 Effect of Al on steel microstructure

1.3.1 Effect of Al as AlN particles on steel microstructure

As mentioned in the introduction of this chapter, like other microalloying elements, aluminium can form a nitride. The solubility of AlN can be defined by the normal solubility product equation:

$$\ln [Al][N] = \ln K = Q/RT + C \qquad \text{(Equation 1.2)}$$

Where the [Al] and [N] represent the concentrations of soluble Al and N, respectively, K is the solubility product, Q is activation energy, R is gas constant, T is absolute temperature and C is a constant. It is believed that the rate and kinetics at which AlN precipitation takes place in steel depends on various parameters such as chemical driving force, time and temperature. The chemical driving force, which is directly related to the concentration of Al and N in steel, is one of the most important parameters which can affect the presence and the volume fraction of AlN in steel. As mentioned, one of the main reasons for utilizing Al in steel is obtaining a finer grain structure. It is well documented [18, 19] that decreasing the grain size is the only way of increasing both strength and ductility simultaneously. When plain carbon steel is held at high austenetising temperatures, grain coarsening takes place resulting in a relatively uniform, equiaxed coarse austenite grain structure. The reduction of grain boundary area and consequently the grain boundary energy would be the driving force for grain growth. However, the presence of pinning particles such as AlN would change this gradual grain growth regime. In aluminium treated steels, grain growth is inhibited at lower temperatures (depending on the level of Al and N) but at a certain temperature, termed the sudden grain growth or grain coarsening temperature, sudden grain growth occurs. This abnormal grain growth results in a mixture of fine and very coarse grained structure [18].

In aluminium treated steels, as in other microalloyed steels, the grain coarsening or abnormal grain growth temperature can be related to the solution temperature of microalloy precipitates or to the temperature in which coarse particles begin to grow at the expense of smaller particles. It is well documented that the pinning effect of AlN is a function of volume fraction and also the size of the particles [20]. For

instance, it has been shown that increasing the Al content to 0.04 wt% would increase the grain coarsening temperature (for the same nitrogen content); however, additional Al content above 0.04 wt% would result in a reduction in the grain coarsening temperature. This can be attributed with the fact that due to the limited solubility, at high aluminium contents, precipitation of AlN occurs at high temperature. This results in having few coarse AlN particles which are less efficient in suppressing the grain growth [19]. More discussion about AlN and its influence on grain structure can be found in chapter 5.

1.3.2 The effect of excess aluminium on grain size

Although aluminium is primarily known as a grain refining element due to AlN formation, some work, mostly based around high Si steels, has shown that, depending on the level of additional Al, excess aluminium in steel may have an influence on the microstructure in steels of different compositions [21-23]. Nakamaya and Hojou [21] have shown that by adding 0.07 wt% Al, ferrite grains become finer, while the addition of more than 0.1 wt% Al leads to slightly coarser ferrite grains as compared with the lower Al content steels. A similar phenomenon has been reported in ultra low carbon steels. In this case, increasing the aluminium content has been shown to lead to a coarser and more equiaxed grain structure (Fig. 1.8) which was believed to be attributed to the effect of Al and N content on AlN [24, 25].

As mentioned, a change in Al content seems to be affecting not only grain size but also grain size distribution. In general, the grain size distribution becomes more uniform ('normal' distribution) in higher aluminium steels [21, 24]. It is well known that the level of aluminium and nitrogen determines the stability of the aluminium nitride particles which can then interfere with the grain growth process [18]. In other words, the observed variation in grain size in Al added steels could be associated with both the effect of Al content on the AlN particles and the potential influence of Al on the transformation behaviour of the steels [19, 20, 26].

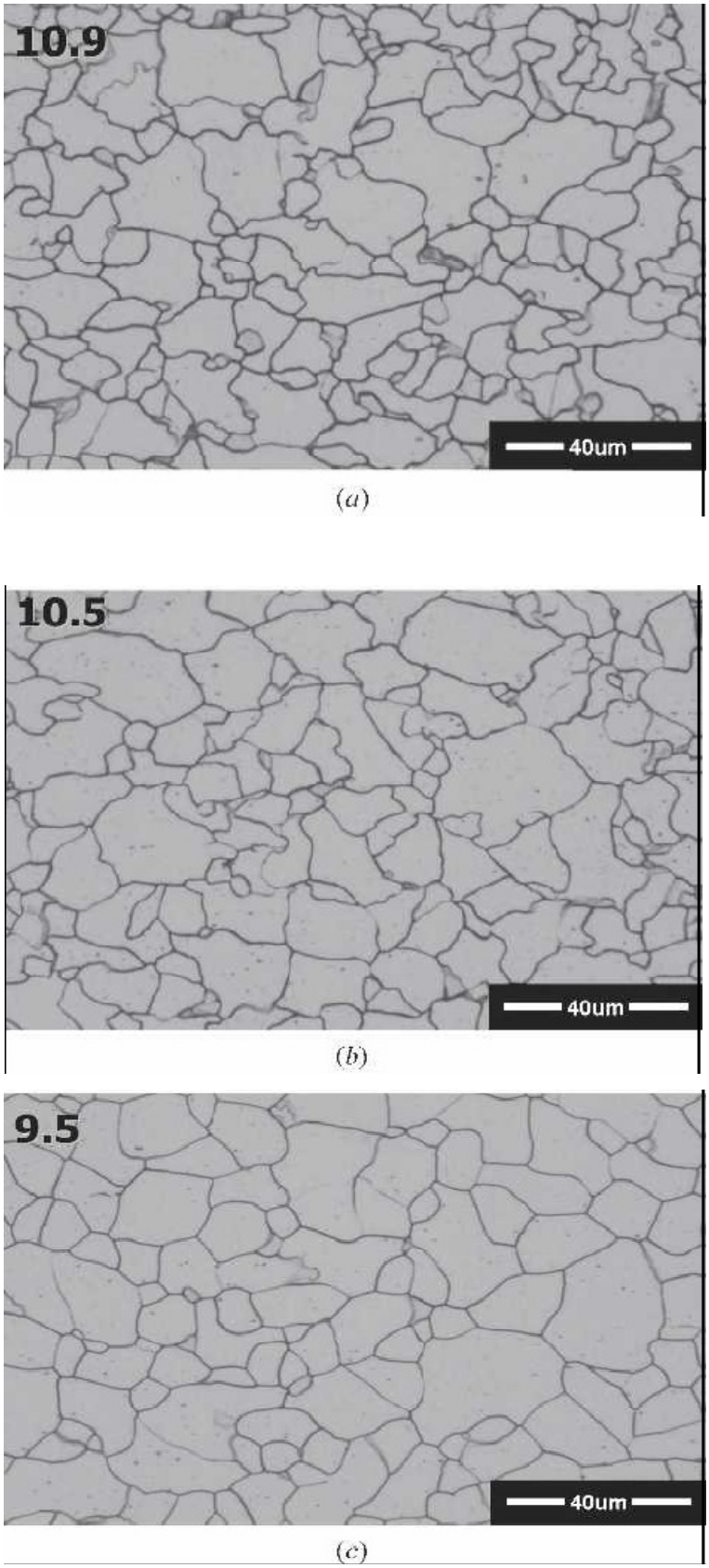

Figure 1.8 Optical micrographs showing the effect of Al content on the microstructure of hot-rolled steels: steel with 0.055 wt % Al, (b) steel with 0.093 wt % Al, and (c) steel with 0.16 wt % Al. The grain size index number in the ASTM scale is shown in the micrographs [21]

1.3.3 Effect of Al upon the austenite to ferrite transformation

The effect of substitutional elements on transformation temperature and transformation kinetics has been discussed very briefly in section 1.2.1. However, there is a lack of systematic studies of the effect of Al on transformation temperature and kinetics.

It is well known that aluminium, like silicon, delays the austenite to bainite transformation [27]. Based on an investigation carried out on high purity steels, it has been shown that large additions of aluminium (> 1 wt%) can raise the transformation temperature (A_3) [28]; no evidence was reported, however, to indicate a significant change in ferrite morphology.

In addition to the effect of aluminium on transformation temperature, it is also known to be a ferrite stabilizing element in amounts greater than 0.5 wt% and as the aluminium content increases the microstructure tends to a ferrite / martensite structure. Mintz has shown that addition of Al at levels of 0.02 to 0.2 wt% gives a ferrite / pearlite structure, while increasing the aluminium content to 1 wt% leads to martensitic structure formation rather than pearlite and at 2 wt% aluminium, pearlite is completely suppressed and the remaining austenite transforms to martensite [29].

Furthermore, Eldridge [27, 30] illustrated that aluminium can raise the transformation start and finish temperatures for additions in the range of 0.005-0.072 wt% Al. It was also shown that the transformation kinetics can be changed by the level of aluminium present in steel depending on cooling rate. One interpretation of these observations was that segregation of aluminium to the ferrite / austenite interface had occurred and this influenced the transformation behaviour [30].

1.4 Segregation of aluminium to grain boundaries

Whilst the segregation/ partitioning of aluminium to the advancing ferrite/austenite interface has been proposed as a mechanism for the effect of aluminium on the transformation behaviour in steels [30] it has also been suggested that aluminium, like boron, can affect the transformation behaviour (nucleation and growth) by reducing the austenite grain boundary energy. The formation of a monolayer of segregant at the interface boundaries is believed to affect the grain boundary mobility [30, 31].

Mabuchi and co-workers examined the segregation of Al to prior austenite grain boundaries in 5% Ni steels [32-34]. They have shown that the presence of additional alloying elements can affect the segregation of aluminium to austenite grain boundaries. For instance, the removal of Mn from the steel with 0.3 wt% Al and 0.02 wt% Mn significantly increases the grain boundary segregation of Al. This significant increase of Al segregation was attributed to the site competition between Al and Mn in prior austenite grain boundaries. Furthermore, they reported that segregation of Si is significantly increased by raising the Al concentration. Mabuchi investigated the concentration of Al and Si along the grain boundaries. He has shown that there is a repulsive interaction between Al and Si which causes considerable periodic segregation of Al and Si along grain boundaries. He showed a clear periodic segregation of Al and Si which varied alternately by the cycle of about 3nm.

In addition to the segregation of Al to grain boundaries in 5% Ni steels, Mabuchi and co-workers examined the segregation of Al in a plain carbon steel with 0.35 wt% Al, 0.1 wt% P, and 0.53 wt% Si. They showed that the periodic alternating segregation of Al does not depend on the presence of the other alloying elements such as Ni and Mn. This means that this phenomenon can be expected not only in 5% Ni steels but also in any kind of steel.

As discussed above, there is strong evidence for Al segregation to austenite grain boundaries and it is possible to conclude that, at least for ferrite/ pearlite steels, there may be reasons to suppose that Al may have a marked effect on transformation

behaviour. To the knowledge of author there is a lack of study regarding the relation between segregation of Al to grain boundaries and changes in ferrite grain size and grain size distribution (as a result of changes in austenite to ferrite transformation behaviour). This needs to be addressed in future research to have a better understanding of the role of Al in influencing steel microstructure.

1.5 Other aspects of excess aluminium on microstructure

In addition to the effect of aluminium on transformation behaviour and grain size, aluminium is known not to form carbides in steel. Hence, aluminium interferes with the formation of the pro-eutectoid carbide network at the grain boundaries and also inhibits the precipitation and growth of the carbide plates in UHCSs (ultra high carbon steel). In other words, excess aluminium can increase the ductility of UHCS by changing the carbide morphology and inhibiting the formation of the carbide network [35]. Furthermore, it is interesting to note that aluminium can affect the formation of microalloy carbides due to its non-carbide-forming property. For example, the number of fine NbC precipitates was found to significantly decrease with an increase in the aluminium content affecting both the toughness and strength in an ultra low carbon steel [24].

It should be noted that aluminium additions in the range of 1 to 4 wt% also can affect the segregation behaviour of Cu and Sn in steels to ferrite grain boundaries [36].

1.6 The effect of excess aluminium on mechanical properties

Although it is believed that Al cannot be considered as a precipitation strengthening element, it can affect mechanical properties as a solid solution strengthener or grain refining element by changing the microstructure [24, 29]. It has been shown that Al has a dramatic effect on hardenability, particularly of Cr-Mo steels even when present in amounts as low as 0.01 wt%. In the case of hot rolled, ultra low carbon Nb-IF (interstitial free) steels, it was reported that Al additions have a softening effect and also decrease the strength. It should be noted that the softening effect of aluminium was expected as a result of decreasing the number of fine NbC precipitates due to decreasing the carbon activity by Al and promoting coarser, more uniform and equiaxed grain structures as a result of coarsening AlN precipitates. In contrast, Mabuchi has shown that adding a small amount of excess aluminium has a deleterious effect on low temperature toughness in an A302C steel (Mn-Mo-Ni) due to changing the microstructure from fine ferrite to coarse upper bainite [37]. A change in the microstructure is associated with the effect of Al on transformation

behaviour. Furthermore, it was shown by Mabuchi that the excess Al has different effects on the tensile strength depending on the chemical composition of steels. He showed that additional Al can increase the tensile strength in Mn-Mo steel whereas it does not have any significant influence on Mn-Mo-Cr-Ni steels [37, 38].

Recently, Mintz has shown that Al additions can improve the impact behaviour of steel. He indicates that aluminium additions of up to 0.2 wt% can increase the impact behaviour by removing nitrogen from the steel due to the formation of AlN and also by refining the grain boundary carbides without considerable influence on strength [39].

In addition to the effect of Al on impact behaviour, the influence of Al on strength as a solid solution strengthener has been investigated by Mintz. Although the atomic radius of aluminium is similar to silicon, which is accepted as having a large solid solution strengthening effect in iron, until recently aluminium has not generally been considered to be a solid solution strengthening element [29]. Despite the fact that Al acts as a substitutional solid solution on pure Fe, Frommeyer indicates that Al levels up to 2 wt% behave in a similar manner to Ni in steel i.e. it slightly decreases the strength of steel (Fig. 1.9) [40].

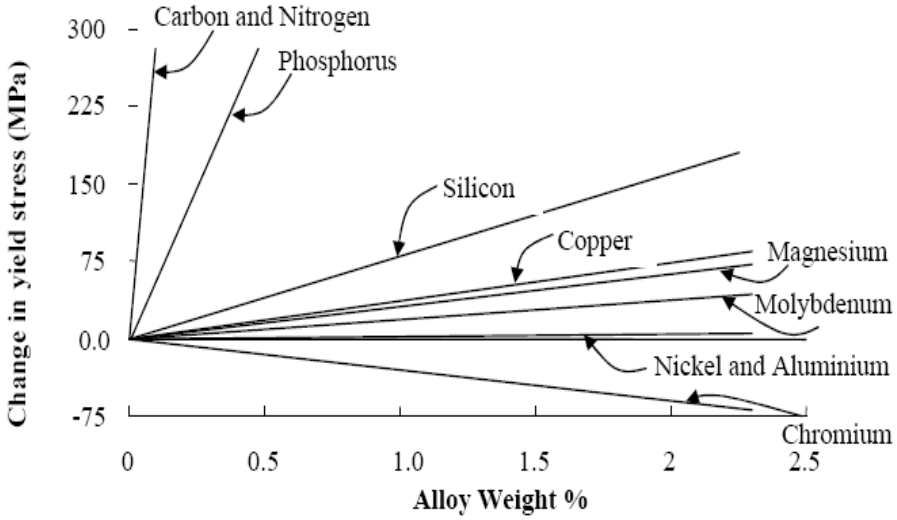

Figure 1.9 Influence of alloying elements on the yield stress of steel [40].

In contrast, Mintz has recently shown the significant effect of aluminium as a solid solution strengthener in steel. He indicates that a 1 wt% addition of aluminium to low carbon and low nitrogen steels gives an approximate 70 MPa increase in strength which is similar to the effect of silicon in steel as would be expected from the similar atomic sizes of both elements. However, Mintz notes that the changes in mechanical properties are not only dependent upon the levels of aluminium but also on the concentrations of carbon and nitrogen. For example, in the case of a 0.1 wt% carbon and 0.005 wt% nitrogen steel, it can be seen that the UTS (ultra tensile strength) increases with Al content while the yield strength shows a small decrease. Mintz mentioned that there was a masking of the strengthening effect of Al (for levels lower than 0.2 wt% Al) possibly due to the formation of AlN. AlN formation would remove the N from the solution and obviously reduce the interstitial solid solution strengthening effect of nitrogen which is about 5 MPa per 10 ppm. He pointed out that if adding 0.2 wt% Al can improve the tensile strength by 15 MPa, removing 40 ppm nitrogen decreases the tensile strength by 20 MPa and finally adding 0.2 wt% Al leads to 5 MPa reduction in strength [29].

Furthermore, the presence of martensite might be another reason for the decrease in tensile strength on adding Al at levels greater than 0.2 wt% in steels which have about 0.1 wt% carbon present. As mentioned before, Al can delay the austenite to ferrite transformation and promote retained austenite or a martensite microstructure, specifically in the pearlitic region. To negate the interference of aluminium on the formation of martensite and removal of free nitrogen, Mintz carried out his investigations on very low carbon and nitrogen steels (0.02 wt% C and 0.001 wt% N) and showed that the solid solution strengthening effect of Al is about 70 MPa per 1wt % independent of grain size [29].

It is believed that aluminium affects the mechanical properties via several possible strengthening mechanisms. However, it is important not to consider the aluminium in isolation but to always be aware of the full composition of the steel**.**

1.7 Aluminium in TRIP steels

Transformation induced plasticity (TRIP) steels were developed in the late 1960's. Generally, TRIP steels have some additional alloying elements to delay the austenite to bainite transformation and they retain a significant amount of austenite at room temperature [41-43]. It should be noted that the retained austenite can transform into martensite during the deformation and it is very useful for improving the formability of steels and gives excellent mechanical properties combining high strength with significant ductility [44, 45].

Usually TRIP steels have more than 1 wt% silicon to promote retained austenite in the microstructure. However, silicon can form a silicon oxide film on the surface and reduce the galvanizability and weldability of steels, specifically for spot welding. Some attempts have been made to solve these problems by reducing the silicon content or replacing the silicon by other elements such as aluminium and phosphorus [45-47]. The substitution of silicon by aluminium showed that it has potential for use in TRIP steels, however it is less effective than silicon, for the same concentration, in terms of suppressing carbide formation.

Furthermore, results showed that a full substitution of silicon by an equivalent amount of aluminium leads to considerable reduction of strength [43]. It should be noted that the effect of aluminium on the formation of strain induced martensite has been investigated and it was shown that as the aluminium content increased the formation of strain-induced martensite and also deformation twining became more difficult [47].

In addition to using Al in TRIP steels, it has been added in amounts between 1 to 8 wt% to TWIP (twining induced plasticity) and Hadfield manganese steels to modify their mechanical properties. The results showed that aluminium decreases the frequency of mechanical twins in austenite of Hadfield composition as a result of increasing the stacking fault energy of the austenite as also shown in TRIP steels [48-51].

1.8 Summary of the effect of Al on microstructural development

The role of aluminium in formation of ferrite can be summarised as follows:

- Apart from the early work by Aaronson and co-workers there is little systematic work on the effect of Al on either equilibrium transformation temperature A_{e3} or on the isothermal transformation kinetics. Both of these would be expected to influence continuous cooling transformation behaviour which in turn can be used to control the processing needed to produce an optimum microstructure for formable dual phase strip steels.

- To optimise the effect of Al on microstructure, it is also necessary to understand how Al segregates / partitions to grain boundaries and transformation interfaces in more detail. It would appear from the work by Mabuchi that the role of Al is influenced by the presence of other elements such as Si and Mn. With the advance of high resolution transmission microscopy it is the now possible to research both segregation and partitioning directly at the nano-scale of austenite grain boundaries and ferrite / austenite transformation interfaces.

- It is well known that addition of Al grain refines steels. This is largely the result of a finer ferrite grain size forming from a finer austenite grain size. Some studies have indicated that there may be an effect of Al directly on ferrite grain size possibly associated with segregation or partitioning effects, noted above. Changes in ferrite nucleation rate or growth rate would also be reflected in ferrite grain size distribution at the end of transformation. Up to the present there have been few studies concerning changes in ferrite grain size distribution due to the alloying. This was to do with the difficulty of data collection on a realistic time scale. Techniques such as automatic image analysis and EBSD allow such data to be obtained much more easily and

therefore it is possible to study the effect of Al as well as other solute elements on ferrite grain size distribution.

Chapter 2: Experimental methods

This chapter describes the principles of the different techniques employed in the present study and also details of the sample preparation methods.

2.1 Steel

To investigate the influence of aluminium in steel, 50 kg casts of steels of differing aluminium composition between 0.02 and 0.96 wt% were prepared in a laboratory vacuum melting furnace. The level of nitrogen was kept as low as possible to avoid the formation of aluminium nitride precipitates. The chemical compositions of the alloys are shown in Table 2.1. To observe the effect of the rolling condition, two different rolling schedules (hot rolled (HR) and control rolled (CR)) were performed and steels rolled to 13mm thick plate.

Table 2.1 Composition of Hot rolled steels (wt %)

Steel sample	C	Si	Mn	P	S	Al	N	Excess Aluminium	Rolling treatment
E	0.028	0.28	1.41	0.001	0.001	0.02	0.0022	0.018	HR
F	0.019	0.28	1.41	0.001	0.001	0.48	0.0015	0.478	HR
G	0.022	0.29	1.41	0.001	0.001	0.94	0.0019	0.938	HR
L	0.028	0.28	1.4	0.001	0.001	0.02	0.0022	0.018	CR
M	0.019	0.28	1.41	0.001	0.001	0.48	0.0015	0.478	CR

Table 2.1 also shows the excess Al which is defined by following equation:

$$Al(free) = \text{total Al} - 27/14\ N \qquad \text{(Equation 2.1)}$$

Excess Al implies the amount of aluminium remaining in solid solution in the bulk. In addition to chemical composition, the effect of rolling in high Al treated steels was examined by two different rolling schedules; hot rolling (HR) and controlled rolling. The details of the schedules are shown in Table 2. These schedules were based on previous experience of laboratory rolling of C-Mn-Nb steels and, as such, were not expected to be optimal for these low C steels. The first rolling schedule (HR)

consisted of rolling the plate from 1250 ^{o}C continuously to finish rolling (FRT) at ~1050 ^{o}C. This contrasts with the second schedule (CR) with the same reductions per pass but with a hold at 42mm from ~1150 ^{o}C to ~1050 ^{o}C aiming to finish rolling at a somewhat lower FRT, 950 ^{o}C.

Table 2.2 Hot rolling schedule (HR) as above, CR slab held at 7* aiming to reach to 1050 ^{o}C and then rolled as the same as HR

Pass number	Plate thickness (mm)		Reduction %	Aim temperature for HR(^{o}C)
	Start	Finish		
1	100	95	13.6	1250
2	95	80	15.7	
3	80	70	12.5	
4	70	60	14.3	
5	60	50	16.7	
6	50	42	16	1200
7*	42*	35	16.7	
8	35	28	20	1160
9	28	23	17.8	
10	23	19	17.4	
11	19	13	21.1	1095

2.2 Metallography

In order to reveal the as rolled and heat treated microstructure the specimens were polished to 1 μm and then etched using a mixture of 2% nital (2% nitric acid and 98% propan-2-ol (by volume) and picric acid (200 ml nital and 10 g picric acid).

Initial microstructural characterisation was performed using a Nikon Optiphot optical microscope. The images were captured using an AxioCam MRc 5 camera. The images were processed using the Axio Vision image processing software (Carl Zeiss).

Although attempts were made to reveal the austenite grain boundaries by hot picric acid etching the results achieved were not satisfactory. Therefore, thermal etching as

an alternative technique was employed to reveal the prior austenite grain boundaries. Section 2.4 will discuss in detail the principles of this technique.

2.3 Dilatometry

Dilatometry is one of the most powerful techniques to investigate the solid-solid phase transformation in steel [52]. It is frequently used for determining the phase transformation temperatures in steel, both on cooling (A_{r1}, A_{r3}) and heating (A_{c1}, A_{c3}). It is based on measuring the change of the specific volume of the sample during a phase transformation. Volume changes accompanying certain phase transformations, as the result of changes in structure and consequently in lattice parameter, allows us to determine the transformation temperatures.

The basic design of the dilatometer has remained unchanged for a number of years, however recently significant improvements have been made in terms of sensitivity, enhancing the data collection system and also the ability to deform the sample during the test. The sample is supported in a fixture of low thermal expansion coefficient such as silica or alumina. A rod of the same material transfers the change in sample length upon heating to a measuring device. A thermocouple attached to the specimen monitors the temperature during the cycle. An induction coil around the sample is the source of heat and the cooling takes place via quench gas injected at the specimen. Heating and cooling are usually carried out under vacuum to limit the possibility of oxidation particularly at high temperatures.

As mentioned, dilatometry can be used in the construction of transformation diagrams such as continuous heating transformation (CHT), time temperature transformation (TTT) and continuous cooling transformation [52]. Also, dilatometry can be employed to perform heat treatments which need precise control of time and temperature. In the present research two types of dilatometer (high resolution dilatometer Adamel Lhomargy DT1000 and Bahr D805) have been employed to determine the critical transformation temperatures and to examine the effect of additional Al on isothermal transformation of steel and austenite formation. Also, the dilatometry system has been used to perform the thermal etching technique (section 2.4).

2.3.1 Isothermal dilatometry

Isothermal dilatometry is the most common method by which isothermal transformation may be studied. An ordinary thermal cycle for an isothermal study involves austenetising the specimen at a specific temperature followed by a rapid quench using argon or helium gas to the isothermal temperature. Then the specimen will be held at the isothermal temperature until completion of the transformation, followed by a further rapid quench to room temperature. At this point the specimen is ready for further characterisation using methods such as metallography or electron backscattered diffraction (EBSD).

Isothermal experiments were carried out in a Bahr 805D high resolution dilatometer (Fig. 2.1) under high vacuum conditions (10^{-5} mbar) to prevent oxide formation on cylindrical samples 5mm in length and 4mm in diameter.

Figure 2.1 Bahr 805D high resolution dilatometer

To conduct the isothermal experiments, samples were heated with the following multi-step cycle: 1) heating rate (HR) = 14 ºC/s up to 650 ºC; 2) HR = 6.6 ºC/s up to 900 ºC; 3) HR=2ºC/s up to the final austenetization and held for 600 s. The reason for choosing this heat treatment was to simulate other laboratory furnace heat treatments used in the study. After the austenetization heat treatment, samples were quenched with the injection of helium gas to the isothermal temperatures and were held for different times for each experiment. The samples were then further quenched to room temperature.

2.3.2 Continuous heating dilatometry

As mentioned, dilatometry can be used to investigate the continuous heating transformation (CHT). To study the austenite formation kinetics a high resolution dilatometer DT1000 (Fig. 2.2) was employed. To determine the critical transformation temperatures (Ac_1, Ac_3) and follow the transformation kinetics from the dilatometry plots, samples of 12 mm in length and 2 mm in diameter were continuously heated at 0.05, 0.5 and 7 ºC/s up to 1250 ºC. In addition, to determine the critical transformation temperatures, quench interruption methods were performed during the austenetization process to investigate the austenite formation and the effect of additional Al on austenite formation.

Figure 2.2 High resolution dilatometer DT1000

2.4 Thermal etching technique (prior austenite grain size determination)

Revealing austenite grain boundaries can be a difficult task, especially in steels which show low sensitivity to chemical etching. Despite a number of attempts which were made to reveal the prior austenite grain boundaries by chemical etching, few satisfactory results were achieved. Therefore, finding another technique to reveal the prior austenite grain boundaries had to be considered. The thermal etching method has been shown to be effective in revealing austenite grain boundaries [53].

Thermal etching is based on revealing the austenite grain boundaries in a pre-polished surface of the bulk by the formation of grooves at the intersections of austenite grain boundaries with the polished surface. The formation of the grooves takes place when the polished surface is exposed to a high temperature in an inert atmosphere. These grooves decorate the austenite grain boundaries and make them visible at room temperature by light microscopy (Fig. 2.3). Thermal etching results in equilibration of the triple junction between the grain boundary and the free surface [54, 55]. Although there are some uncertainties, especially in the case of mobile grain boundaries, it is believed this technique is reliable enough to be employed in austenite grain size measurements especially in those steels in which we cannot reveal the prior austenite grain boundaries with normal chemical etching.

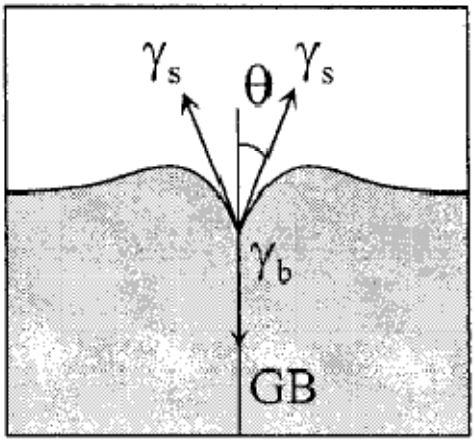

Figure 2.3 Formation of grooves during thermal etching process [55]

To investigate the effect of added Al on prior austenite grain size, cylindrical samples 5 mm in diameter and 12 mm in length were made and a 2 mm wide surface was generated along the longitudinal axis of samples by polishing and finishing with

1 µm diamond paste. These samples were subsequently heated in the furnace of a Bahr D805 high resolution dilatometer at a rate of 14C/s to 650 ºC and then 6.6 ^{o}C/s to 900 ºC followed by 2 ºC/s to different austenetising temperatures and held for 600 sec and then cooled to the room temperature at a rate of 1 ºC/s. This process will reveal the prior austenite grain boundaries which can be examined via optical microscopy.

2.5 Scanning electron microscopy

The microstructures of the heat treated samples were examined by secondary and back scattered imaging using a LEO 1530 Gemini FEGSEM.

Scanning electron microscopy is based on scanning a fine beam of electrons across the specimen and detecting different generated electrons (secondary and back scattered electrons). Secondary electron (SE) images reveal surface topographic information, whereas backscattered electron (BSE) images give contrast due to atomic number variation in the specimen. Analysis of the emitted of X-rays can give elemental composition information.

The interaction volume is defined as the region into which the electrons penetrate the specimen. It should be noted that the interaction volume is determined by the beam energy i.e. the higher the beam energy the larger the interaction volume [56].

The most significant mechanisms for revealing surface topography is secondary electron (SE) imaging. SEs are defined as the electrons which escape from the specimen with energy of around 50 eV. They can be generated not only by the primary electrons entering the specimen but also by escaping back scattered electrons. Due to the energy of secondary electrons, most of the generated SEs are absorbed by the bulk except those generated from the region very near to the surface and therefore the secondary electrons are used to obtain topographic images from the surface of the specimen.

Back scattered electrons are defined as the primary electrons may leave the surface before giving up all their energy. There are not usually as numerous as SEs but in general have higher energy. It should be noted that high energy, back scattered electrons will not be able to escape from a depth more than a fraction of a micrometer. Back scattered electrons (BSE) are employed to achieve atomic contrast image. In addition, they may be used to obtain crystallographic information from the specimen using the technique, electron back scattered diffraction (EBSD) [56].

In addition to the secondary and back scattered electrons, X-rays are generated as a result of the interaction of electron beam with the specimen. Generally, X-rays are used primarily for determination of chemical composition rather than imaging

2.6 Electron backscatter diffraction (EBSD)

Electron backscatter diffraction is a very useful technique in materials characterisation. The development of the EBSD technique started in 1973 with Venables and Harland [57]. The recent introduction of field emission gun SEMs (FEG SEM) giving high current, small spot analysis together with the development of fast acquisition, high resolution digital cameras, have had a dramatic influence on the usefulness of EBSD. It should be noted that many of the structural parameters that control the properties and performance of material, such as grain size, grain size distribution, phase constituents, misorientation distribution, can be investigated by EBSD [57, 58].

2.6.1The EBSD method

The EBSD characterization technique is based on indexing and solving the diffraction patterns (Kikuchi patterns) generated from the interaction of the incident electron beam and the bulk material. Figure 2.4 schematically illustrates how EBSD works.

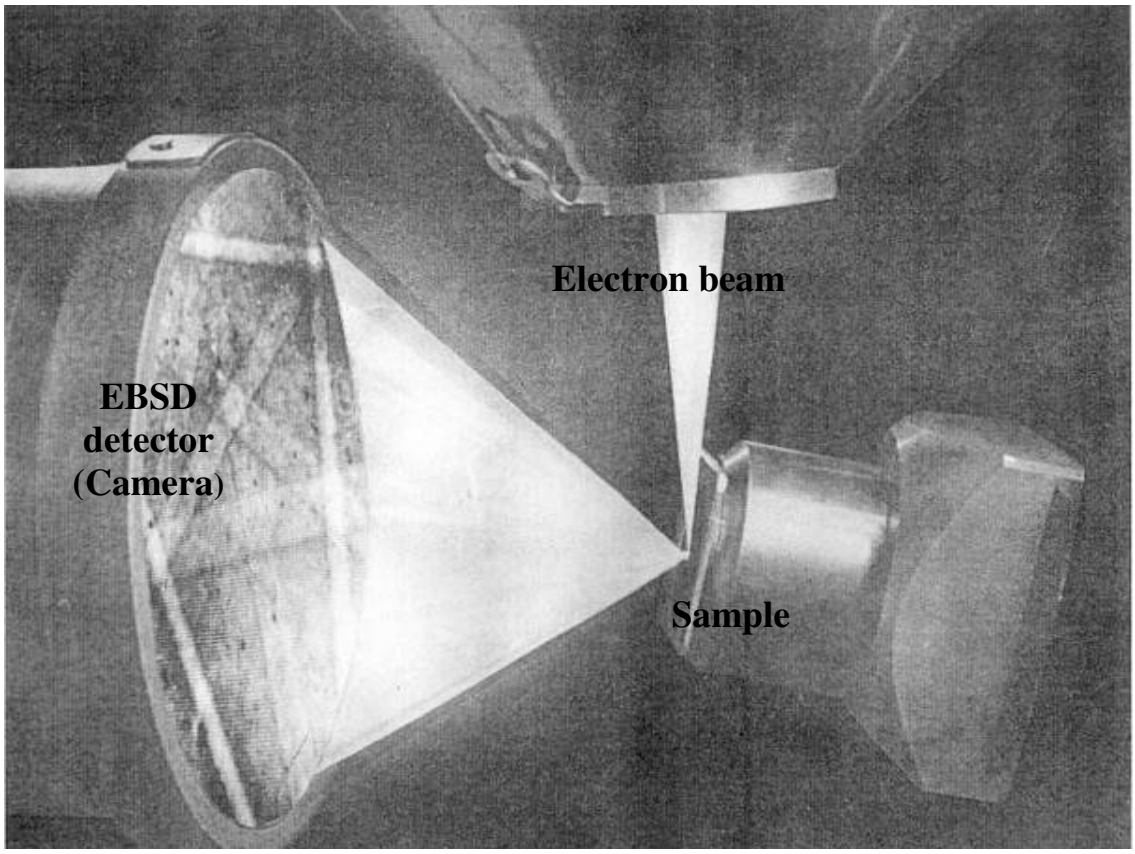

Figure 2.4 Schematic diagram of EBSD within the SEM

The source point of diffracted backscattered electrons is the region on the crystalline sample where the incident beam interacts with the sample. As the backscattered electrons diverge from the source they are diffracted by the crystal planes of the material according to Bragg's law:

$$n\lambda = 2\, d \sin\theta \qquad \text{(Equation 2.2)}$$

Where n is the order of reflection, λ is the wavelength of the electron beam, *d* is the spacing between the crystalline planes and θ is the diffraction angle. At constant wavelength, the *d* spacing due to different sets of crystallographic planes may be

found by analyzing the scattering angle, θ. The Kikuchi diffraction patterns consist of intersecting bands, where each pair of lines represents a lattice plane of the material which is being examined. The width of each band is representative of θ which is inversely proportional to the *d*-spacing of the associated lattice plane. The intersection of these bands is representative of the zone axis and the angle between the bands is the inter-planar angle. i.e. the Kikuchi patterns give information on the complete crystallography of the material at potentially high spatial resolution. A key point with EBSD is to record and analyse the Kikuchi patterns with bands of sufficient quality so that the crystal structure and orientation may be determined accurately. Figure 2.4 shows an example of a Kikuchi pattern.

Before analysis of the patterns begins, details of the crystallographic structures of all possible phases which may be present in the specimen i.e. lattice parameters, space group and atom positions have to be provided. Typically, this information can be obtained from structural databases (e.g. Daresbury Inorganic Structural Database) as a correctly formatted file which may be directly imported into the EBSD software package. Having the crystallography for each possible phase which may be present enables the software to generate theoretical spherically projected Kikuchi patterns for every possible crystal orientation. The software then tries to match these reference patterns with the patterns collected by the camera. If, subject to meeting certain acceptance criteria, the EBSD patterns fit one of the generated reference patterns, then the phase and orientation is determined. Points on the specimen with identical phase and orientation are given the same colour. Hence, a map may be built up whereby the phase and crystal (grain) orientation is shown clearly. Where the match is unsatisfactory then the pixel is shown black.

2.7 Transmission electron microscopy

Transmission electron microscopy (TEM) is used to give information about the internal structure of the specimen. The TEM technique produces images by illuminating the sample by a direct electron beam and detecting the electrons (80-200 keV) which pass through the sample. Each electron passing through the sample has a number of possible fates. The most significant of these are:

-Unscattered electrons (passing through the sample without interaction)

-Scattered electrons (inelastic interaction)

-Electrons which lose significant amount of energy and X-rays may be excited)

Different types of image can be obtained by detecting the transmitted electrons. Furthermore, the TEM may be able to determine phase information via the use of electron diffraction.

TEM can also be used to determine the elemental composition of the specimen. The excited X-rays which result from interactions between the electron beam and the specimen, as in the SEM, can be detected and from a knowledge of their energies can be used to determine the elemental composition. EDX analysis in the TEM has a much higher spatial resolution compared with the SEM, due to the size of electron probe and interaction volume [59].The X-ray spectrum enables us to determine which elements are present in the specimen (at the analysis area) i.e. qualitative analysis. Furthermore, measurement of the number of X-rays which are emitted per second should also give us the information about what proportion of each element is present at the analysis area i.e. quantitative analysis.

One of the most significant issues which should be considered in chemical analysis is the minimum limit of detection for any element in an analysis area. A thorough understanding of the elemental detection limits for EDX in the SEM and TEM is particularly important for these studies as the alloying additions to the steel samples are at low levels. The detectability limit of element A in a matrix of element B is defined by Goldstein [59] as:

$$C_A = 3\frac{(2I_C)^{1/2}}{I_B} \cdot K_{AB} \cdot C_B \qquad \text{(Equation 2.3)}$$

Where C_A and C_B are the weight fraction of any elements and I_B is the intensity from element B and I_C is the continuum background for element A. K_{AB} is the scaling factor which is usually determined experimentally. Goldstein showed that increasing

the count rate or counting time can increase the detectability limit. It should be noted that increasing the counting rate can be obtained only by increasing the specimen thickness or probe size which both deteriorate the spatial resolution. Although the detectability limit differs in different circumstances, generally for the TEM technique it would be assumed to be typically of the order of 0.1-0.5 wt% for a specimen of 50-100 nm thickness [59].

A prerequisite for high quality TEM is a suitably electron transparent specimen, ideally significantly thinner than 100 nm. Hence, specimen preparation is important and for certain materials difficult and time-consuming. The most commonly used method of preparation of thin foils of metallic samples for TEM is electropolishing. However, in this method the user is not be able to locate and define the area of interest for TEM observation i.e. if the user is looking for specific features such as grain boundaries or interfaces between phases it would be difficult to ensure that they are contained within the thin area which has been electropolished. Furthermore, the chance of finding the feature of interest within the thinned region of specimen will be lower when coarse grain structured materials are being examined. Since one of the objectives of the present study is the investigation of the austenite and ferrite interface during the transformation, the Focussed Ion Beam (FIB) technique within the SEM was employed for TEM sample preparation. The FIB method enables the identification of the area of interest within the sample and the accurate preparation of a thin specimen suitable for TEM from this specific area.

2.7.1 TEM sample preparation by FIB-SEM

The FIB-SEM technique was employed to prepare the area specific, thin TEM specimens. The area of interest (e.g. grain boundary) is identified via imaging in the SEM. A thin platinum layer is deposited directly above this area to help reduce damage during the milling step. A focussed beam of gallium ions is then used to mill away bulk material on either side of the intended TEM specimen to create a rectangular section. The gallium ion milling is continued until the section is deemed suitably thin for TEM. The FIB section now needs to be carefully transferred to a suitable TEM grid. This is a delicate step given the fragility of the section. A

tungsten micromanipulator probe is inserted into the SEM chamber. The sample is moved into a position where the probe is touching the side of the milled section. Pt gas injection is used to make a nano weld between the section and the probe and again the gallium ion beam is used to completely detach the section from the bulk. The same technique is used to position the FIB section on the TEM grid. Figure 2.5 shows the sequence of making the FIB section which starts from milling the FIB section to attaching the FIB section to the TEM grid. Figure 2.8 also the shows a confocal microscopy image of the vertical slice of FIB hole after removing the FIB section.

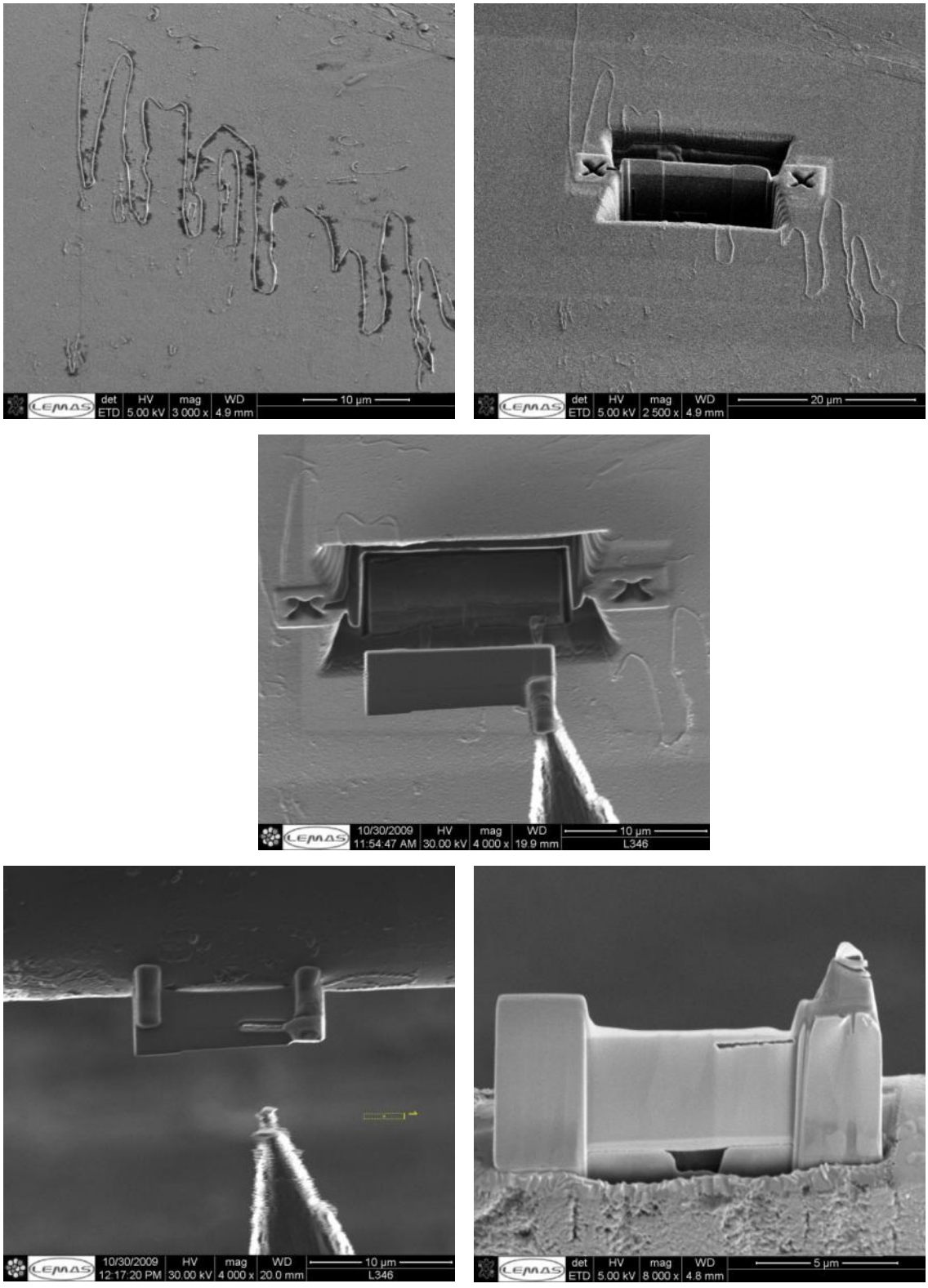

Figure 2.5 The sequence of making a FIB section

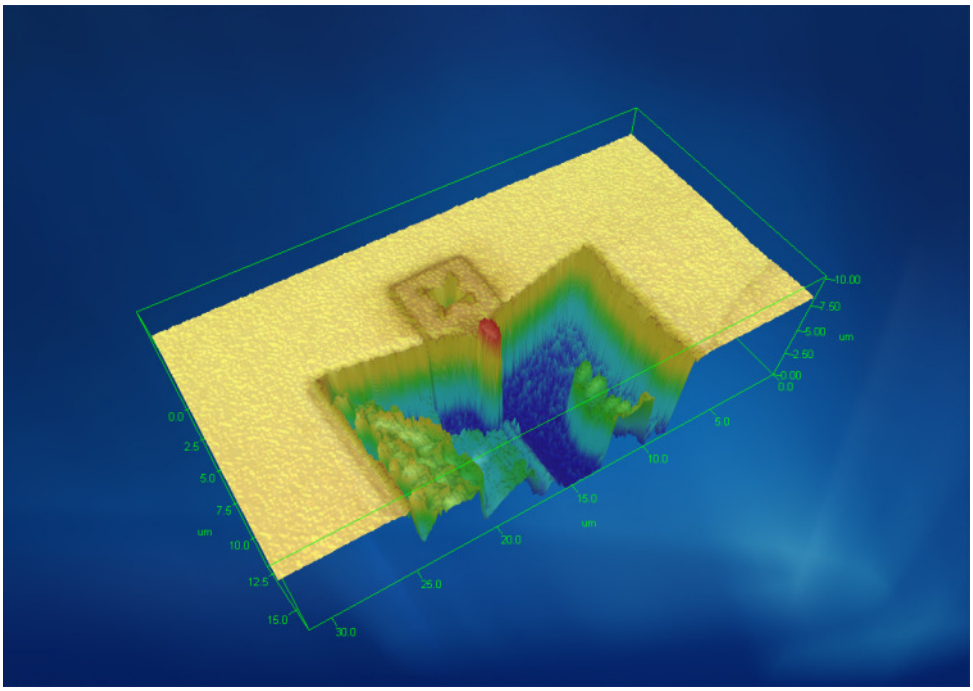

Figure 2.6 A vertical slice of the FIB hole after removing the FIB section (confocal microscopy image)

2.7.2 TEM samples preparation using the carbon replica method

The carbon replica preparation technique was employed to examine the AlN precipitates in the investigated steels. The general principles of the technique are shown in Fig. 2.7. Specimens were polished up to quarter micron diamond paste to obtain the extremely flat surface. Following polishing, the specimen is given a light etch (1% nital) to just reveal the AlN precipitates on the surface. The specimen was washed and dried before the surface was coated with a thin layer of carbon. This was achieved by using a carbon arc source within a vacuum chamber. The next step is to remove the carbon replica, which now contains the precipitates, from the surface. The most efficient way of doing this was found to be by scoring the carbon film with a sharp point into 2-3 mm squares. Then, the specimen was etched with slightly stronger etchant (e.g. 5 % nital) before placing in a dish of water. The carbon replica should now float off onto the water surface and can be picked up by a TEM grid [56].

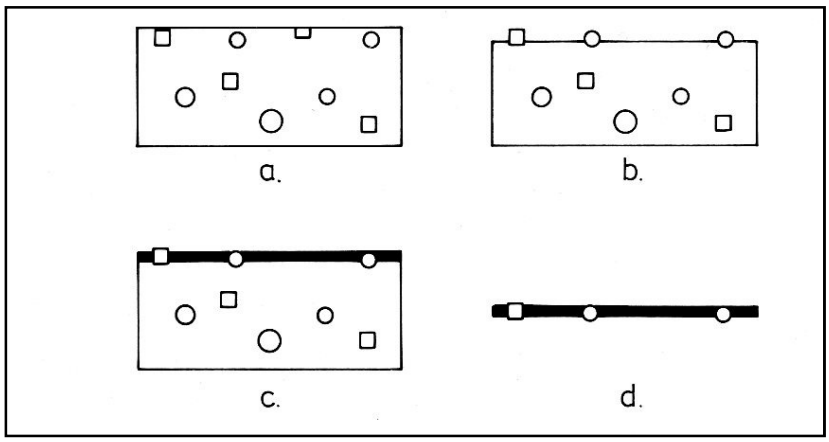

Figure 2.7 The extraction replica method (a) polished surface (b) etched surface (c) carbon coated surface (d) carbon replica containing particles

Chapter 3: The effect of Al alloying additions on as rolled microstructure

Introduction

This chapter will describe the effect of excess Al on the as rolled microstructure, especially ferrite grain size and ferrite grain size distribution, in two different rolling schedules hot rolled (HR) and control rolled (CR). Generally, controlled rolling can be described as a process in which the rolling parameters such as temperature, strain, number of rolling passes, finishing temperature, etc., are predetermined and carefully defined and controlled during rolling process in order to produce a finer structure and consequently higher strength [60]. In contrast, the general idea of hot rolling is rolling the steel as fast as possible with relatively a high soaking and finishing temperature, hence high productivity.

It should be noted that the main effect of the controlled rolled schedule compared to that for hot rolling in the present study, was to obtain a lower finishing rolling temperature (FRT) and allow investigation of the effect on microstructure.

It is well documented that the final ferrite grain size in rolled steels is a function of the following parameters [61-63].

1) Prior austenite grain size; ferrite grains generally nucleate at austenite grain boundaries (surface, edges and corners). Decreasing the austenite grain size leads to a higher density of sites for ferrite nucleation and thus a finer ferrite grain structure.

2) Accumulated strain in austenite grains; it is well documented that the strain accumulates in the austenite grains increasing the ferrite nucleation density. As mentioned above, in un-deformed austenite, ferrite grains generally nucleate at austenite grain boundaries (surface, edges and corners) while in deformed austenite there are additional nucleation sites within the grains such as twins bands and dislocation arrays which can increase the number of suitable sites for nucleation. Thus the accumulated strain as the result of

deformation, below the recrystallisation temperature, leads to a progressive reduction of ferrite grain size.

3) Cooling rate; ferrite grain size can also be a function of cooling rate. An accelerated cooling rate after deformation can lead to a reduction in the ferrite grain size at room temperature.

In addition to the above mentioned parameters, composition can have a considerable effect on the ferrite grain size at room temperature.

To investigate the influence of Al on the as rolled structure, in addition to normal metallography techniques, the electron backscattered diffraction technique was employed to reveal more details of microstructural changes in general and specifically grain structure due to the excess Al content.

Obviously, the size and the shape of grains are generally determined through optical or scanning electron microscopy of etched samples [64]. These methods utilize the fact that grain boundaries (GB) can be made visible through careful etching. The underlying concept of such grain size measurements assumes that GBs are etched to different degrees depending on their energy which is generally thought to be directly related to misorientation angle. Thus, a grain is defined as an area that is surrounded by etched boundaries of a specific minimum misorientation angle and energy. It should be noted that during metallographic investigation in optical microscopy the low energy grain boundaries produce weak contrast and are, in practise, difficult to observe. Moreover, it is generally not known what the minimum misorientation angle is above which boundaries will be etched and below which they are not. Also, the etching procedure may vary slightly from sample to sample. Thus, applying other methods, which could be more reliable and powerful than normal metallography, to reveal the grain structure should be considered.

Therefore, in addition to conventional metallography, the electron backscattered diffraction (EBSD) technique was employed to study the structure of the investigated steels. EBSD is increasingly becoming one of the main characterization techniques for the investigation of crystalline materials. Many of the structural parameters that control the properties and performance of materials can be derived from EBSD data

e.g. grain size, phase constituents, misorientation distribution and microtexture which gives data for modelling and prediction of mechanical anisotropy and residual strain [57, 58, 65]

It should be borne in mind that there are some parameters such as step size, misorientation angle cut off, etc. which can affect the EBSD results. However, due to the size of the ferrite grains in the investigated steels, it can be assumed that the variation of step size will not greatly influence the grain size obtained by EBSD. It is believed that the selected minimum grain boundary misorientation angle can significantly affect the grain size. In fact, a grain is defined as an area completely surrounded by boundaries which have a misorientation greater than the selected minimum grain boundary misorientation angle. Different defined minimum misorientation angles give different grain sizes and consequently different grain size distributions. At present, there is little information in the literature about the effect of minimum misorientation angle (misorientation angle cut off) on grain size measurement and no specific standard. Although there are some limited suggestions and guide lines available among the literature [64, 66], the author preferred to develop his own criteria for interpreting EBSD results since most of the recommended criteria and default settings might be applicable for some materials and conditions but might not suitable for others. The author has investigated the effect of the minimum misorientation angle on EBSD results which can be found in Appendix 1 and concluded that for low carbon hot rolled steel a 10º to 12º cut off misorientation angle would be the best condition to compare the metallography and EBSD results.

In addition to grain size determination, EBSD is able to identify the different phases within the matrix [57, 67]. However, following detailed studies, it was concluded that EBSD could not give accurate, reliable results for identifying phases such as AlN within the ferritic matrix. More details from the results obtained in this regard i.e. the reliability of EBSD results in AlN phase identification, can be found in Appendix 2.

3.1. Experimental methods

Five different steels were prepared by the procedure given in chapter 2. Common metallography preparation (section 2.2) was conducted to prepare the samples for metallography. For further characterization EBSD was undertaken by utilizing Leo 1530 FEG-SEM operated at 30 kV with patterns detected and analysed in real time using an Oxford Instruments camera and associated INCA software. EBSD maps were collected for each sample from the middle of each plate using a step size of approximately 1 μm and a 5 degree misorientation cut off was applied for the purposes of identifying individual grains. In addition, the TEM technique was employed to examine the AlN precipitates.

3.2 Results

The metallography images of samples E, F, G (HR) and L, M (CR) are shown in Fig. 3.1. Figure 3.2 shows the EBSD grain orientation maps for each sample. Table 3.1 shows the average ferrite grain size obtained by EBSD. The mean linear intercept values were calculated from the ASTM numbers determined by the EBSD software via converting equation provided by Gladman [20]. As can be seen from table 3.1 , for the same rolling schedule (HR or CR), increasing Al content leads to a finer ferritic microstructure. Excess Al in the HR condition does not cause a significant change in ferritic microstructure when present in amounts less than 0.5 wt%. However, for the CR condition shows there is a change in ferrite grain size when Al is present at levels of ~0.5 wt%. Although a finer grain structure was expected in the CR as opposed to the HR condition, comparison between steels E and L (both containing 0.02 wt% Al) shows no appreciable difference. However, in Al treated steels (F and M both containing 0.48 wt% Al) a considerable reduction in ferrite grain size can be observed for the CR condition.

Table 3.1 Ferrite grain size determined by EBSD.

Rolling schedule	Steel	ASTM number	Mean linear Intercept (μm)
HR	E	7.1	27.1
	F	7.2	26.5
	G	8.4	17.3
CR	L	6.4	35.5
	M	9.5	11.8

Figure 3.3 compares the ferrite grain area distributions for the investigated steels. Comparison of the ferrite grain area distribution (FGAD) for steels E and F shows little change while the FGAD for composition G shows a narrower and tighter distribution. Apparently, there are finer ferrite grains present in G and the additional Al has eliminated all grains coarser than 3200 μm^2. Figure 3.3b shows the influence of additional Al in the CR condition. The FGAD for M shows a much higher number of small ferrite grains. For instance, for steel M in Figure 3b, 45% of the grains are less than 600 μm^2 in area while there is a much wider range of grain areas for steel L. In contrast, the FGAD of steel L shows a long tail of large grains, hence there is a greater percentage of the overall area fraction in the form of grains coarser than 4400 μm^2. A comparison of steels F and M (Figs. 3.3a and 3.3b) indicates that in the CR condition, as expected we observe as much finer grains and coarse grains are scarce.

Figures 4a and 4b compare the misorientation distribution among investigated steels. The dashed line shows the theoretical distribution for randomly oriented grains provided by Mackenzie [68]. Although the grain misorientation distributions for steels E and F (Figure 4a) are qualitatively similar to that predicted for a completely random orientation of grains, the results do reveal that there is a high proportion of low angle misorientation, particularly for the Al-containing steels G (0.94 wt% Al and HR) and control rolled steels (L and M).

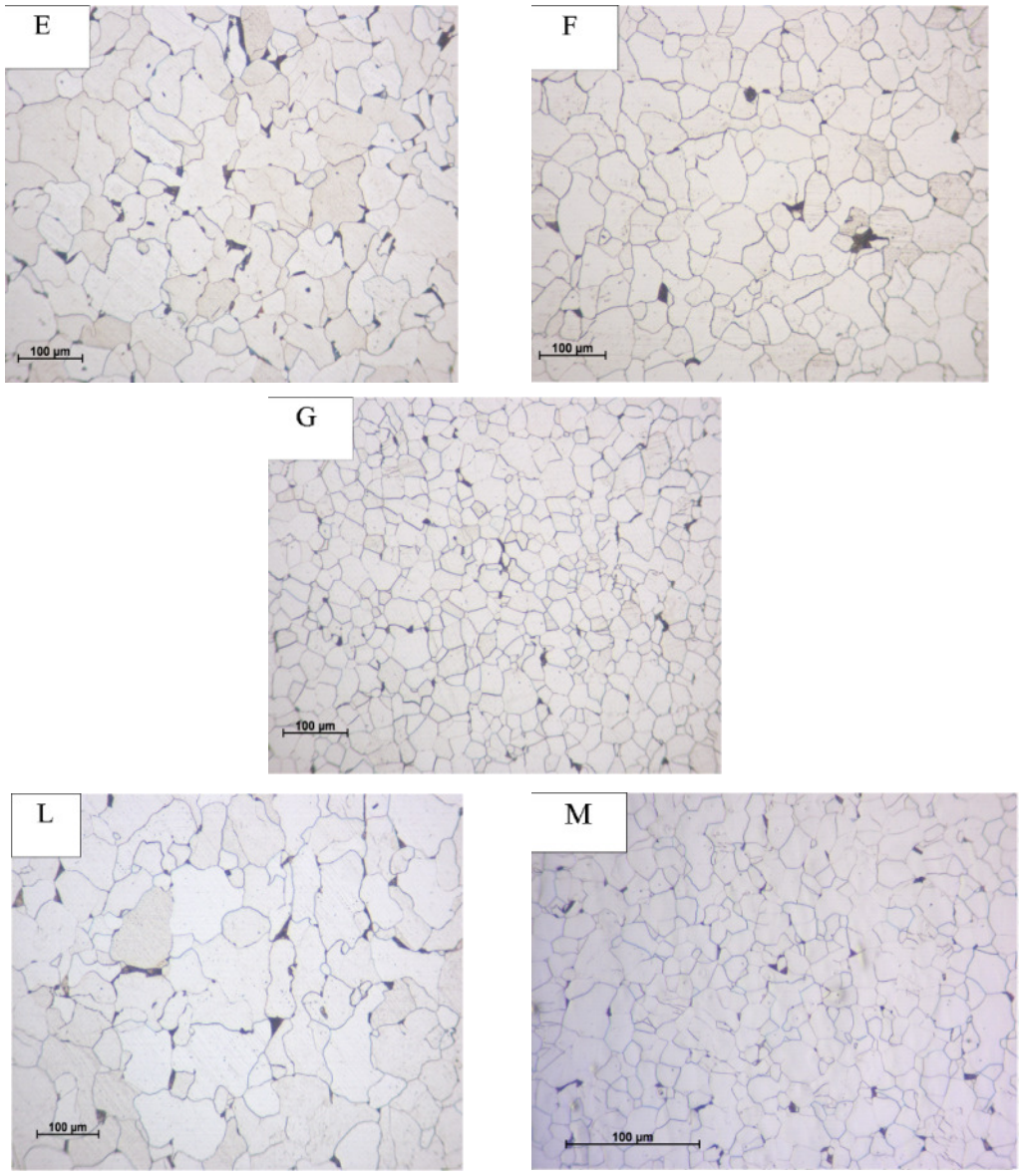

Figure 3.1 Metallography images of samples E, F, G (HR) and L, M (CR)

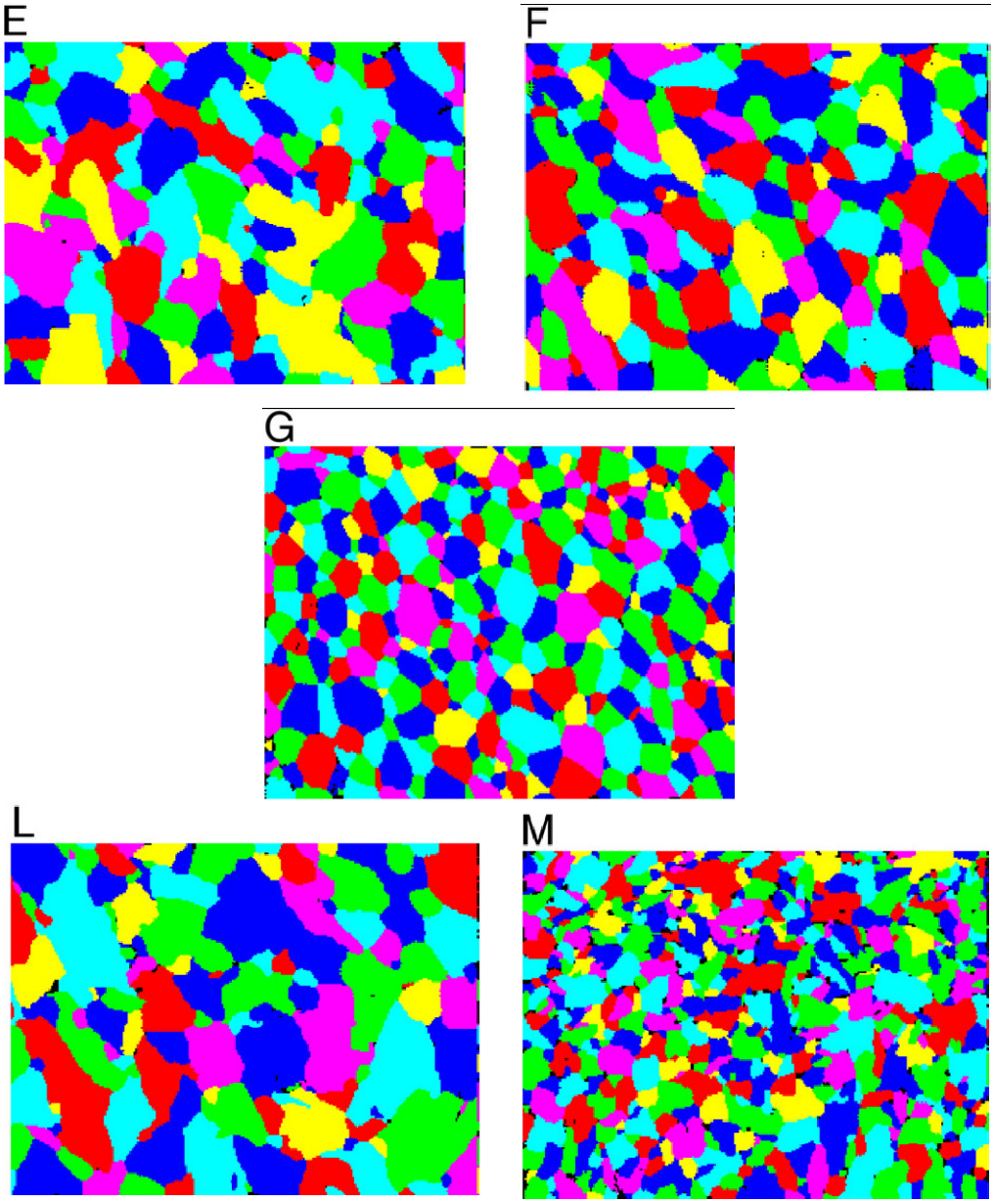

Figure 3.2 EBSD grain orientation maps for each sample

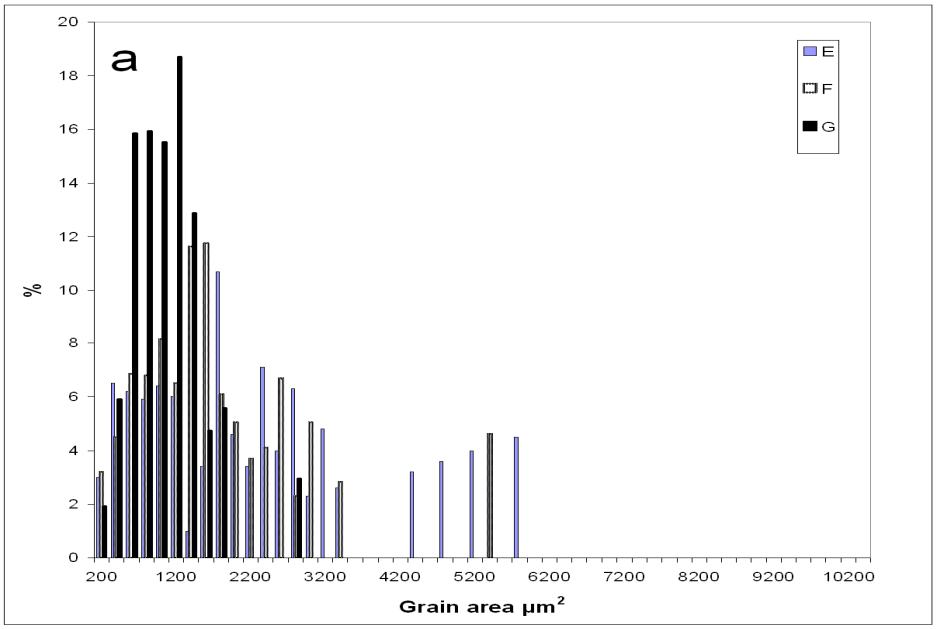

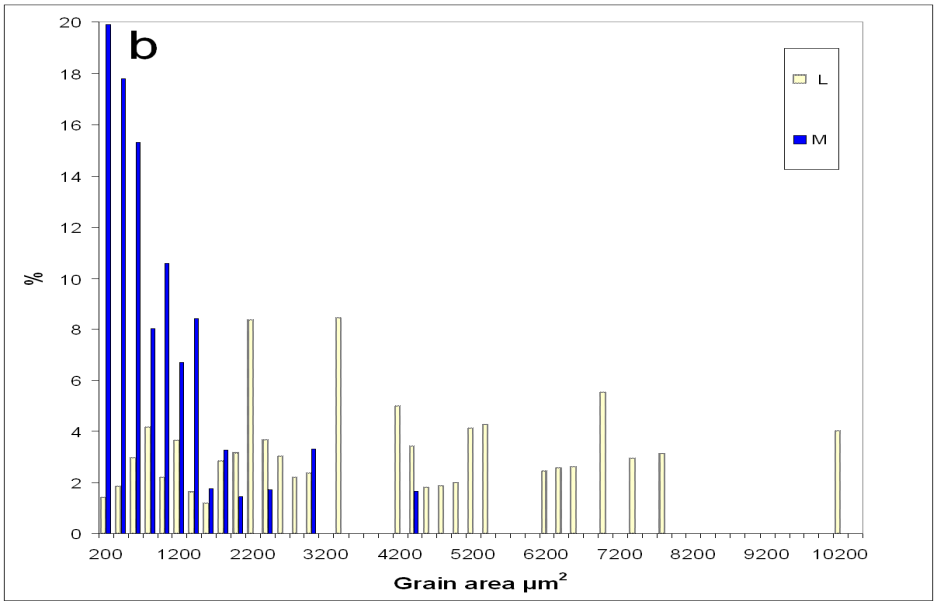

Figure 3.3 Ferrite grain area distributions for steels E, F and G (a) and L and M (b)

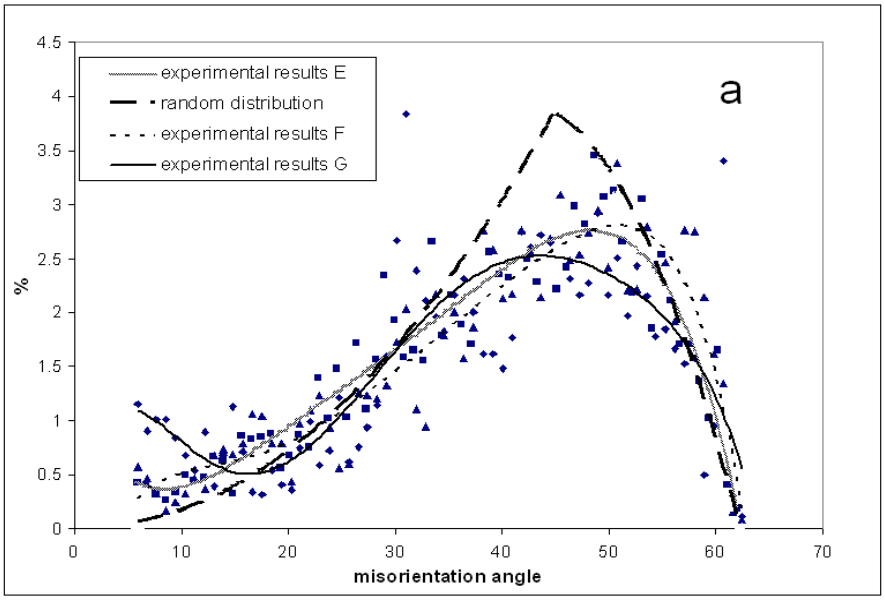

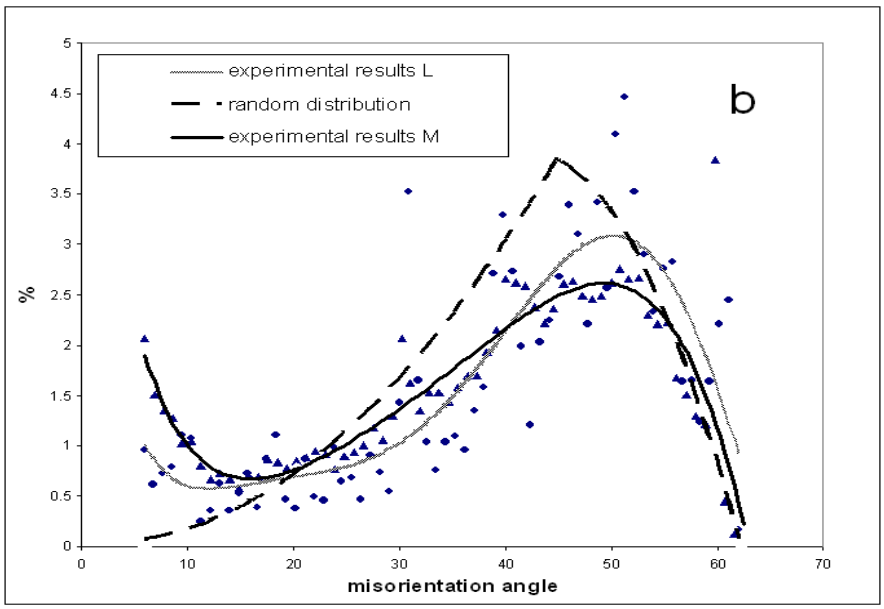

Figure 3.4 Grain boundary misorientation distributions for steels E, F, G (a), L and M (b)

In addition, the presence of any AlN particles, which could lead to grain refinement, was determined via TEM for both Al treated hot rolled samples (F and G). TEM results show that the AlN particle size extracted by the carbon replica technique to be approximately between 350 nm - 500 nm (Figs. 5a and 5b).

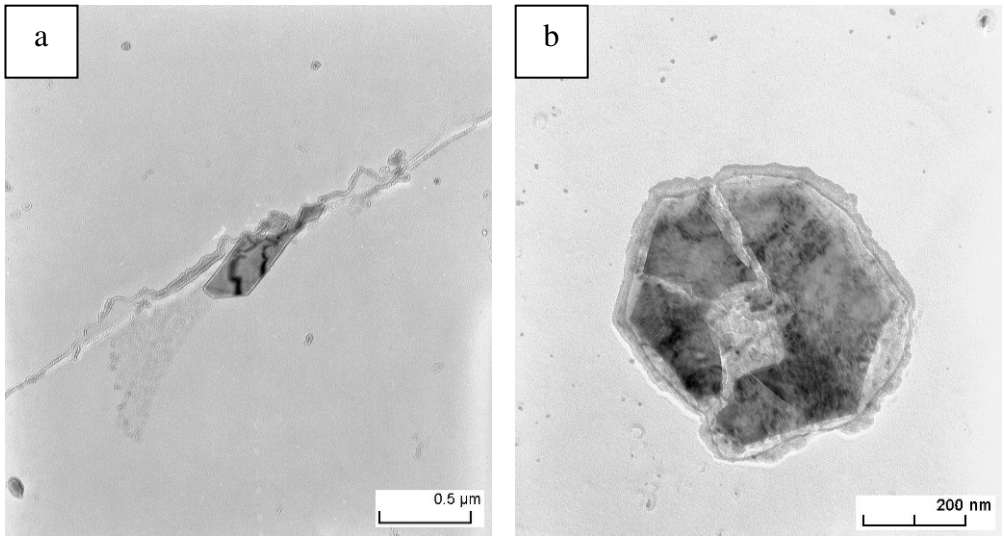

Figure 3.5 TEM micrograph showing AlN particles for the steels F (a) and G (b)

3.3 Discussion

The results show a considerable difference in grain size, grain size distribution and misorientation distribution in the investigated steels. Since there is only one difference, which is the Al content, between the investigated steels, the change in microstructure can be attributed to the presence of additional Al in steels F, M and G. Although the presence of Al in steels could be considered as the influence of AlN on microstructure, it is believed that the observed changes in microstructure cannot be only associated with the presence of AlN particles i.e. pinning effect in the investigated steels.

As explained, the observed changes in microstructure can be associated with the presence of higher amounts of Al in steels F, M and G. It should be borne in mind that there is little in the literature concerning the effect of Al as a solute element (apart from AlN) on ferrite grain size. However, there are some works concerning the effect of additional Al up to 0.3-0.4 wt%, mostly in high Si, magnetic steels. In these afore-mentioned studies, attempts were made to reveal the effect of Al in the range of 0.001-0.4 wt% on ferrite grain size. These studies concluded that the effect of Al on ferrite grain size can be categorized as follows:

1) The effect of Al in amounts between 0.01-0.07 wt%; here, the effect of Al as a grain refiner element has been well established [18]. It is well known that Al can form AlN and inhibit both austenite and ferrite grain growth. This means that by adding Al to a nitrogen containing steel (commercial steels normally contain between 50 and 150 ppm N) a finer ferrite grain size can be obtained.

2) The effect of Al at higher amounts (> 0.07 wt%); there is little in the literature concerning Al additions above 0.07 wt% which is expected since there is no desire by steel makers to produce high Al steels owing to the fact that high Al content can cause lower castability with problems such as nozzle blocking. Also, since Al has not been recognized as a solid solution strengthener, there was no reason for steelmakers to use Al as a deliberate addition to steels except as noted in the introduction. However, information about the effect of additional Al in amounts between 0.1-0.4 wt% can be found [21-24]. Nakamaya and Hojou have shown that by adding 0.07

wt% Al, ferrite grains become finer while the addition of more than 0.1 wt% Al leads to slightly coarser ferrite grains as compared with the Al free steel [21]. They attributed this phenomenon to the effect of additional Al on the size of AlN particles. As they reported, adding more Al to the steel makes the AlN particles coarser. For instance, in a 0.05 wt %Al steel the average AlN particle size observed was 50 nm while in a 0.3 wt% Al steel AlN particles up to 1.2 μm were seen. It is well established in the literature [18] that by increasing the size of AlN, these particles lose their efficiency in contributing to the grain boundary pinning process.

It is worth mentioning that in addition to the role of AlN in controlling ferrite grain size in Al-treated steels (in amounts higher than 0.1 wt%), there are possibly two additional factors which have been ignored in previous studies and need to be considered. These are the effect of Al on the prior austenite grain size, not only as a result of the presence of AlN particles but also more directly as a consequence of Al segregation to prior austenite grain boundaries. Theoretically, Al atoms can segregate to prior austenite grain boundaries which may cause solute drag and consequently affect the prior austenite grain size. In addition to segregation of Al atoms to prior austenite grain boundaries, the influence of Al on critical transformation temperature (Ae_1, Ae_3) and possibly on transformation kinetics might lead to change in ferrite grain structure. It is believed that these two latter factors play important roles in steels with high Al contents (for example 0.5 wt% or more) which will be discussed later. However, as mentioned above, these parameters have been ignored in the previous studies.

Concerning the role of AlN in the investigated steels, the presented TEM results (Fig. 5) are consistent with the previous results of Nakamaya and Saxena [21, 23]. As can be seen, AlN particles in steels F and G are observed to be between 350 and 500 nm in size. This, together with the fact that there are no significant differences in the volume fraction of AlN in steels E, F and G, due to the very low levels of N, leads to the conclusion that the limited number of relatively large AlN particles would not be efficient enough to play a significant role in the determination of the final ferrite grain size.

As already mentioned, alternative interpretations for the appearance of finer ferrite grains in Al containing steels may be associated with the effect of Al on the Ae_3

temperature and also on the accumulated strain prior to the austenite to ferrite transformation. In order to better interpret and understand the results concerning the effect of Al on Ae_3 temperature, obviously we need to determine the Ae_3 temperature for each steel. The critical transformation temperatures for the investigated steels can be determined by using dilatometry. However, the application of a very low heating rate, which is conventionally used for Ae_3 determination, may allow Al atoms to partition into ferrite which would automatically raise the measured Ae_3 due to the fact that Al is a ferrite stabilizer. It is considered that transformation during rolling would take place rapidly at relatively fast cooling rates and therefore there is little prospect for Al partitioning to transforming ferrite austenite interfaces. Calculation of transformation non-partition temperatures using MTData [69] was performed to obtain a better understanding of the results. Table 3.2 shows the Ae_1 and Ae_3 temperatures predicted by MTData for steels E, F and G; it can be assumed temperatures Ae_1 and Ae_3 for steels L, M are the same as those predicted for steels E and F.

The MTData results show that additional Al can raise the Ae_3 temperature and hence the FRT moves closer to Ae_3 in the Al treated steels (F and G). In addition, increasing the Ae_3 leads to there being less time for austenite grain growth after finishing the rolling. Therefore, during cooling after rolling in the higher Al content steels, austenite grains will have less chance to recrystallize and grow before commencing the austenite to ferrite phase transformation and therefore the ferrite grain size can be expected to be smaller for steel G as compared to steels F or E. Also, for the same reason, F and G might have more accumulated strain since FRT moves closer to Ae_3 and, since retained strain plays significant role in the determination of final ferrite grain size, we may expect to get a finer ferrite grain size. A combination of all these phenomena would lead to a finer ferrite grain structure. However, more structured rolling studies would be needed in order to fully understand the whole process.

Table 3.2 Critical no-partition transformation temperatures Ae_1, Ae_3 as predicted by MTData thermodynamic software

Steel	Ae_1 (ºC)	Ae_3 (ºC)
E	679	859
F	691	923
G	709	1053

In addition, the CR samples show a more pronounced effect of additional Al on ferrite grain size in comparison with the HR samples. However, changes in the rolling schedule do not appear to have the same influence for the 0.02 wt% and 0.5 wt% Al containing steels. The results show that controlled rolling of the 0.02 wt% Al steel leads to a slightly coarser average ferrite grain size and also promotes the presence of very large ferrite grains (Fig. 3b). A likely explanation for the reason why steel L was coarser grained after an apparently more 'controlled' rolling schedule (compare with steel E) lies in the rolling schedule used. It should be mentioned that the particular rolling schedule used here for CR had not been optimized for the controlled rolling of steels with such low C contents (being based on studies of Nb steels with carbon contents from 0.05 to 0.15 wt%). During the early development of controlled rolling practices, it has been well documented that the controlled rolling process would not lead to a desirable microstructure unless austenite recrystallisation is properly controlled before the plate temperature falls into the partial recrystallisation region [70, 71]. It is highly probable that in the absence of any effective pinning particle such as AlN, the growth rate of austenite grains would become extremely high. Therefore, holding the material at 1180 ºC and allowing it to fall to 1050 ºC allows the development of some coarse austenite grains which subsequently give rise to coarse grains of ferrite. The appearance of ferrite grains greater than ~5000 μm^2 (Fig. 3b) is consistent with this interpretation.

As mentioned above, the effect of additional Al on ferrite grain size is considerably more pronounced in the CR condition (steel M). The interpretation of this grain refinement in the CR condition could be due to the lower FRT (in comparison with

steel F) which results in higher retained strain and less time for growth and also the effect of Al on prior austenite grain size which could lead to noticeable grain refining.

3.3.1 Ferrite grain misorientation distribution (GMOD)

Regarding the change in the grain misorientation distribution (GMOD) it should be noticed that there appears to be a correlation between a higher number of low angle misorientations and the levels of additional Al in the steel and also controlled rolling (Figs 4a and 4b, respectively). The presence of excess low angle grain boundaries i.e. $< 15^{\circ}$ has been reported in some cases [62, 72]. Priestner and Ibraheem [62] have shown that warm rolling of a Nb steel results in an excess of low angle grain boundaries which are representative of substructure. Table 3.3 and Fig. 3.6 show considerable correlation between the amount of low angle grain boundaries and difference between Ae_3 and FRT for each steel. In the case of our investigated steels it is believed that when Ae_3 becomes close to the finishing rolling temperature (FRT) the amount of low angle grain boundaries increases. For instance, a comparison among E, F and G shows that the steel which has the higher Ae_3 has a higher excess of low angle misorientations. Also, a similar effect is seen for the CR condition. However, it should be noted that comparison between HR and CR grain boundary misorientation distribution (GBMD) results shows that in general CR steels have a greater proportion of low angle boundaries which can be interpreted as a consequence of a lower FRT for this specific type of rolling schedule or in other words, a lower difference between Ae_3 and FRT. Generally, the CR results are consistent with our previous observations on the HR steels and also with those of Priestner and Ibraheem [62]. However, it should be noted that they observed a higher proportion of low angle grain boundaries owing to the specific type of rolling schedule.

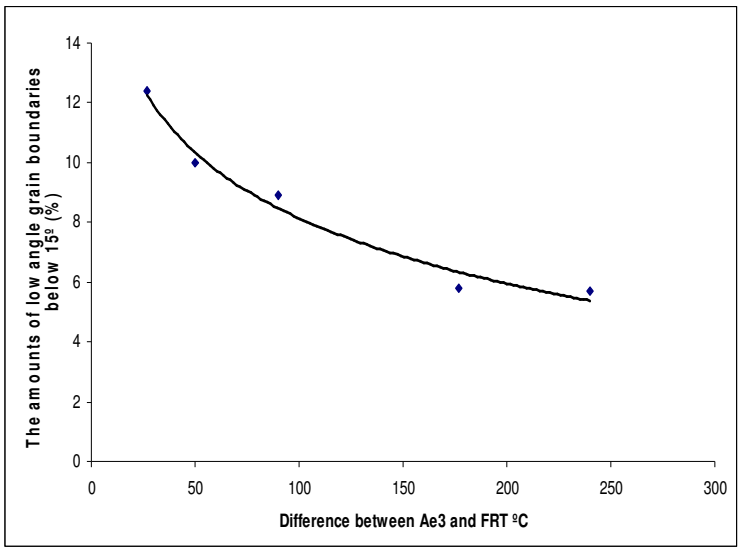

Figure 3.6 Correlation between the amount of low angle grain boundaries and difference between Ae_3 and FRT for investigated steels

Table 3.3 Correlation between the amount of low angle grain boundaries and difference between Ae_3 and FRT for each steel

Steel	Difference between Ae_3 and FRT (ºC)	The amounts of low angle grain boundaries below 15º (%)
E	240	5.7
F	177	5.8
G	50	10
L	90	8.9
M	27	12.4

3.4 Conclusions

The results obtained from the as rolled ferrite microstructure show the strong effect of significant Al additions to ultra-low carbon and nitrogen steels on ferrite grain size. Both the level of nitrogen present in the steels plus TEM observations, lead to the belief that this cannot arise as a consequence of AlN formation. Due to the lack of evidence regarding the effect of Al on prior austenite grain size, ferrite nucleation rate and growth, a comprehensive interpretation of the results cannot be provided. However, the initial interpretations suggest that this grain refinement may be considered to be mainly an effect of aluminium on the Ae_3 temperature and consequently the amount of retained strain in austenite. Also, there is no clear understanding regarding the effect of additional Al on prior austenite grain size which needs to be investigated further.

The other interesting result which needs further consideration is the presence of low grain misorientation angles in Al-containing steels. These results show that the existence of excess low angle grain boundaries not only in Al treated steels but also high levels in those Al containing steels which had undergone controlled rolling. Also, these results can be interpreted as an influence of Al on Ae_3 which leads to a smaller difference between the FRT and Ae_3.

The other interpretation which has not been considered is the effect of Al on ferrite nucleation rate. This could affect the grain structure i.e. final ferrite grain size and grain size distribution. This aspect is more fully described in chapter 6.

It can be concluded that the results and their subsequent interpretation would not be able to provide comprehensive understanding regarding the effect of additional Al in as rolled microstructure in low nitrogen low carbon steel. However they have raised a series of questions concerning the effect of additional Al on austenite formation and grain growth and also the influence of Al on austenite to ferrite transformation (ferrite nucleation and growth) which should be studied to have a better understanding about the effect of Al on as rolled structure. In the next chapters, the effect of Al on the austenetising process (austenite formation and growth) and austenite to ferrite transformation will be investigated.

Chapter 4: The effect of additional Al on austenite formation

Introduction

To investigate the effect of Al on steel microstructure, it is vital to have a broad idea of the role of Al in the austenetization process. It is believed that if Al can influence austenite formation and austenite grain growth it would certainly affect any results from isothermal or continuous transformation experiments. Therefore, without understanding the effect of Al on austenite formation and austenite grain growth, we would not be able to interpret or even design any further transformation experiments (which is essential to understand the effect of Al on as rolled structure). Understanding the influence of the excess Al on austenite formation can also help to obtain more desirable microstructure in high Al added steels such as TRIP steels. As mentioned, in TRIP steels the retention of small austenite islands in the multiphase microstructure leads to an improvement of the mechanical properties. In these steels, it is not only important to study the influence of aluminium on the transformations taking place on cooling, but also on those taking place on heating. Factors such as the initial microstructure and the heating conditions e.g. heating rate, final austenitization temperature, holding time [73-78], as well as proposed theoretical models to predict this transformation [79-82] are required to be studied. In this sense, published experimental observations have shown that:

1) The higher the heating rate applied, the higher the start and finish transformation temperatures (Ac_1 and Ac_3, respectively) this effect being more significant for heating rates >5 ºC/s [78, 83-85]. An empirical equation has been proposed to predict these transformation temperatures as a function of the heating rate and microstructural parameters [83].

2) At temperatures above, but still close to Ac_1, the mechanism of austenite formation may be controlled by substitutional diffusion (mainly Mn or Cr) instead of by volume carbon diffusion, slowing down the transformation noticeably [75-77].

3) The phases present in the initial microstructure before heating (ferrite, pearlite, carbides, martensite, bainite) also influence how the nucleation and growth of austenite takes place [86, 87]. In steels with a ferrite+pearlite initial microstructure, similar to the steels studied in this work, austenite formation takes place via two main steps: first, preferential nucleation at the boundaries of pearlite colonies until pearlite colonies are completely transformed to austenite; this is then followed by the ferrite to austenite transformation which takes place at a much slower rate [74, 75, 88]. However, if cementite particles are present at ferrite grain boundaries and, depending on the heating rate or isothermal conditions applied, nucleation can also take place in these locations at the same time as in pearlite colonies. Consequently, the nucleation rate could be altered and coincident pearlite to austenite and ferrite to austenite transformations could occur.

The aim of this chapter is to investigate the austenite formation process during continuous heating in a wide range of heating rates (0.05 ºC/s – 20 ºC/s) in three investigated steels and also propose a suitable heating cycle for further required experiments i.e. isothermal in order to investigate the effect of excess Al on steel microstructure. The effect of additional Al on austenite grain size will be discussed further in chapter 6.

4.1 Experimental methods

Samples of 12 mm in length and 2-3 mm in diameter were made from three investigated steels. Samples then were continuously heated at rates of 0.05, 0.5, 1, 7 and 20 ºC/s using the high precision furnace of a high resolution dilatometer Adamel Lhomargy DT1000. From the dilatometry plots recorded for every experiment, the start (Ac_1) and finish temperature (Ac_3) of the pearlite+ferrite to austenite transformation were determined. An attempt was also made to establish the temperature at which the dissolution of pearlite finishes (Ac_θ) [84]. To determine temperatures Ac_1 and Ac_3, each experiment was repeated at least three times. A metallographic study was carried out to follow the nucleation kinetics of the transformation. Interrupted heating by quenching experiments were carried out at

different temperatures between Ac_1 and Ac_3 using the furnace of the high resolution dilatometer mentioned above.

4.2Thermodynamic calculations

Thermodynamic calculations have been carried out using MTDATA software [69] to predict the influence of aluminium content on the transformation behaviour of carbon-manganese steels (0.02C-1.41Mn-0.28Si, in wt%). Figure 4.1 shows the simulated equilibrium phase diagram (isopleth "T-x", with "x" the aluminium content) taking a base composition of 0.02C-1.4Mn-0.28Si (in wt%). The aluminium content has been varied over a range from 0 up to 1.0 wt% (slightly above the aluminium content of steel G).

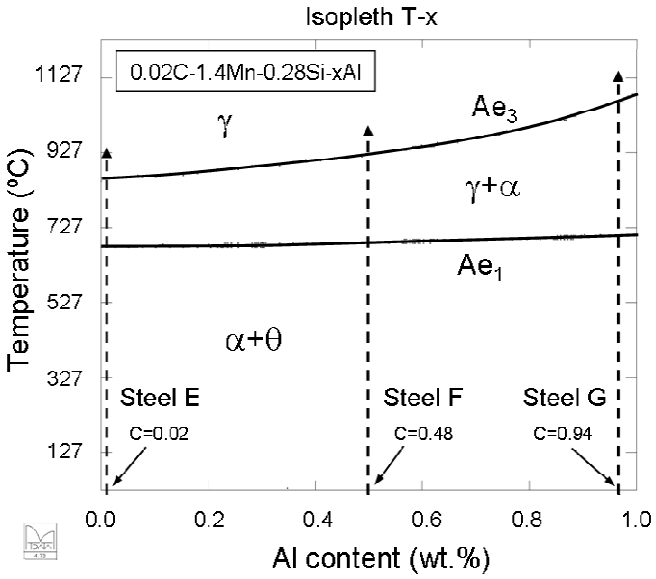

Figure 4.1 Equilibrium phase diagram/Isopleth T-x (=Al) as predicted by MTDATA thermodynamic software for the base composition of the three steels under investigation (0.02C-1.4Mn-0.28Si). Symbols α, γ and θ stands for ferrite, austenite and cementite phase. Solubility lines Ae_3 is the equilibrium temperature for austenite/ferrite transformation

In this diagram, Ae_1 and Ae_3 would correspond to the start and finish temperatures for austenite formation under equilibrium heating conditions. Three dashed arrows inserted in the diagram reproduce the heating path that would be followed by steels E, F and G during an equilibrium heating cycle. In addition to these results, Fig. 4.2 describes the predicted temperature evolution of the mass fraction of austenite, ferrite (αand δ) and cementite.

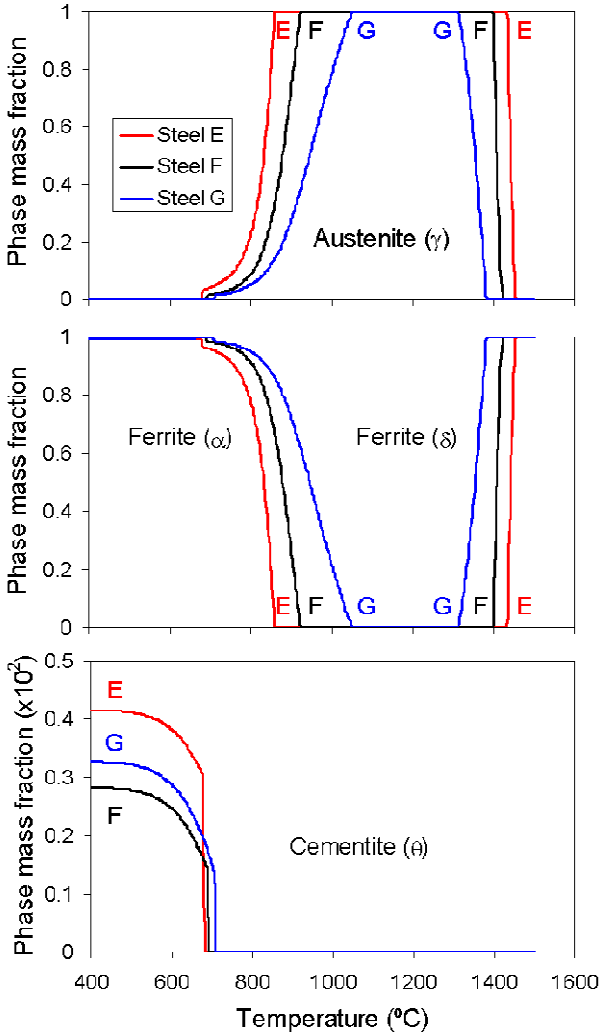

Figure 4.2 Evolution of the equilibrium volume fraction of austenite, ferrite (αand δ) and cementite in the three steel samples under investigation (E, F, G) as predicted by MTDATA.

The exact composition of every steel sample has been used for these simulations. Aluminium has a profound influence on the austenite-ferrite (γ+α) phase field, expanding it and raising drastically the temperature at which a fully austenitic microstructure can be observed (Ae_3). Moreover, the addition of aluminium contracts the γ-phase field by promoting the formation of δ-ferrite. Table 4.1 summarizes the equilibrium transformation temperatures for the start and end of austenite, delta (δ) ferrite (A_δ) and liquidus (A_L) formation (Ae_1, Ae_3, $A_{\delta i}$, $A_{\delta f}$, A_{Li} and A_{Lf}, respectively) for the three steels investigated as predicted by MTDATA.

Table 4.1 Equilibrium start and end temperatures for austenite (Ae_1, Ae_3), delta (δ) ferrite ($A_{\delta i}$, $A_{\delta f}$) and liquid (A_{Li}, A_{Lf}) formation according to MTData predictions.

Steel	Ae_1/Ae_3 (ºC)	$A_{\delta i}/A_{\delta f}$ (ºC)	A_{Li}/A_{Lf} (ºC)
E	679 / 859 ºC	1433 / 1454	1507 / 1526
F	691 / 923 ºC	1397 / 1420	1511 / 1528
G	709 / 1053 ºC	1312 / 1382	1513 / 1530

The addition of 0.94 wt% Al increases $Ae_1$by approximately 30 ºC; while temperature Ae_3 increases by around 195 ºC (Table 4.1).These results predict a significant increase of temperature Ac_3, with a smaller increase in temperature Ac_1, should be expected during continuous heating in the present investigation as the aluminium content of the steels increases (note that under continuous non-equilibrium heating conditions, temperatures Ae_1 and Ae_3 correspond to temperatures Ac_1 and Ac_3 respectively).

Figure 4.3 shows the predicted evolution at equilibrium of the carbon concentration in ferrite (a) and austenite (b) as a function of the heating temperature. The different phase fields are separated using dotted lines. Carbon solubility in ferrite reaches its maximum ($C^{\alpha}_{\max}$) around temperature Ae_1 and this value increases with the aluminium content of the steel (Fig. 4.3a). Figure 3b shows that as the transformation evolves with temperature and the volume fraction of austenite increases, the average carbon concentration of austenite decreases gradually from a maximum value ($C^{\gamma}_{\max}$) at temperatureAe_1, to the nominal carbon composition at temperature Ae_3.

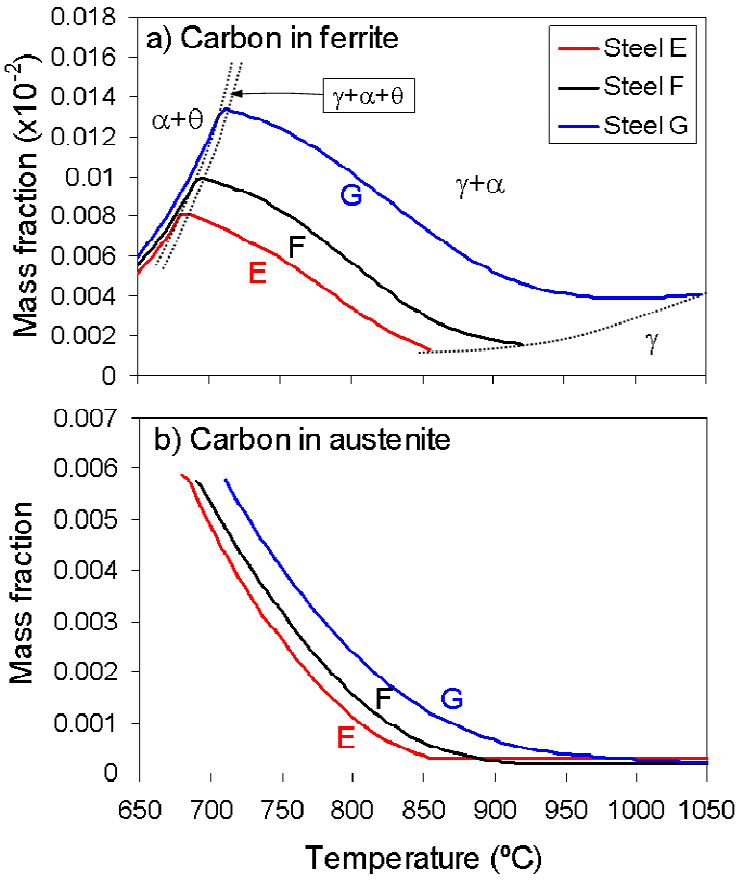

Figure 4.3 Evolution of the carbon mass fraction in a) ferrite and b) austenite for steels E, F and G as predicted by MTDATA. The dotted lines in a) separates the location of different phase fields.

Table 4.2 gives the maximum solubility of carbon in ferrite ($C^{\alpha}_{\max}$) and austenite ($C^{\gamma}_{\max}$) for the three steel samples. In addition, Figure 4.4 represents the evolution of the aluminium concentration in ferrite as a function of the heating temperature.

Table 4.2 Maximum carbon concentration of allotriomorphic ferrite for steels E (679 °C), F (691 °C) and G (709 °C) as predicted by MTData. The carbon composition of the steel is referred to as C_N in this table.

Steel →	E Al %	F Al %	G Al %
$C^{\alpha}_{\max}$ (wt-%)	0.0081	0.0099	0.0133
$C_N - C^{\alpha}_{\max}$ (wt-%)	0.0199	0.0091	0.0087
$C^{\gamma}_{\max}$	0.589	0.575	0.579

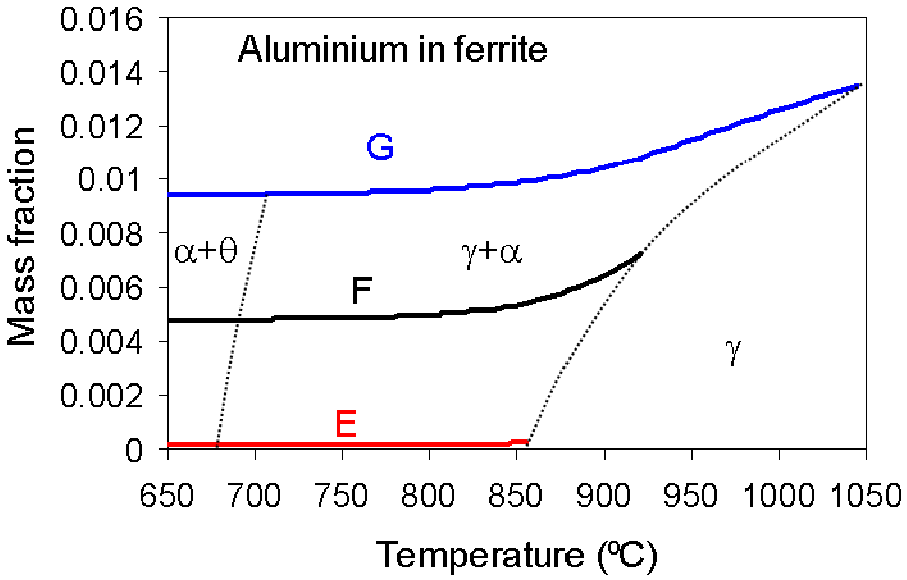

Figure 4.4 Evolution of the aluminium mass fraction in a) ferrite for steels E, F and G as predicted by MTDATA. The dotted lines separate the location of the different phase fields.

Under equilibrium conditions, the aluminium concentration in ferrite increases as temperature Ae_3 is approached, which would contribute to the stabilization of this phase. This enrichment increases with the aluminium content of the steel. However, under non-equilibrium heating conditions, it would be expected that the partitioning of aluminium between both phases during the transformation would not take place or would happen to a lower degree, reducing this aluminium enrichment.

4.3 Results

4.3.1 Initial Microstructure

The microstructure of the steels in the as-received condition is mainly ferritic with some pearlite islands (Fig. 4.5 a, c, e). Cementite particles have been observed located at ferrite grain boundaries in the three steels samples (Fig. 4.5 b, d ,f). The volume fraction of pearlite colonies (f_p) measured experimentally and estimated with MTDATA is given in Table 4.3. More detail regarding the initial microstructure of these steels can be found in chapter 3. The experimental determination of the volume fraction of pearlite has been carried out taking into account only the black islands visible in the optical micrographs (Fig. 4.5 a, c, e). The fact that many cementite particles are present at ferrite grain boundaries might explain the discrepancy between the experimental and predicted values of pearlite volume fraction (Table 4.3). During heating, austenite nucleation takes place preferentially at those locations where carbon is present (in ferritic-pearlitic microstructures nucleation starts in pearlite). The existence of cementite particles at ferrite grain boundaries could influence the austenite formation kinetics since they can act in addition to pearlite, also as sources for the nucleation of this phase.

Table 4.3 Volume fraction of pearlite present in the initial microstructure, determined experimentally and predicted by MTData of the three steel samples **under investigation.**

Steel →	E	F	G
f_P (exp)	2.4±0.3	1.1±0.1	1.4±0.2
f_P (MTData)*	2.8	1.9	2.2

***f_P values were deduced from predicted cementite volume fraction (MTData) by considering that the fraction of cementite in pearlite is 0.15.**

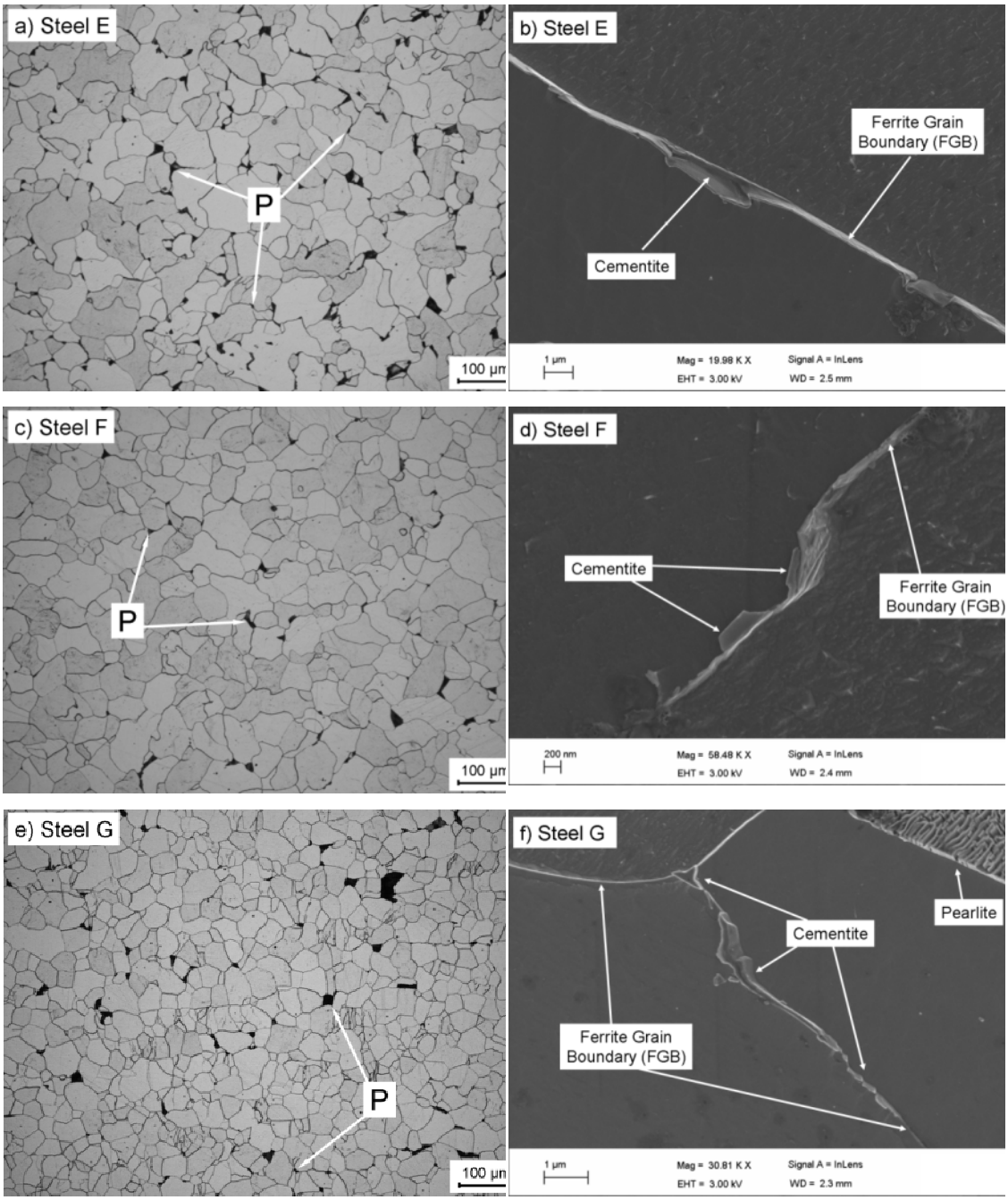

Figure 4.5 Optical micrographs showing the initial microstructure of steel samples E, F and G. In a, c and e, the grey matrix is ferrite and the black islands, pointed out with arrows, correspond to pearlite (P). Scanning electron micrographs in b, d and f show the presence of cementite at ferrite grain boundaries (FGBs). Microstructures have been revealed with Nital-2% etching solution.

4.3.2 Austenite formation. Dilatometry measurements

Figures 4.6 a-c show typical dilatometry plots (relative change in length ($\Delta l/l_0$) vs. temperature) recorded during continuous heating at different rates (0.05, 0.5, 1, 7 and 20 ºC/s) for steels E (a), F (b) and G (c). The determination of the critical temperatures from the dilatometric plots has been conducted considering that Ac_1 corresponds to the temperature at which the expansion deviates from linear behaviour during heating and the sample starts to contract due to the austenite formation; whereas Ac_3 is the temperature at which expansion begins again to depend linearly on temperature once the sample is fully austenitic. Since some investigations have experimentally shown that a separation can be made between pearlite to austenite and ferrite to austenite transformations in low and medium carbon steels [74, 76, 84, 89, 90] an attempt was made to determine the temperature at which this occurs (Ac_θ) from the dilatometry plots. The determination of Ac_θ can be generally attempted if a first contraction due to pearlite dissolution is clearly perceived [81]. Although no clear sharp contraction associated with the start of pearlite to austenite transformation is visible compared to previous studies in higher carbon steels [84], a change in the slope of $\Delta l/l_0$ assumed here to be associated with the nucleation of austenite from pearlite, is observed in all plots. This change is much easier to identify in steel E (Fig. 4.6a) compared to steels F and G (Fig. 4.6 b, c).

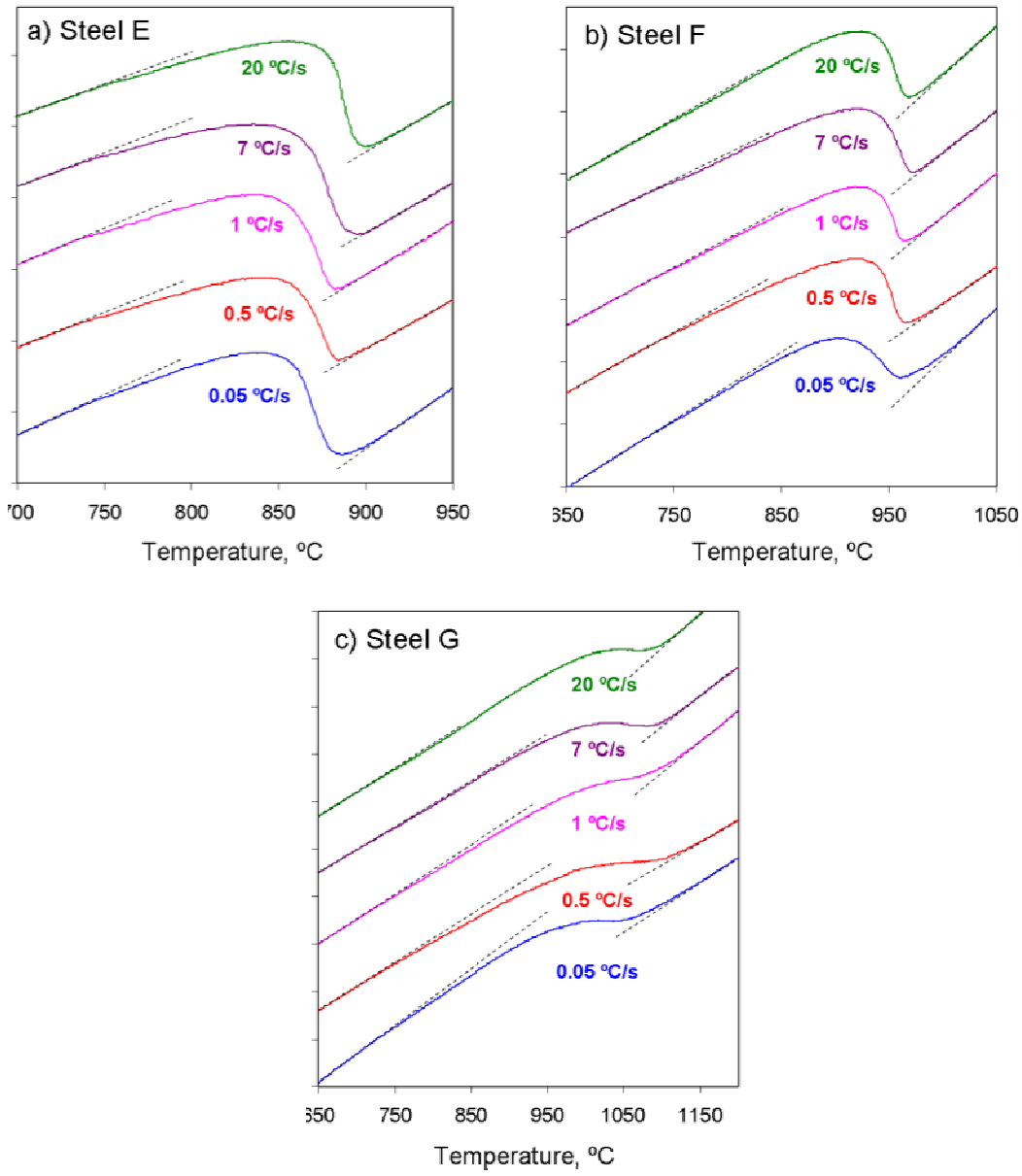

Figure 4.6 Typical dilatometry plots obtained after heating at different rates (0.05, 0.5, 1, 7, 20 ºC/s) for steels E (a), F (b) and G (c). Y axis has been removed since curves have been displaced in Y axis.

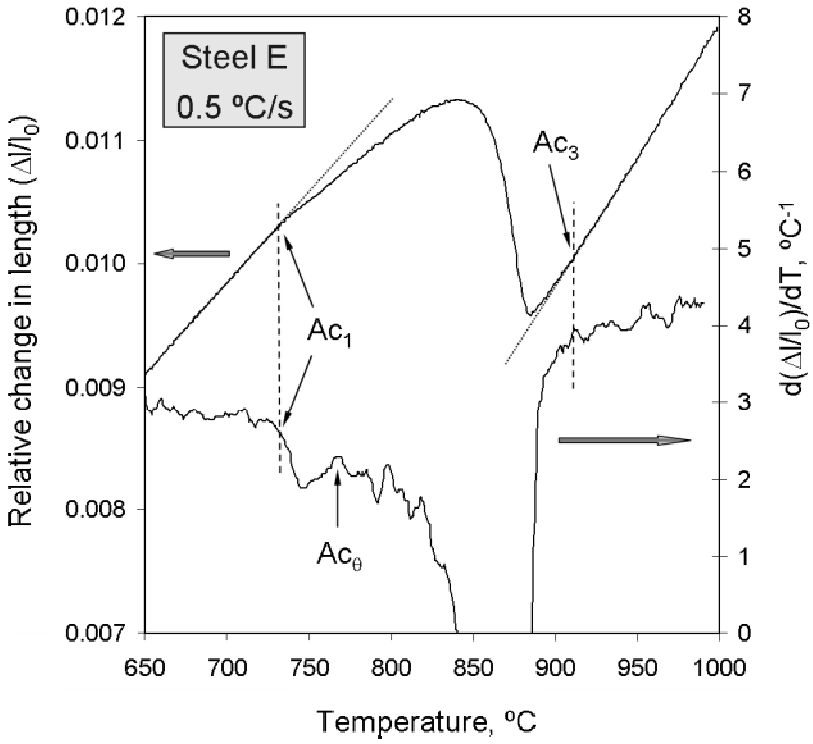

Figure 4.7 Relative change in length ($\Delta l/l_0$) and its temperature derivative ($d(\Delta l/l_0)/dT$) for steel E after heating at a) 0.5 ºC/s and b) 7 ºC/s. The approximate location of the three critical transformation temperatures (Ac_1, Ac_θ and Ac_3) derived from this plots is shown.

To help in the determination of temperature Ac_1 and, primarily, Ac_θ, the temperature evolution of $d(\Delta l/l_0)/dT$ has been used. As an example to explain how this dilatometry analysis has been carried out. Figure 4.7 shows the temperature dependence of ($\Delta l/l_0$) and ($d(\Delta l/l_0)/dT$) for steel E during heating at 0.5 ºC/s. In this plot, the representation of $d(\Delta l/l_0)/dT$ with temperature helps to identify the critical transformation temperatures (pointed out by arrows). However, this approach to determine Ac_θ could be only attempted successfully in steel E under all heating conditions, but not in steels F and G due to the lack of a clear change of slope. In light of these results, to ascertain the location of temperatures $Ac_1$and Ac_θ, requires the mandatory metallographic inspection of the microstructure of quenched samples. The location of temperature Ac_3 is much easier to determine from the dilatometry plots. Table 4.4 summarizes the values of Ac_1 and Ac_3 estimated from the dilatometry plots. Temperature Ac_θ was estimated only for steel E. For comparison of the results obtained for the different steels, the continuous heating transformation

(CHT) diagram is presented in Fig. 4.8. These results show that aluminium has a significant influence on raising temperature Ac_3, while Ac_1 remains almost unaffected. Some recent works has shown that the further the heating conditions are from equilibrium, the higher temperature Ac_3 [91]; however, in the aluminium alloyed steels, the heating rate seems to have the opposite effect, raising temperature Ac_3 for lower heating rates. In steel F this effect is only visible for heating rates ≤7ºC/s.

Finally, under heating conditions closer to equilibrium (0.05 ºC/s), it can be observed (Table 4.4) that the difference between Ac_3 transformation temperatures is 240±17 ºC, which is similar to the value predicted by MTDATA (~195 ºC). In addition, the difference between Ac_1 transformation temperatures is 20±13 ºC, which again is consistent with the MTDATA (~30 ºC) prediction.

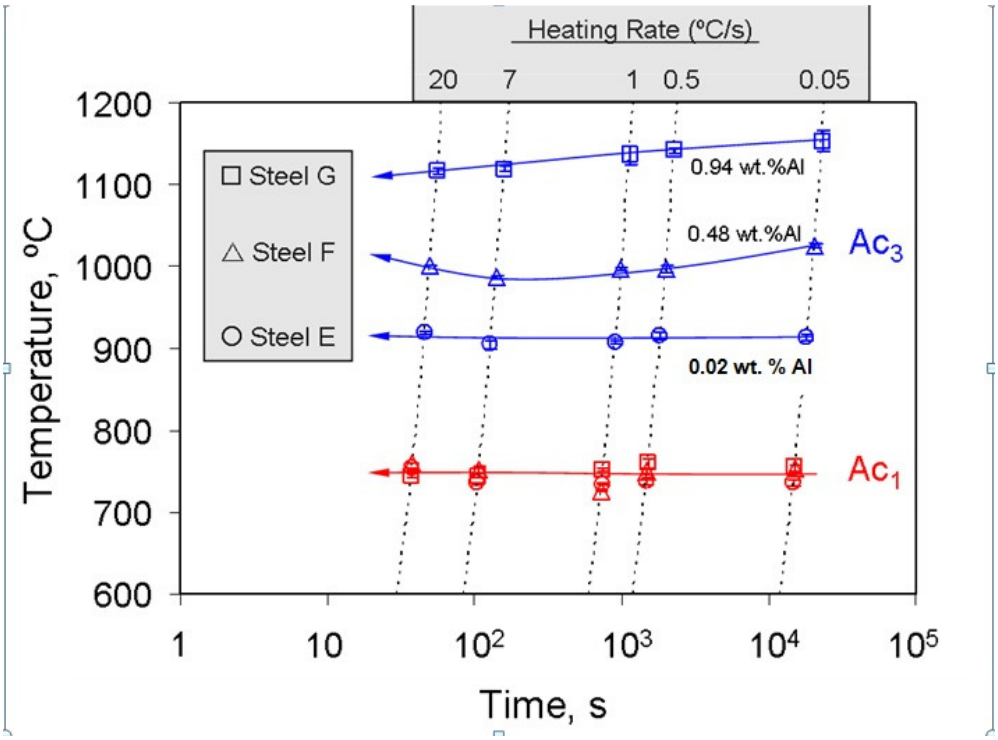

Figure 4.8 Continuous Heating Transformation (CHT) Diagram including the results of the three steels investigated. Symbols Ac1 and Ac3 stand for the start and finish of austenite formation. The solid arrows represent a guide to the eye.

Table 4.4 (Ac_1) and (Ac_3) temperatures for austenite formation on heating, experimentally obtained for different heating schedules, compared with MTData thermodynamic predictions.

	Heating rate, ºC/s	Steel E	Steel F	Steel G
Ac_1	0.05	736±4	754±4	756±9
	0.5	738±4	749±4	759±8
	1	734±1	747±5	752±2
	7	735±1	751±4	744±2
	20	753±1	760±1	744±3
Ac_θ	0.05	758±1	-	-
	0.5	760±1	-	-
	1	758±1	-	-
	7	764±4	-	-
	20	774±3	-	-
Ac_3	0.05	913±4	1025±3	1153±13
	0.5	915±4	997±4	1141±4
	1	906±2	997±4	1136±11
	7	904±5	987±2	1118±3
	20	919±2	1000±1	1116±3

4.3.3 Austenite formation; metallographic analysis

The general approach to estimate the kinetics of austenite formation in low-alloyed carbon steels is by quenching the high temperature austenitic microstructure using high cooling rates. This way the austenite present transforms to martensite and the volume fraction of this latter phase can be regarded as equal to the volume fraction of austenite. On the other hand, it is also well-known that low-carbon steels have a low hardenability, and this property is enhanced by the presence of ferrite stabilizers like aluminium. This could make it very difficult to avoid the formation of ferrite/bainite even applying high cooling rates. If we cannot ensure that austenite has decomposed only into martensite during quenching, the estimation of the austenite volume fraction can result in significant errors. Thus a careful analysis of the dilatometry plots has to be carried out after the quench-out experiments before undertaking any metallographic work to ensure that no austenite has transformed to ferrite/bainite during cooling.

Several quench-out temperatures were selected in the range between Ac_1 and Ac_3 ($\alpha+\gamma$ phase field). Samples were continuously heated up to the selected temperatures and quenched to room temperature at rates around 280-300 ºC/s by a helium gas flow. Figure 4.9 a-c shows characteristic dilatometry plots recorded during quenching after heating at 0.5 and 7 ºC/s to different austenitization temperatures ($T_{\alpha+\gamma}$) in the $\alpha+\gamma$ phase field for the three investigated steels. Temperatures $T_{\alpha+\gamma}$ are given for each dilatometry plot in the figure. As temperature $T_{\alpha+\gamma}$ approaches Ac_3, the average carbon content of austenite decreases significantly, as predicted by MTDATA (Fig 4.3b) and as a consequence the hardenability also decreases. It is clear that an expansion during cooling is detected in all the steels after austenitizing at temperatures well below Ac_3. Those samples in which a ferrite/bainite formation has been formed during quenching are unacceptable for metallographic analysis since it might become difficult to differentiate between untransformed ferrite/bainite that was present in the initial microstructure and ferrite that was formed upon quenching. Thus, the metallographic work was restricted only to a range of temperatures between the nucleation temperature (Ac_1) and volume fractions <0.2-0.3 depending on the steel.

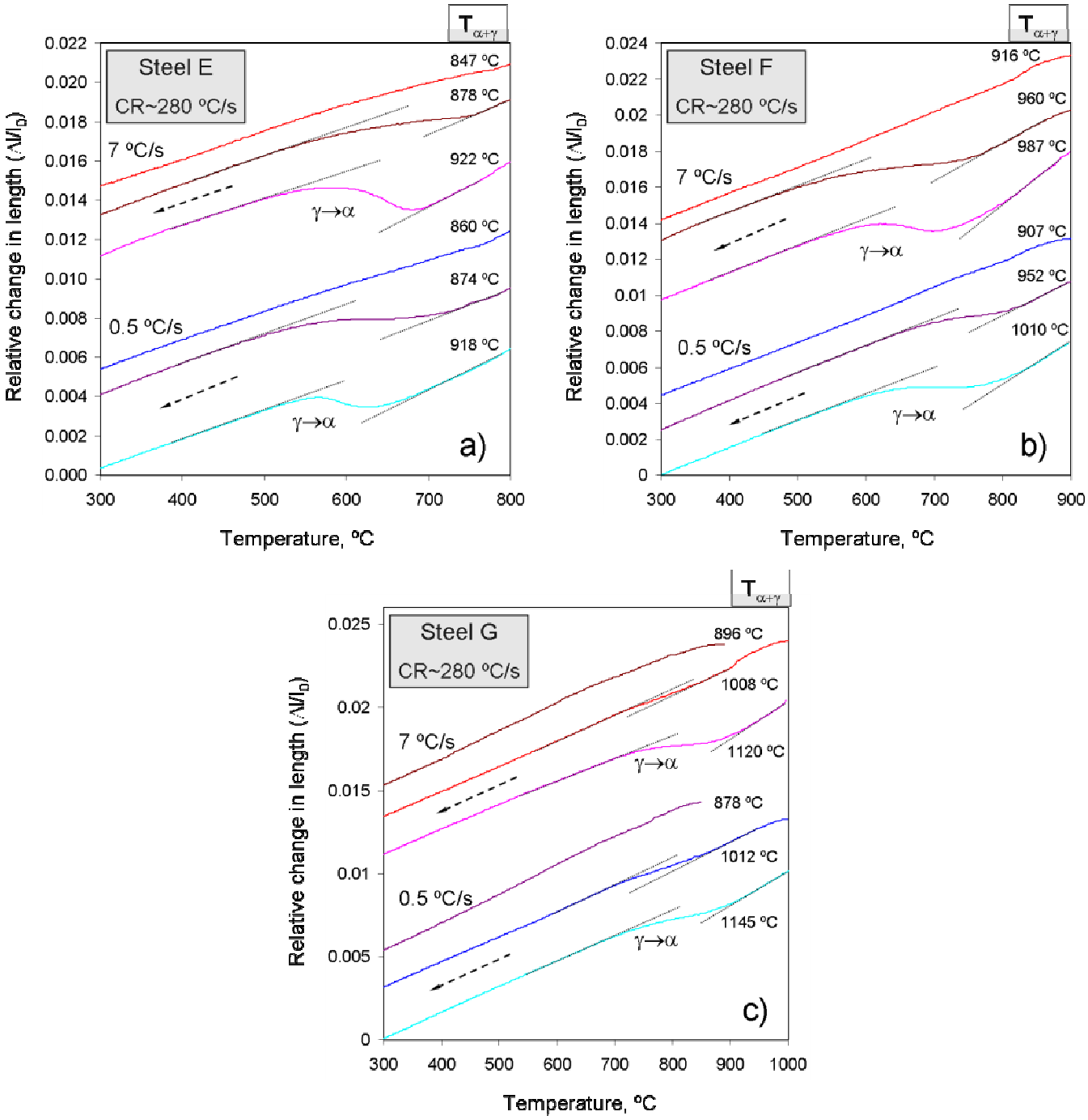

Figure 4.9 Dilatometry plots recorded for the steels E (a), F (b) and G (c) during quenching after heating at two heating rates (0.5 °C/s and 7 °C/s) to different austenitization temperatures ($T_{\alpha+\gamma}$) in the α+γ phase field. The symbols α and γ stands for ferrite and austenite phase; CR stands for cooling rate.

Figures 4.10-4.15 illustrate scanning electron and light optical micrographs showing the nucleation and growth of austenite for the three steels investigated and after heating to different temperatures ($T_{\alpha+\gamma}$) and quenching to room temperature. Two

very different heating rates (0.5 ºC/s and 7 ºC/s) are compared. As was pointed out above, this study was restricted to the initial stages of the transformation.

Several conclusions can be extracted from the metallographic results shown in these figures:

1) Slow heating rates (<1 ºC/s) promote the spheroidization and dissolution of cementite lamellas inside pearlite. This effect is more pronounced in the aluminium alloyed steels.

2) In every steel sample, the partial dissolution of pearlite during slow heating compared to fast heating although reducing the number of nucleation sites (cementite), does not have a significant effect on austenite nucleation (see Table 4.4). However, from the comparison of the three steel samples, the micrographs show that aluminium addition contributes to the dissolution of cementite during slow heating (<1 ºC/s) as Ac_1 is approached, delaying the nucleation of austenite (compare also the values given Table 5).

3) The growth of austenite is clearly affected by the heating rate applied since slow rates promote the growth of austenite along ferrite grain boundaries. For higher heating rates, the growth is initially restricted to the former location of pearlite colonies and small growth along ferrite grain boundaries is observed. Growth along ferrite grain boundaries is more significant in aluminium alloyed steels.

4.4Discussion

4.4.1 Influence of heating rate on the pearlitic microstructure

Figure 16 represents schematically how the dissolution/spheroidization of pearlite has been observed to take place during a slow heating process in the steels investigated. The extent of dissolution depends on the heating rate and aluminium content of the steel. As the temperature increases and reaches Ac_1, the lamellar structure of cementite starts spheroidizing and also dissolving. In addition, we have observed cementite particles at the boundaries of pearlite colonies and even at

locations close to the pearlite (see Fig. 4.10a, in steel E, for example). It is not clear if these particles have precipitated at these locations or are the result of the spheroidization process of the lamella cementite during heating. In addition, during the initial stages of the austenite nucleation, an increase in the nucleation of cementite particles at ferrite grain boundaries has been observed. As pointed out before, the amount of carbon that goes into solution during heating increases with a slower heating rate and a higher aluminium content of the steel.

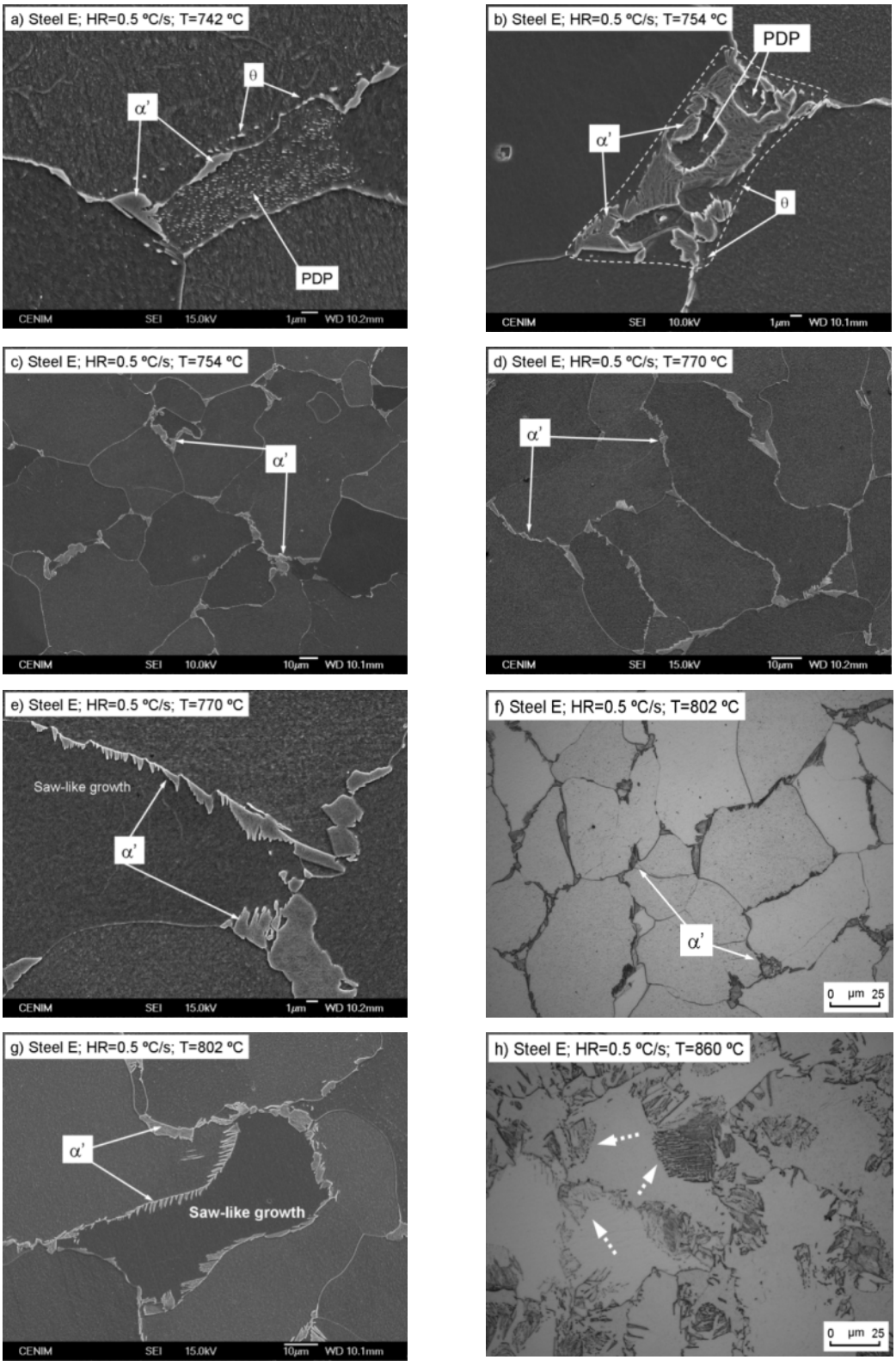

Figure 4.10 Scanning electron and light optical micrographs obtained in steel E after interrupted heating by quenching. Heating rate (HR) of 0.5 ºC/s to 742 ºC (a), 754 ºC (b, c), 770 ºC (d, e), 802 ºC (f, g), 860 ºC (h). Symbols α', θ and PDP stands for martensite, cementite and partially dissolved pearlite respectively.

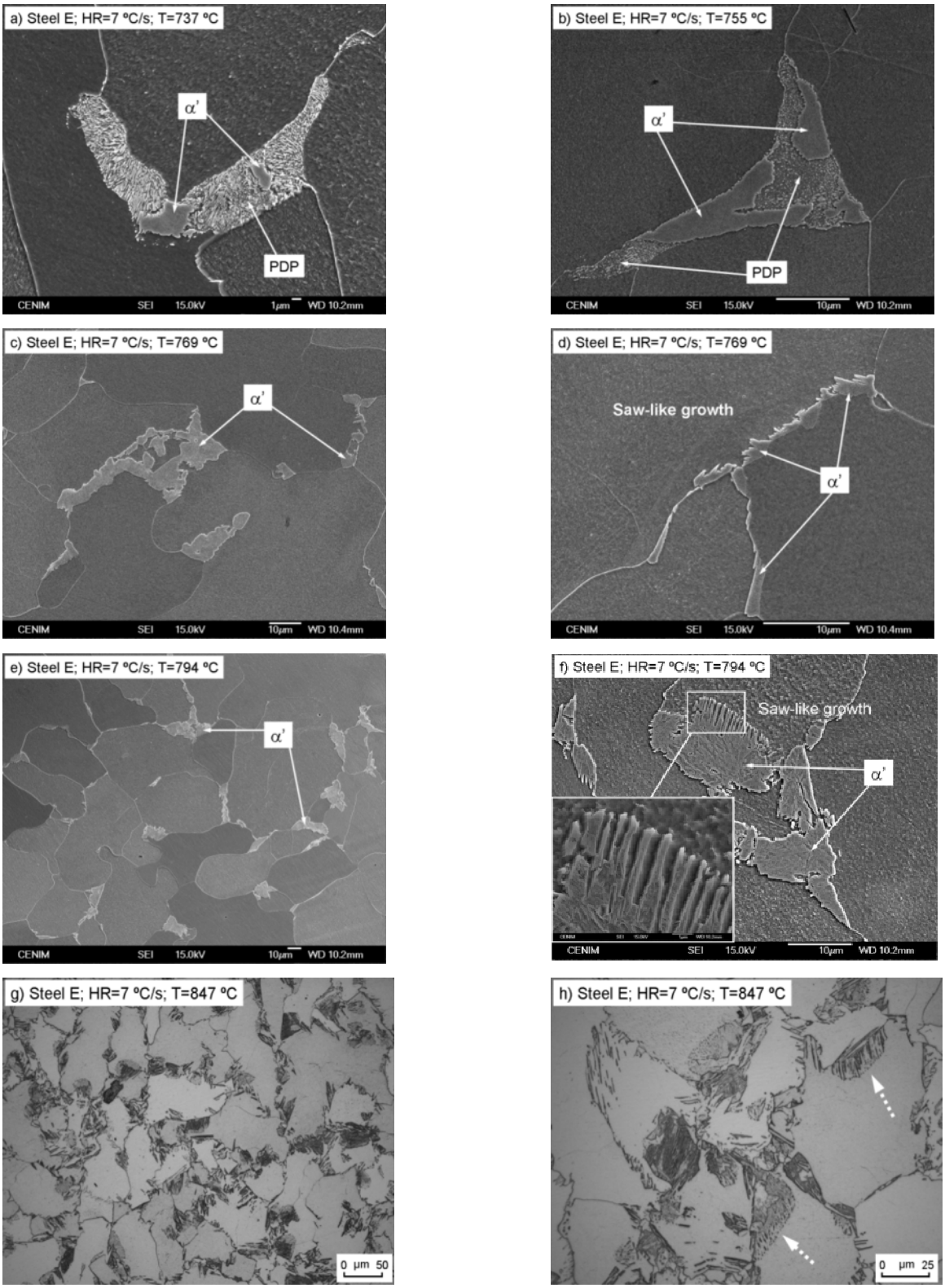

Figure 4.11 Scanning electron and light optical micrographs obtained in steel E after interrupted heating by quenching. Heating rate (HR) of 7 ºC/s to 737 ºC (a), 755 ºC (b), 769 ºC (c, d), 794 ºC (e, f), 847 ºC (g, h); Symbols α' and PDP stands for martensite and partially dissolved pearlite respectively.

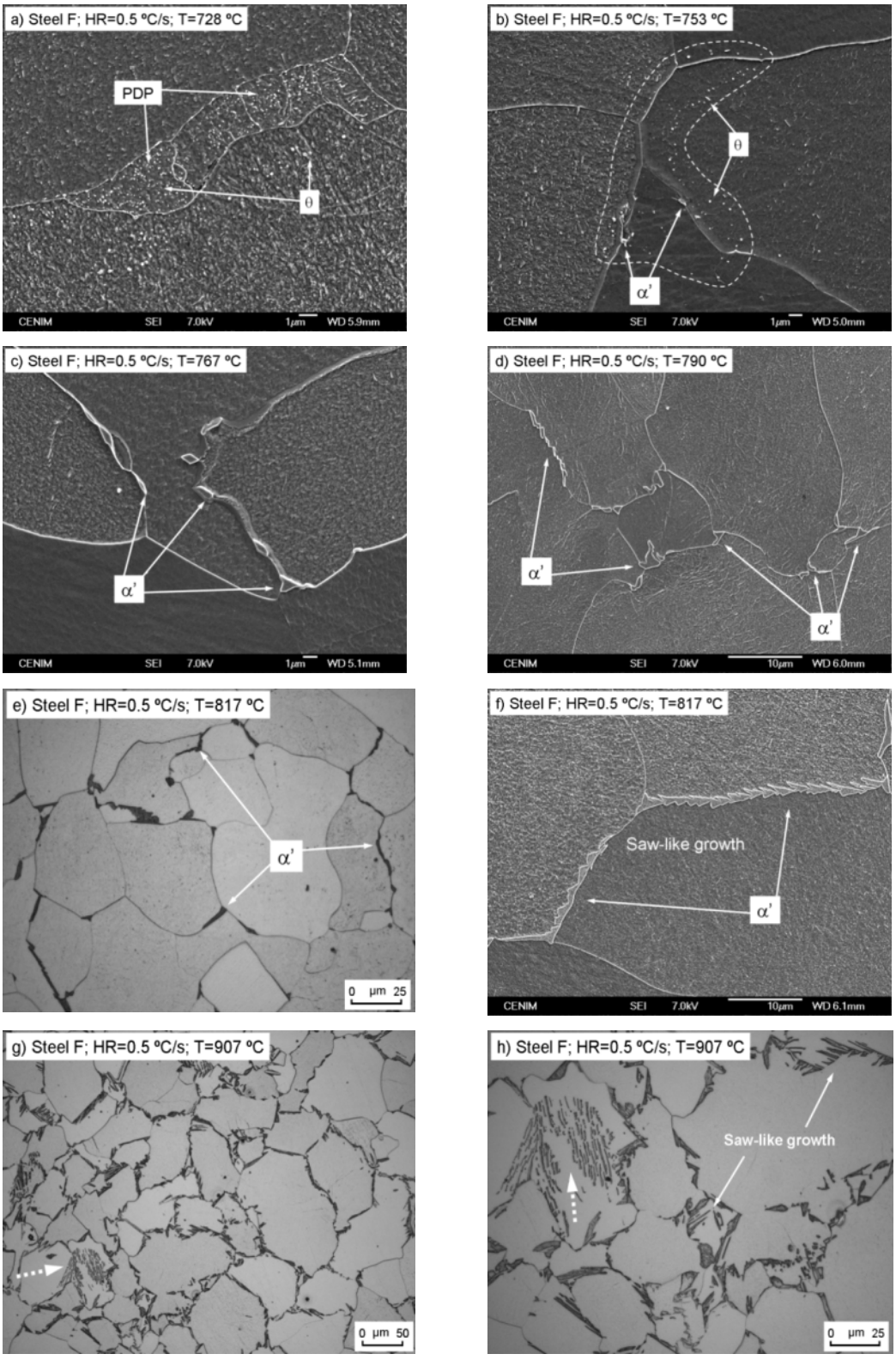

Figure 4.12 Scanning electron and light optical micrographs obtained in steel F after interrupted heating by quenching. Heating rate (HR) of 0.5 ºC/s to 728 ºC (a) 753 ºC (b), 767 ºC (c), 790 ºC (d), 817 ºC (e, f), 907 ºC (g, h). Symbols α' and PDP stands for martensite and partially dissolved pearlite respectively.

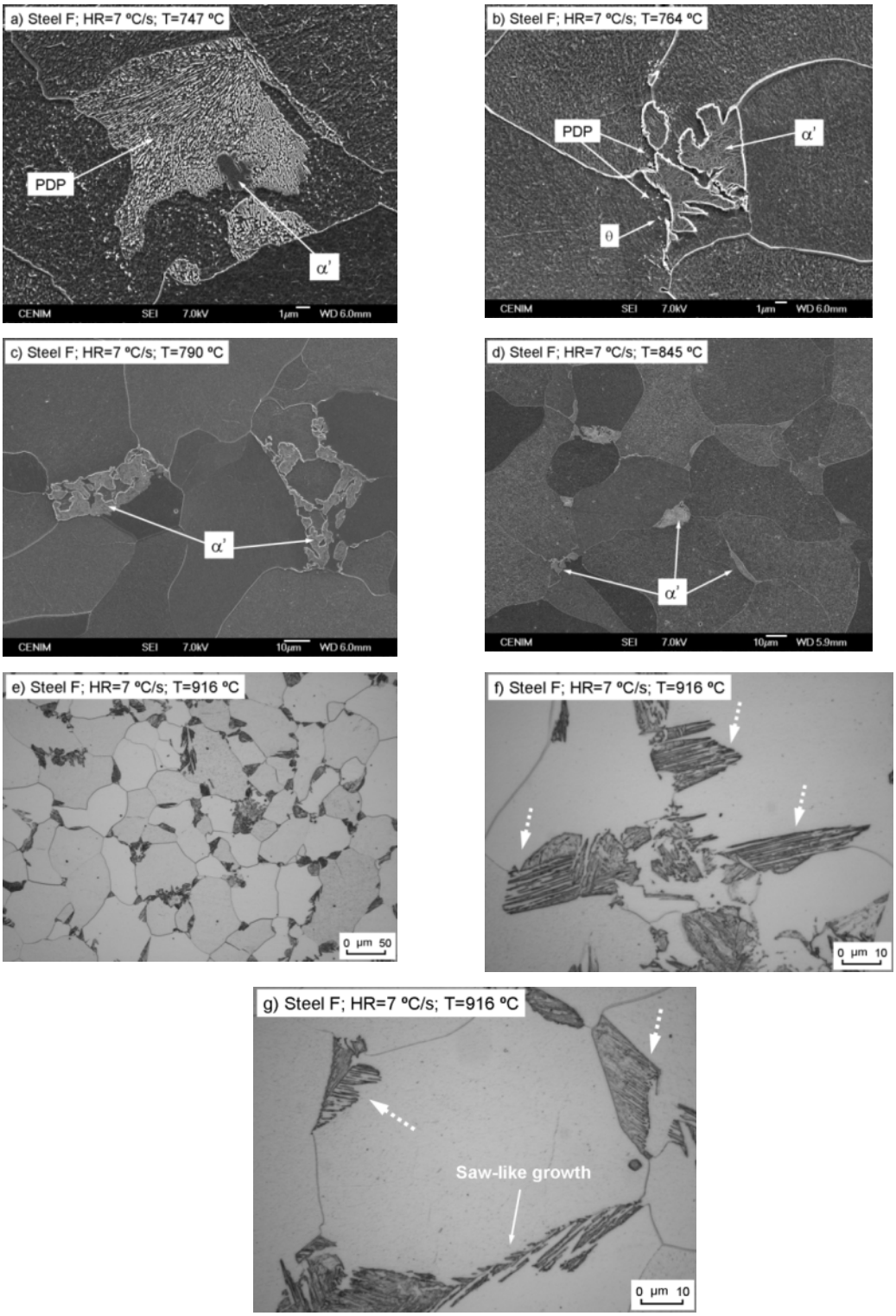

Figure 4.13 Scanning electron and light optical micrographs obtained in steel F after interrupted heating by quenching. Heating rate (HR) of 7 ºC/s to 747 ºC (a), 764 ºC (b), 790 ºC (c), 845 ºC (d), 916 ºC (e, f, g). Symbols α' and PDP stands for martensite and partially dissolved pearlite respectively.

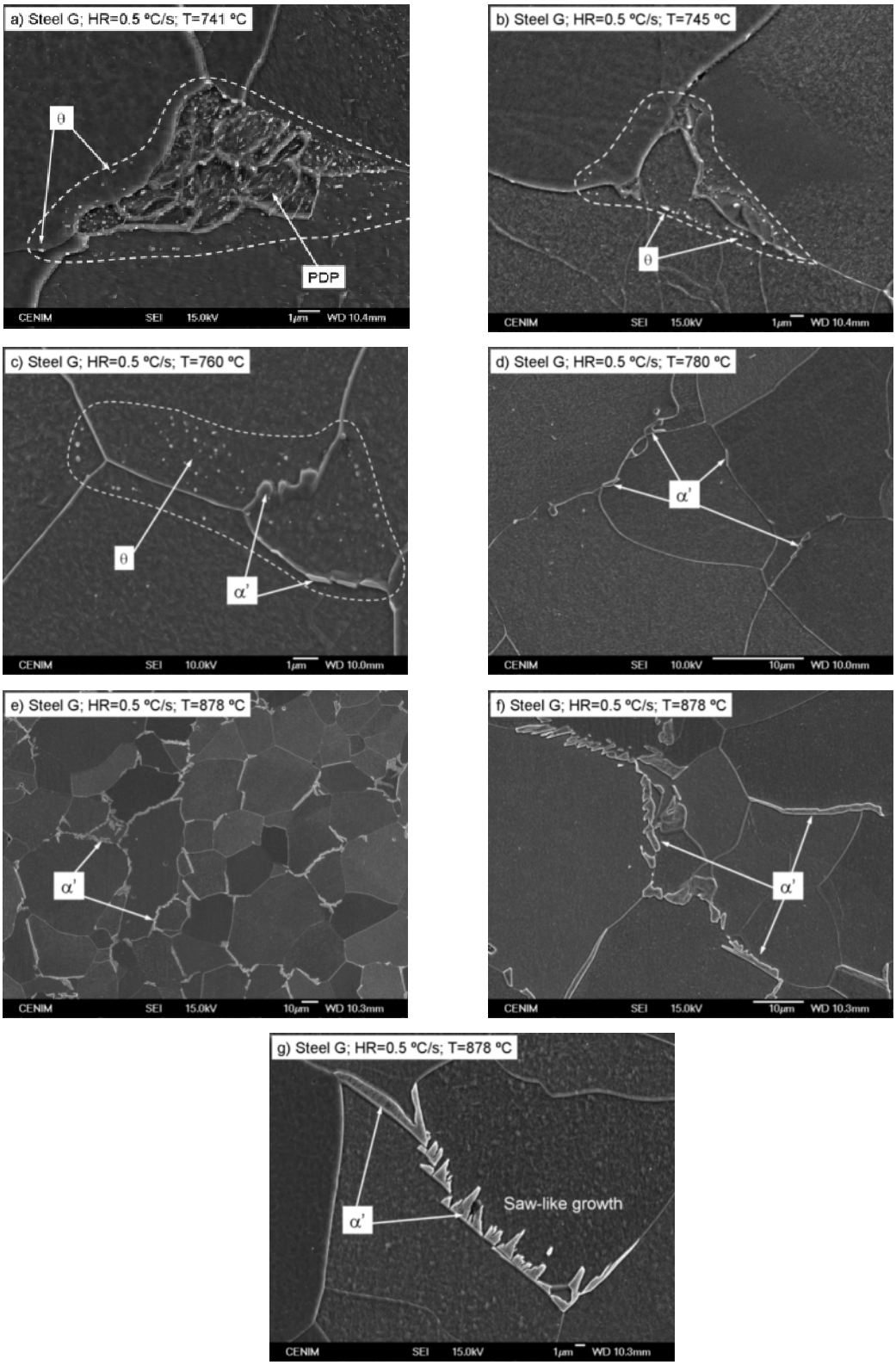

Figure 4.14 Scanning electron micrographs obtained in steel G after interrupted heating by quenching. Heating rate (HR) at 0.5 ºC/s to 741 ºC (a), 745 ºC (b), 760 ºC (c), 780 ºC (d), 878 ºC (e, f, g).Symbols α', θ and PDP stands for martensite, cementite and partially dissolved pearlite respectively.

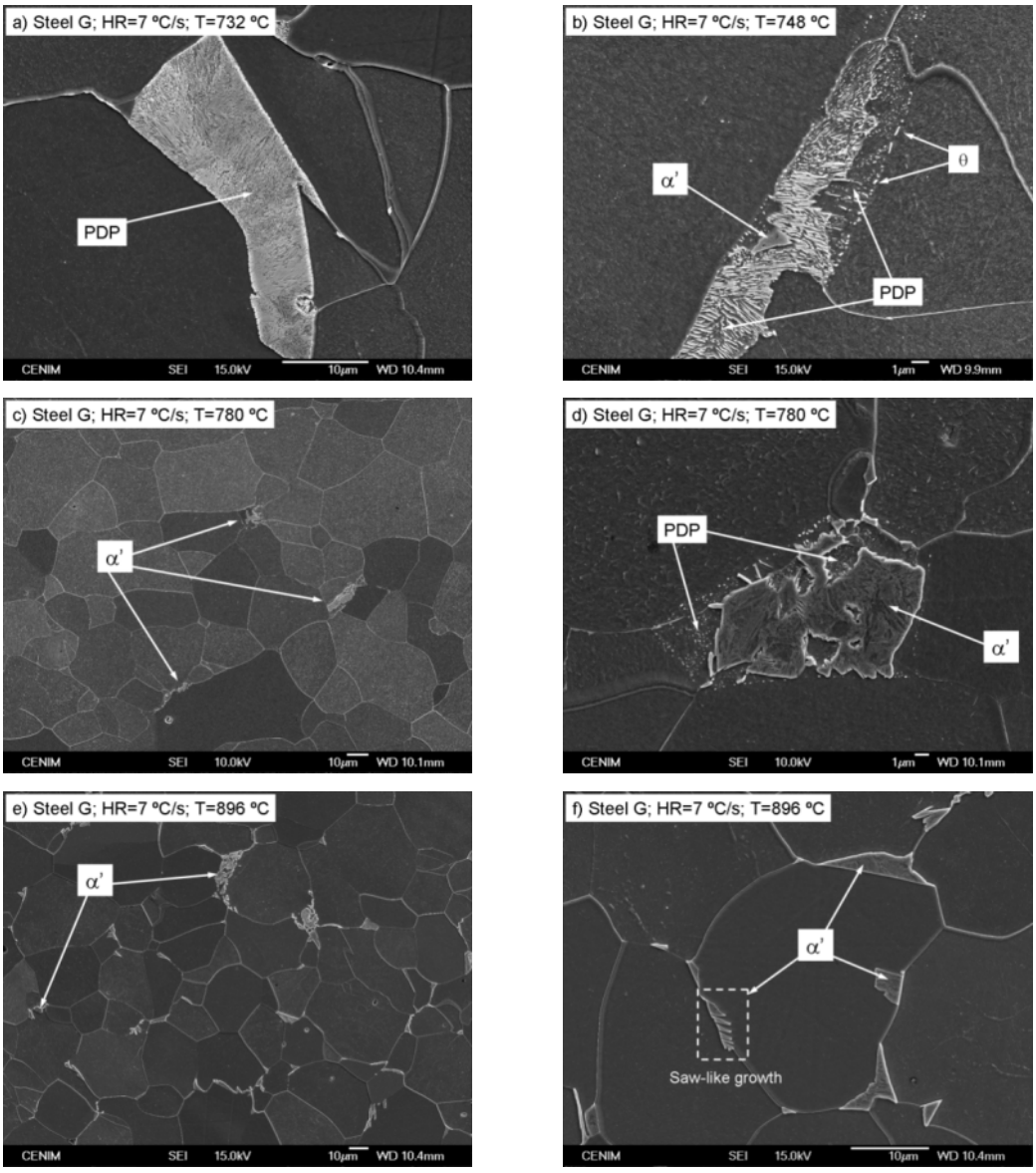

Figure 4.15 Scanning electron micrographs obtained in steel G after interrupted heating by quenching. Heating rate (HR) of 7 ºC/s to 732 ºC (a), 748 ºC (b), 780 ºC (c, d), 896 ºC (e, f). Symbols α', θ and PDP stands for martensite, cementite and partially dissolved pearlite respectively.

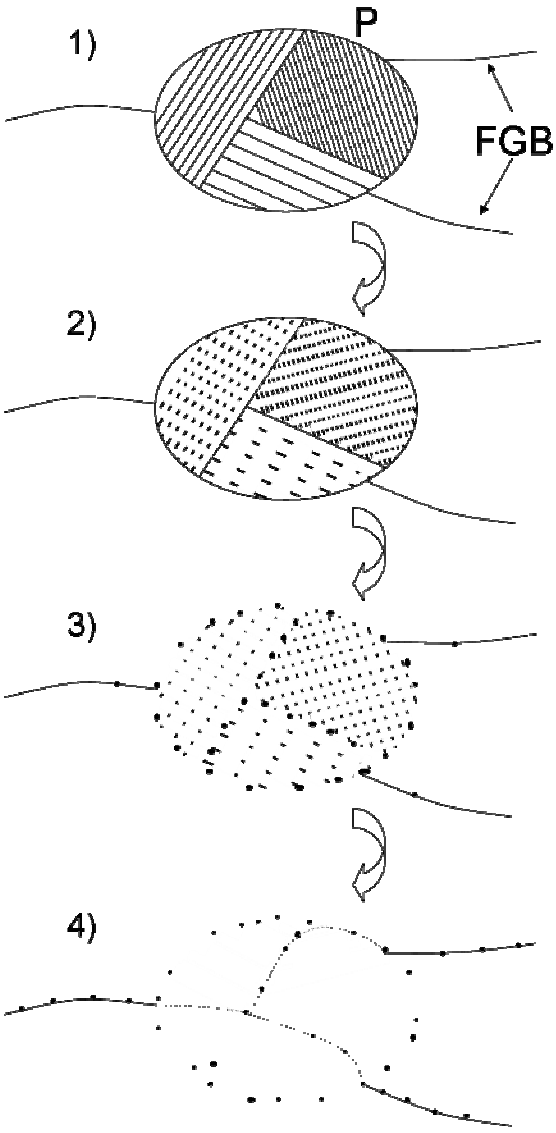

Figure 4.16 Representation of the dissolution/spheroidization of pearlite (P) during slow heating:

1) Initial pearlite nodule composed of three colonies;2) Start of the spheroidization process; 3) spheroidization/dissolution and precipitation at grain boundary colonies (see Figure 4.10a for example);4) Depending on the solubility of carbon in ferrite this process may end up in the complete dissolution of cementite lamellas; Only some cementite particles remain present at grain boundaries of pearlite colonies (see Figure 4.14b for example), start of nucleation at ferrite grain boundaries (FGB).

Figure 4.3a also shows that the solubility of carbon in ferrite reaches a maximum ($C^{\alpha}_{\max}$, Table 4.2) at temperature Ae_1 during heating and then falls. This carbon maximum is higher, with increasing aluminium content of the steel. This was expected due to the stabilizing effect of aluminium on the ferrite phase. Additionally, taking into account that the carbon content is slightly lower in the aluminium alloyed steels (F, G), these thermodynamic calculations explain why the extent of pearlite dissolution after heating at 0.5 ºC/s to a temperature around Ac_1 is more significant in steels F and G (see Fig. 4.12a-b and 4.14a-b, respectively) compared to steel E (see Fig. 10a). A quick calculation shows that, under equilibrium conditions, the carbon that remains undissolved in steel E at temperature Ae_1 ($C_N - C^{\alpha}_{\max}$, Table 4.2) is more than double the amount remaining in steels F and G. Finally, as expected for the three steel samples investigated, the lower the heating rate, the closer the system is to equilibrium heating conditions and more pronounced should be the extent of the dissolution of pearlite nodules. On the contrary, for high heating rates (>1 ºC/s) the heating time is much shorter, the dissolution effect is much weaker and the pearlite lamellar structure is kept almost intact at temperatures around Ac_1 (See Figs 4.11a, 4.13a and 4.15a-b for examples).

4.4.2 Austenite nucleation; pearlite to austenite transformation

It is expected that the state of pearlite dissolution/spheroidization should influence the nucleation and growth of austenite since the transformation starts at those locations where cementite is present. The distance between carbon sources also determines the kinetics of these transformations. In previous studies it has been experimentally observed that the smaller the interlamellar spacing of pearlite, which is the diffusion distance between carbon sources (cementite lamellas), the faster the kinetics of the pearlite to austenite transformation [92]. In spheroidized and partially dissolved pearlitic microstructures the volume fraction of cementite is lower and the diffusion distance between cementite particles larger, which should result in less nucleation sites for austenite and slower growth kinetics during the first stages of the

transformation. This effect is more pronounced when the microstructures of the three steels are compared.

As discussed before, the applied heating rate has a major influence on the stability of the lamellar structure of pearlite. The aluminium content of the steel also plays a role promoting the solubility of carbon in ferrite due to the higher solubility of this element in aluminium alloyed steels. At low heating rates the amount of cementite dissolved and/or spheroidized in steels F and G is much greater than in steel E. Thus, the initial microstructure of steels F and G just before the nucleation process is basically ferritic plus some cementite particles mainly present at ferrite grain boundaries; while in steel E pearlite has been just slightly dissolved and spheroidized, but keeping most of the structure intact. These microstructural differences result in a delay to the austenite nucleation process in the aluminium alloyed steels, which is in general translated as an increase in Ac_1 temperature (see values in Table 4.4). This delay in the nucleation process disappears under fast heating conditions (≥7 ºC/s), for which pearlite remains almost intact for the three steels investigated. Finally, it should be mentioned that the metallographic observations shown in Figs 4.10-4.15 confirm that the location of Ac_1, Ac_θ and Ac_3 estimated from the dilatometry plots is approximately correct within experimental error.

Since pearlite retains most of its initial structure during fast heating conditions, this results in having the growth of austenite after nucleation mainly confined to within former pearlite regions until cementite is totally transformed (for example, Fig. 4.11b, 4.13b-c, 4.15c-d). However, although in steel E the structure of pearlite is also kept intact for low heating rates (<1 ºC/s), growth along ferrite grain boundaries also takes place (Fig. 4.10b). The main reason for this latter observation could be explained if the nucleation is also taking place at cementite particles located at ferrite grain boundaries. Moreover, fast grain boundary diffusion of carbon would also assist the growth of austenite along these pathways for long heating times. On the contrary, heating conditions under which pearlite is almost entirely dissolved, as is the case for steels F and G for heating rates <1 ºC/s, nucleation takes place on cementite particles at ferrite grain boundaries (Fig. 4.12b-c, 4.14c-d) and grows following these pathways (Fig. 4.13d-f, 4.15e-g). This should be expected because after the dissolution of pearlite during heating, most cementite particles are present at ferrite

grain boundaries and carbon available for diffusion at these locations has increased. Moreover, due to a lower number of sites present for austenite nucleation (cementite), particularly in steels F and G, and because ferrite is more stable in these later steels (higher aluminium contents), it has been experimentally observed that the growth of austenite in the initial stages is slower.

4.4.3 Austenite growth; ferrite to austenite transformation

As the growth of ferrite to austenite is determined by how the nucleation and growth took place during the initial stages of cementite dissolution and transformation to austenite, austenite growth along ferrite grain boundaries compared to bulk growth will continue to be promoted the lower the heating rate and the higher the aluminium content of the steel under consideration. Once ferrite grain boundaries are saturated, the growth continues towards the bulk of ferrite grains.

As the amount of austenite transformed increases in the sample, the metallographic investigation of quench-out samples becomes more complicated. Figure 4.9 shows that even using high cooling rates (280-300 ºC/s) the formation of ferrite/bainite is detected. Note that ferrite/bainite formation is detected after austenitization to temperatures, $T_{\alpha+\gamma}$, far from Ac_3, which implies that still a small amount of austenite has transformed on heating. The expansion detected in the samples and the range of temperatures at which this takes place (between 500 and 950 ºC, depending on the steel composition) denotes that ferrite and, probably some upper bainite (depending on the temperature $T_{\alpha+\gamma}$), is forming from austenite during quenching. These results are partially explained if one realizes that as the volume fraction of austenite increases with heating temperature, the average carbon content decreases markedly (Fig. 4.3b). Moreover, under non-isothermal heating conditions compositional gradients of carbon inside austenite should be expected, so that regions of even lower carbon content might be encountered. This is observed for example in Fig. 4.11g-h. Nital-2% etching solution does not reveal all martensite regions in the same way; those regions with a lower amount of carbon are weakly revealed, highlighting the presence of adjacent regions of different carbon concentrations. It is well known that the lower the carbon content of martensite the more difficult to be quenched. One should also consider that hardenability decreases with the aluminium content. As a

result of the low carbon and/or high aluminium content of austenite, the formation of ferrite/bainite during cooling may be unavoidable even using very high cooling rates. Only during the initial stages of the transformation, when the carbon content is high enough, does austenite have sufficient hardenability not to transform to ferrite/bainite on cooling. Since discrimination between ferrite present in the initial microstructure and that formed on cooling becomes difficult using standard metallographic techniques, the study of these samples has been avoided. The quantification of austenite above a certain transformed volume fraction (~0.2-0.3) becomes unfeasible in these steel samples unless other in-situ high-temperature techniques such as X-ray or neutron diffraction are employed.

Nevertheless, some important observations can be made from the dilatometry results and the critical transformation temperatures derived from these plots:

1) For the same heating rate, the higher the aluminium content the slower the austenite growth which is reflected in an increase in temperature Ac_3 (Fig. 4.8);

2) In steel G (alloyed with 0.94 wt% Al), the lower the heating rate, the higher the temperature Ac_3. In steel F the same results are observed up to a heating rate of 7 ºC/s. This evolution of Ac_3 with heating rate is different to that observed in steel E and in other alloys free of aluminium [83].

Both observations are due to the stabilizing effect of aluminium when present in solid solution in ferrite. The ferrite to austenite transformation becomes less favourable thermodynamically (lower chemical driving; $\Delta G_{\alpha\rightarrow\gamma} = G_\gamma - G_\alpha$) the higher the aluminium content of ferrite; i.e. ferrite is more stable the higher the aluminium content. The first observation is due to the large difference in aluminium content between steels E, F and G. The second can be understood if it is assumed that during the transformation not only carbon would partition but aluminium would also diffuse from austenite to ferrite. To prove this hypothesis, a series of FIB/TEM experiments were designed and carried out. The obtained results will be discussed in next chapter in more detail. Figure 4.4 also shows that the aluminium content of ferrite under equilibrium conditions (very slow heating) increases with temperature

as we approach temperature Ae_3 (Ac_3 during heating). The enrichment of ferrite in aluminium would stabilize the remaining untransformed ferrite and increase temperature Ac_3 as the heating rates decreases. Partitioning of aluminium would clearly decrease for high heating rates far from equilibrium.

4.4.4 Austenite growth morphologies

If we assume that martensite retains the morphology of austenite upon quenching, different micrographs seem to reveal that austenite sometimes grows as finger or saw-shaped morphologies (See examples in Figs 4.10e,g; 4.11d,f,h; 4.12f,h; 4.13g; 4.14g; 4.15f). Saw-like morphologies are primarily observed growing from austenite nucleated at ferrite grain boundaries during slow heating conditions (Fig. 4.10g), while finger-like morphologies are observed growing mainly from regions where pearlite nodules located (Fig. 4.11f), but less commonly from former ferrite grain boundaries. Irregular microstructures have been also observed either during fast or slow heating conditions. These irregular microstructures seem to be due to the presence of etching contrast within this phase. A similar effect is observed between adjacent martensitic regions. This could be explained because Nital-2% etching solution enhances those regions with higher carbon content (see locations pointed by thick dashed arrows in different micrographs, like Figs 4.12h, 4.13f), suggesting that there exists an inhomogeneous distribution of carbon in the austenite during heating. Some of these morphologies resemble those observed in bainite and Widmanstätten ferrite microstructures. These types of microstructures have been observed before in different types of steels but the mechanism of formation is yet unclear [84, 90, 93, 94]. Electron probe microanalysis (EPMA) measurements carried out by Savran et al. [93] in microstructures similar to Fig. 11f (finger-like), show that between fingers, the carbon concentration is much lower (~0.2 wt%) than that of the fingers themselves (0.8 wt%); however, it is too high to suggest that these spaces between fingers correspond to the ferrite phase. These results would suggest that the distribution of carbon in austenite in the growth front is again very inhomogeneous in some cases. Savran et al. argued that in this finger-type of austenite growth fronts occur only when the austenitic microstructure inherits the former pearlitic lamellar structure and this only happens when cementite lamellas are perpendicular to the

front of growth. Following this argument, finger-like growth would be visible just after pearlite has transformed and would disappear as the transformation goes on. However, in the steel samples under investigation, these morphologies have been observed long after pearlite dissolution has taken place. On the other hand, growth morphologies like the one observed in Fig. 10g could not be explained in this way. Zel'dovich et al [94] related the formation of the saw-like microstructures to the partitioning of nickel in high nickel alloyed steels during slow heating (0.05 ºC/s) and did not observe this morphology during fast heating when partitioning did not occur. In these steels it could be the result of aluminium and/or manganese partitioning. A major investigation of the distribution of alloying elements as well as on the local orientation relationships between phases would be needed to understand why this growth mechanism is more efficient than a planar growth front under certain conditions.

4.5 Conclusion

The present investigation deals with the influence of aluminium and heating rate on the formation of austenite during continuous heating in low carbon (0.02 wt%) manganese (1.4 wt%) alloyed steels. The main conclusions are highlighted as follows:
- The temperatures that determine the start (Ac_1) and finish (Ac_3) of the austenite formation process have been experimentally determined using high resolution dilatometry over a wide range of heating rate conditions (0.05, 0.5, 1, 7, 20 ºC/s). Temperature Ac_θ that defines the end of pearlite to austenite transformation has also been estimated but only for steel E. It has been observed that while temperature Ac_1 remains almost unaffected, temperature Ac_3 increases markedly with the aluminium content of the steel.

- It has been shown experimentally that slow heating conditions promote the spheroidization and dissolution of pearlite phase before reaching temperature Ac_1. In the extreme case, after the dissolution process, only a few cementite particles are visible in the initial ferritic matrix located at ferrite grain boundaries. This effect is more pronounced the lower the heating rate, the lower the carbon and the higher the aluminium content of the steel.

- The dissolution of pearlite results in a decrease in the number of nucleation sites for austenite (cemenite), delaying the nucleation of this phase in the aluminium alloyed steels and thus increasing temperature Ac_1. This delay in the nucleation process reduces as the heating rate applied is increased. However, even at high heating rates, and due to the smaller number of carbon sources available after the partial dissolution of pearlite, the growth of austenite becomes slower in these microstructures during the initial stages of the transformation. Moreover, under these conditions, austenite growth occurs mainly along ferrite grain boundaries as carbon sources (cementite) are present at these locations. Only after the saturation of grain boundaries has taken place growth towards the bulk of ferrite grains occurs. For high heating rates at which pearlite remains almost undissolved during heating to Ac_1, austenite growth is basically confined to pearlite regions.

- In the aluminium alloyed steels the slower the heating rate, the higher the temperature Ac_3. This is explained by the partitioning of the aluminium to the untransformed ferrite phase during heating.

- The metallographic study of the austenitic microstructure, generally undertaken in quenched samples, in which it is assumed that the martensitic microstructure resembles that of austenite at high temperatures, becomes very difficult in the steels under investigation. Due to the low carbon and high aluminium content of the steels, the hardenability of austenite becomes very low and the formation of ferrite/bainite during quenching even at rates as high as 300 ºC/s becomes unavoidable. As a result, only the evolution of austenite up to volume fractions 0.2-0.3 could be investigated metallographically.

- It was shown that heating rate has a strong influence on Ac_3, which possibly is due to the partitioning of Al, and this should be taken in to account in designing further experiments.

Chapter 5: Partitioning of Al in ferrite – austenite region with low heating rates

Introduction

As mentioned in chapter 4, there is little literature concerned with the effect of Al in solid solution on the austenetization process. Therefore, more systematic research on the effect of Al in solid solution is required to understand the influence of Al on steel microstructure. It was shown in chapter 4 that additional Al delays the austenite formation. Moreover, the critical transformation temperatures in the steels investigated are very sensitive to the applied heating rates. It was shown that in steel G (alloyed with 0.94 wt% Al), the lower the heating rate, the higher the temperature Ac_3. The same result can be observed up to a heating rate of 7 ºC/s in steel F. This change of Ac_3 with heating rate is different to that observed in steel E and other steels with low level of aluminium [83]. The reverse effect would have been expected i.e. a faster heating rate should have led to a higher A_{c3} since the faster the heating rate the further the steel is from equilibrium conditions. The most likely interpretation for the observed results is the diffusion or partitioning of Al to the final remaining ferrite grains at temperatures close to Ac_3

To prove and confirm this hypothesis experimentally a series of FIB/TEM experiments were designed and conducted based on steel F. More details regarding the effect of heating rate on Ae_3 in Al added steels can be found in chapter 4 however Table 5.1 gives a brief summary of the two applied heating rates and the obtained Ac_3.

Table 5.1 Influence of heating rate on temperature A_{c3} for steels E (0.02 wt%Al) and F (0.48 wt%Al)

	Heating rate	
	0.05 ºC/s	7 ºC/s
Steel E: A_{c3}	913±4 ºC	904±5 ºC
Steel F: A_{c3}	1025±3 ºC	987±2 ºC

5.1 Results and discussion

Table 5.1 displays the Ac_3 temperature determined from the dilatometry plots, for the two different heating conditions. As mentioned, the addition of 0.48 wt% Al increases Ac_3 from ~910 to 985-1025ºC. This is consistent with Al acting as a ferrite stabilizer and expanding the ferrite + austenite phase field. In addition, it was shown that the Al-alloyed steel (F) has an Ac_3 that is very sensitive to the applied heating rate, while steel E does not. For steel F, the Ac_3 increases (from 987 to 1026 ºC) with a decreasing heating rate. Previous work on the effect of heating rate on this critical transformation temperature in low and medium steels without Al shows the opposite, a faster heating rate led to a higher Ac_3 since the faster the heating rate the further the steel is from equilibrium conditions . It was mentioned that the most likely interpretation for the results observed here is the diffusion or partitioning of Al to the untransformed ferrite grains which then further delays their transformation to higher temperatures. If this is so then at temperatures close to Ac_3 a greater concentration of Al is expected in the last untransformed ferrite grains of an Al-rich steel (such as steel F here), and that this would be most prominent at a low heating rate (such as 0.05 °C/s) since this would allow the Al time to diffuse and partition. Thus we have investigated Al levels (by EDX) in an untransformed ferrite grain and a former austenite grain of a partially transformed TEM specimen of steel F (details in the following paragraph). Certainly it is well known that during an austenitization heat treatment, partitioning of alloying elements can take place, that the extent of this is dependent on the relative solubilities in austenite and ferrite [95, 96] and that his phenomenon can affect the transformation kinetics in steel [97]. It is well documented that during annealing in the ferrite-austentite phase region, Mn partitioning can take place. However, there is little literature concerned with the partitioning of Al during the austenitization process. Koo et. al. [98] have shown that Al may partition under certain heat treating conditions and intercritical annealing (ferrite/austenite region) in steels alloyed with 1 wt% Al, while Amirthalingam et.al. [99] have shown higher concentrations of Al in ferrite grains in welded, high silicon and high aluminium TRIP steels.

To study the austenite/ferrite interface in the Al added steel (F), a specimen (2 cm cube) was heated continuously at 0.05 °C/s up to 970 °C and water quenched to room

temperature. Standard metallographic procedures were carried out to reveal the microstructure. Due to the sample's microstructure and grain size (Fig. 5.1A), the chance of obtaining a TEM thin foil sample containing an appropriate untransformed ferrite and former austentite boundary, with the 'bulk' electropolishing technique, was considered small and therefore, the site-specific focused ion beam (FIB) preparation technique was utilized. A TEM thin foil (thickness ~60 nm) containing a specific austenite/ferrite interface (Fig. 5.1b) was prepared using a FEI NOVA200 dual beam FIB/SEM. An FEI CM200 TEM operating at 197 keV fitted with a Gatan imaging filter and an Oxford Instruments energy dispersive X-ray (EDX) spectrometer was used to examine the FIB section. To determine the concentration of Al on both sides of the interface, the ultra thin window (EDX) spectrometer was employed (running OxfordInstruments ISIS software); EDX spectra were taken in TEM mode with a spot size of ~6 nm diameter (it is estimated that this increases to 10 nm after beam broadening) and were quantified using the ISIS software (including an appropriate correction for X-ray absorption).

The heat treated steel contains a mixture of very large ferrite grains (approximately 10 % of the bulk) and relatively fine ferrite grains (approximately 90 % of the bulk; Fig. 5.1a and 5.1b). Due to the low carbon and high Al content of the steel, the hardenability of austenite at temperatures close to Ac_3 is extremely low, resulting in the unavoidable formation of ferrite, even at cooling rates greater than 300 ºC/s (confirmed through dilatometry experiments). Consequently for this water-quenched specimen the fine grained ferrite is presumed to be formed on quenching from austenite grains formed at temperature and the large ferrite is consistent with the expected volume fraction of ferrite and austenite at 970 °C (based on the dilatometry data). It is assumed that the interface between a coarse and a fine ferrite grain represents approximately the interface between an untransformed ferrite and austenite grain at high temperatures and that the rapid quench has prevented any subsequent Al re-diffusion. These assumptions therefore suggest that the rhomboidal indentation shown in Fig. 5.1b is located at the interface between an untransformed ferritic region (grain A in Figs 5.1 (b-d) and 5.2 (a, b)) and a transformed, former austenitic region containing finer grains (grain B). A thin foil of this identified boundary region was prepared for TEM by dual beam FIB (Fig. 5.1c). Extreme care was taken to make the FIB section as thin as possible for TEM imaging at high

resolution without causing significant surface damage and ion implantation. In addition, the relative orientation of the FIB section was carefully noted so as to preserve the distinction between the untransformed ferrite (grain A) and the former austenitic (grain B) region. Electron diffraction was used to confirm the phase purity (ferritic nature) of the two grains in the FIB section (Fig. 5.1d). Atomic lattice imaging of the section revealed a sharp grain boundary interface (Fig. 5.2b). The spatial distribution of Al and Mn respectively across the interface was determined by spot EDX (Fig. 5.3 a-b). These results show considerable variations in the concentrations of both Al and also Mn within the two adjacent grains A and B. This could be either due to the fact that the Al and Mn distribution is not homogenous within even one phase (ferrite) or following the assumptions above that we are examining at temperature transformation interface. If the latter then the concentration of Al is significantly higher in the untransformed ferrite (grain A, mean 0.94 wt%) than the former austenite (grain B; mean 0.53 wt%). Such distribution would be expected if partitioning/diffusion of Al into the ferrite phase is taking place at high temperature. However, it is expected to see a fall in aluminium concentration profile in both sides of the interface by going away from the interface i.e. inside B the aluminium concentration approaches ~ 0.48 wt%, which is the bulk level and inside A aluminium concentration reaches ~ 0.7 wt%, which is the equilibrium level of Al according to MTData calculation [69]. The corresponding concentration profile for Mn is the inverse of that observed for Al (i.e. it increases from grain A to B) as in contrast to Al, Mn is an austenite stabilizer and partitions in the opposite direction (i.e. to austenite). EDX elemental analysis was also performed across what is presumed to be a former austenite/austenite interface (in a region indicated with an arrow in Fig. 5.1a) and Fig. 5.3c shows the areal concentration profile of Al across this interface. As expected, the results do not show any significant difference in the level of Al between two former austenite grains and the Al concentration is similar to the base composition of the steel.

In summary, this investigation involving TEM-EDX analysis of untransformed ferrite and former austenite interfaces in site-specific cross-sections prepared by FIB, has supported the hypothesis that the increase in Ac_3 temperature in the Al alloyed steel during slow (0.05 ºC/s) heating as compared with fast (7 ºC/s) heating conditions is due to the partitioning of Al atoms from austenite to the untransformed

ferrite, so further stabilizing this phase. In addition, the results show that partitioning of Mn takes place between austenite and ferrite during slow heating which is consistent with previous studies and expected because Mn is a known austenite stabilizer.

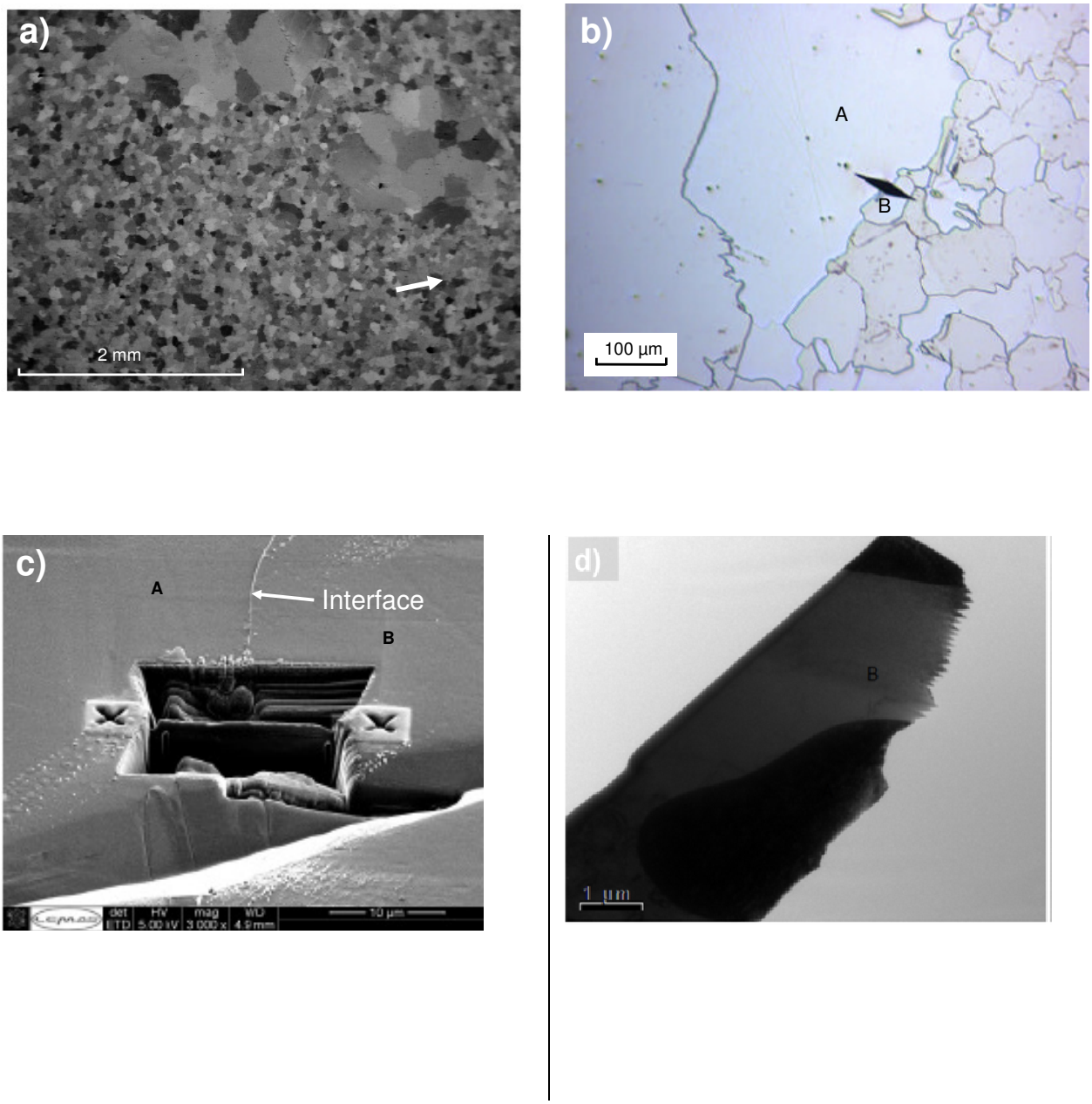

Figure 5.1 Micrographs of the microstructure of Steel B: a) Back scattered electron image; b) optical metallography image of interface between the a ferritic region and a former austenitic region; c) the selected area for FIB sectioning where TEM-EDS analysis will be performed
d) FIB section observed by TEM

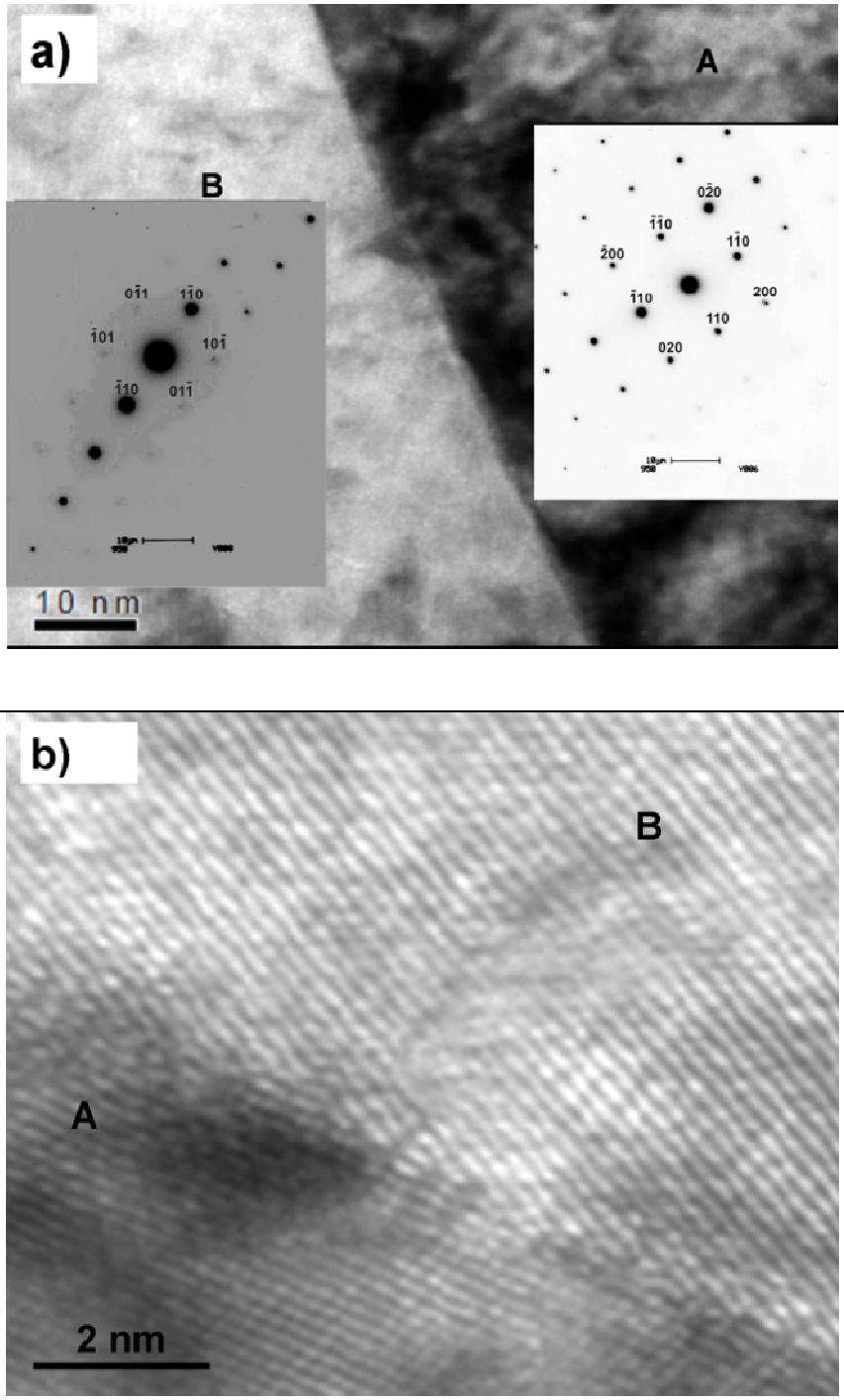

Figure 5.2 (a)TEM images of the FIB section in steel B showing the interface between two different grains and diffraction patterns from both side of interface (b) high resolution image form interface showing lattice image

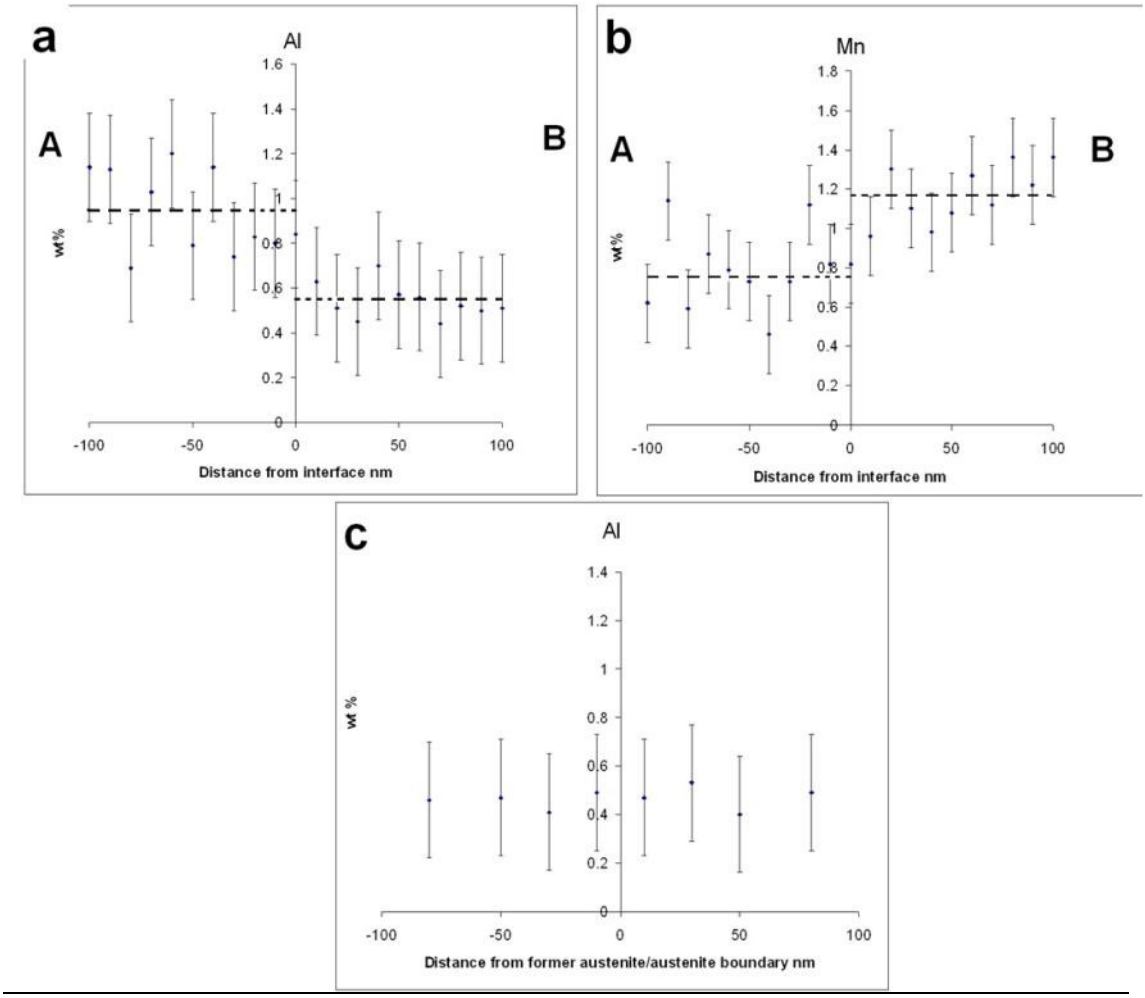

Figure 5.3 Elemental concentrations (EDX) of Al (a) and Mn (b) across the austenite/ferrite interface and Al (c) across a former austenite/austenite interface

Chapter 6: The effect of additional Al on prior austenite grain size

Introduction

The austenite formation process in the investigated steels and the effect of additional Al have been studied extensively in last two chapters. It has been shown that additional Al affects the austenite formation kinetics and depending on the applied heating rate the critical transformation temperatures i.e. A_1 and A_3 are influenced by the amount of Al in each steel. However, the role of additional Al in affecting austenite grain size has not been investigated yet. In the present chapter, efforts will be made to reveal the role of Al in solid solution on the determination of austenite grain size and the results obtained from this chapter in addition to the last two chapters will be considered in the design of the isothermal experiments in the following chapter.

Austenite grain growth is a thermally activated process which depends on both time and temperature. However, there are some other well know phenomena such as solute drag or the presence of second phase particles which can influence the grain growth process [19, 100]. It is well documented that the final structure and consequently the mechanical properties of steel is highly dependent on prior austenite grain size. Thus, producing a desirable austenite grain size is one of the key factors in improving the steel's properties.

It has been shown that austenite grain coarsening can proceed in one of two ways, depending on the composition of the steel. In plain carbon steels, in the absence of any nitride forming elements such as Al, V, and Ti, the growth regime can be described as a gradual growth of all grains as the temperature is increased [101]. A second type of growth takes place in steels containing additions of grain refining elements such as Al and V. In this type, austenite grain size would not change significantly until the temperature reaches a certain point which is called the grain coarsening temperature. This is closely related to the size and volume fraction of precipitated particles. Above this point only a few grains grow and the structure would be the mixture of fine and coarse grains. However, when the temperature increases significantly all grains become coarse [19, 102].

It is well documented that Al in amounts 0.02-0.07 wt% is a strong grain refining element. It can form AlN which consequently inhibits grain growth and produces fine structure in the steel. Nevertheless, as with other aspects of solute Al in steel, there is little detailed literature concerning the effect of aluminium in amounts higher than 0.1 wt% on steel microstructure concerning the influence of Al (apart from AlN) on austenite grain size and austenite grain growth.

6.1 Experimental

To investigate the effect of Al additions on prior austenite grain size, cylindrical samples 5 mm in diameter and 12 mm in length were made and a 2 mm wide surface was generated along the longitudinal axis of the samples by polishing and finishing with 1 mm diamond paste. Subsequently, these samples were heated in the furnace of a Bahr D805 high resolution dilatometer at a rate of 14 ºC/s to 650 ºC and then 6.6 ºC/s to 900 ºC, followed by 2 ºC/s to different austenetising temperatures; samples were then held at their respective austenetising temperatures for 600 sec before being subsequently cooled to room temperature at a rate of 1 ºC/s. The preceding heat treatments produce a thermal etching of the steel revealing the prior austenite grain boundaries. To measure the prior austenite grain size (PAGS) and grain size distribution the following procedure was conducted: a binary colour image was drawn manually from optical micrographs obtained using reflected light microscopy with grain boundaries in white and background in black; the area of every grain (A) was determined by using an image analyser and the Feret diameter was determined for each grain. The Feret diameter (d) is the diameter of a circle having the same area as the grain ($d = \sqrt{4A/\pi}$). Approximately 500 grains were measured to decrease the error of the measurement to 5%.

6.2 Results

Figures 6.1-6.3 show the optical micrographs of the thermal etched samples of steels E, F and G treated at different austenetising temperatures. It is clear that the thermal etching technique appears to be more effective in revealing the prior austenite grain

boundaries in higher Al steels, specifically in steel G, regardless of the austenetising temperature. Figure 6.4 illustrates the variation of austenite grain size with austenetising temperature for the three steel. The results do not show any significant difference in prior austenite grain size (PAGS) at temperatures below 1050 ºC, whereas a significant difference is observed at higher temperatures. For instance, the measured PAGS for steels E, F and G at 1050 ºC shows approximately the same value of 47 µm, while for steel E at 1200 ºC the PAGS jumps to 400µm and for steel F the value is 150 µm. However, for steel G the PAGS remains relatively unchanged between different austenitising temperatures. In addition to the grain size, all three investigated steel samples show the sudden grain growth regime yet the slope and also the sudden growth temperatures varies with steel compositions.

Figure 6.5 shows the MTData [69] thermodynamics calculation for the presence of AlN in the investigated steels. Although it shows a slight difference in mass fraction of AlN in the investigated steels which is due to the small difference in nitrogen content, this appears as a negligible difference which can be ignored i.e. it can be assumed that the mass fraction of AlN among these three steels is the same.

Figures 6.6-6.8 show the grain size distribution at different austenetising temperatures in the three investigated steels (E, F, and G). A significant difference is seen not only in mean grain size but also in grain size distribution at different austenetising temperatures.

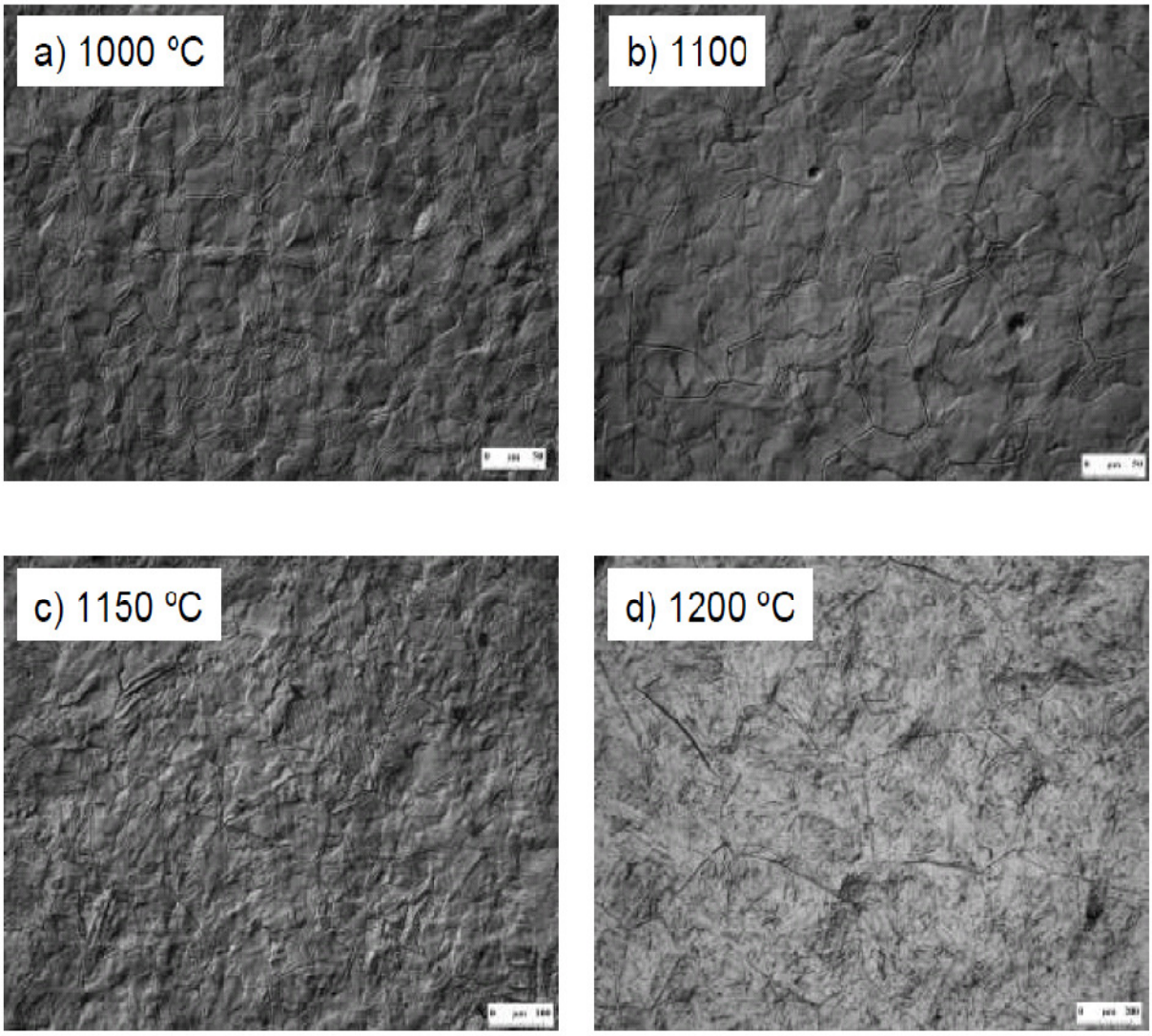

Figure 6.1 Optical micrographs showing the prior austenite grains for steel E at different austenetising temperatures

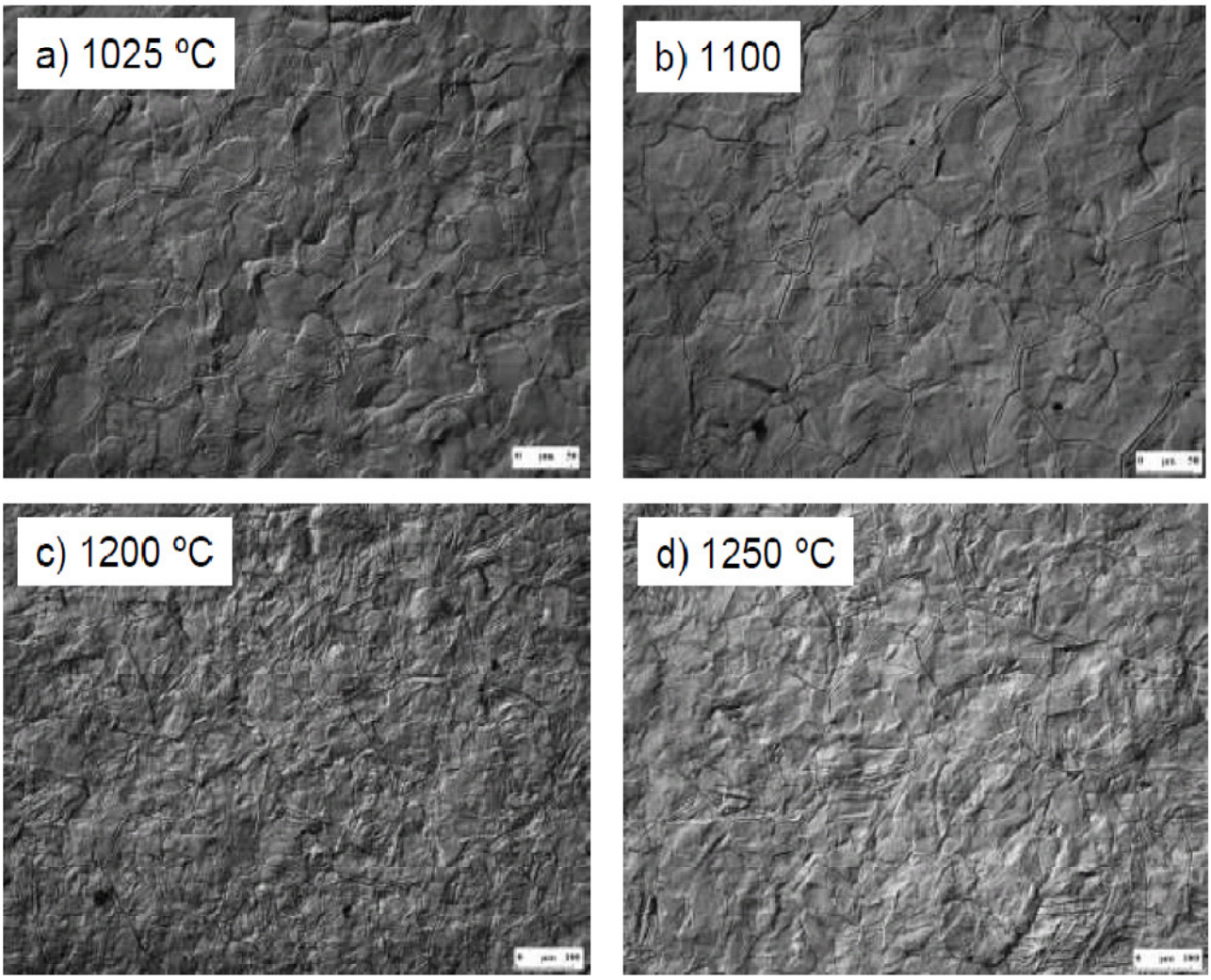

Figure 6.2 Optical micrographs showing the prior austenite grains for steel F at different austenetising temperatures

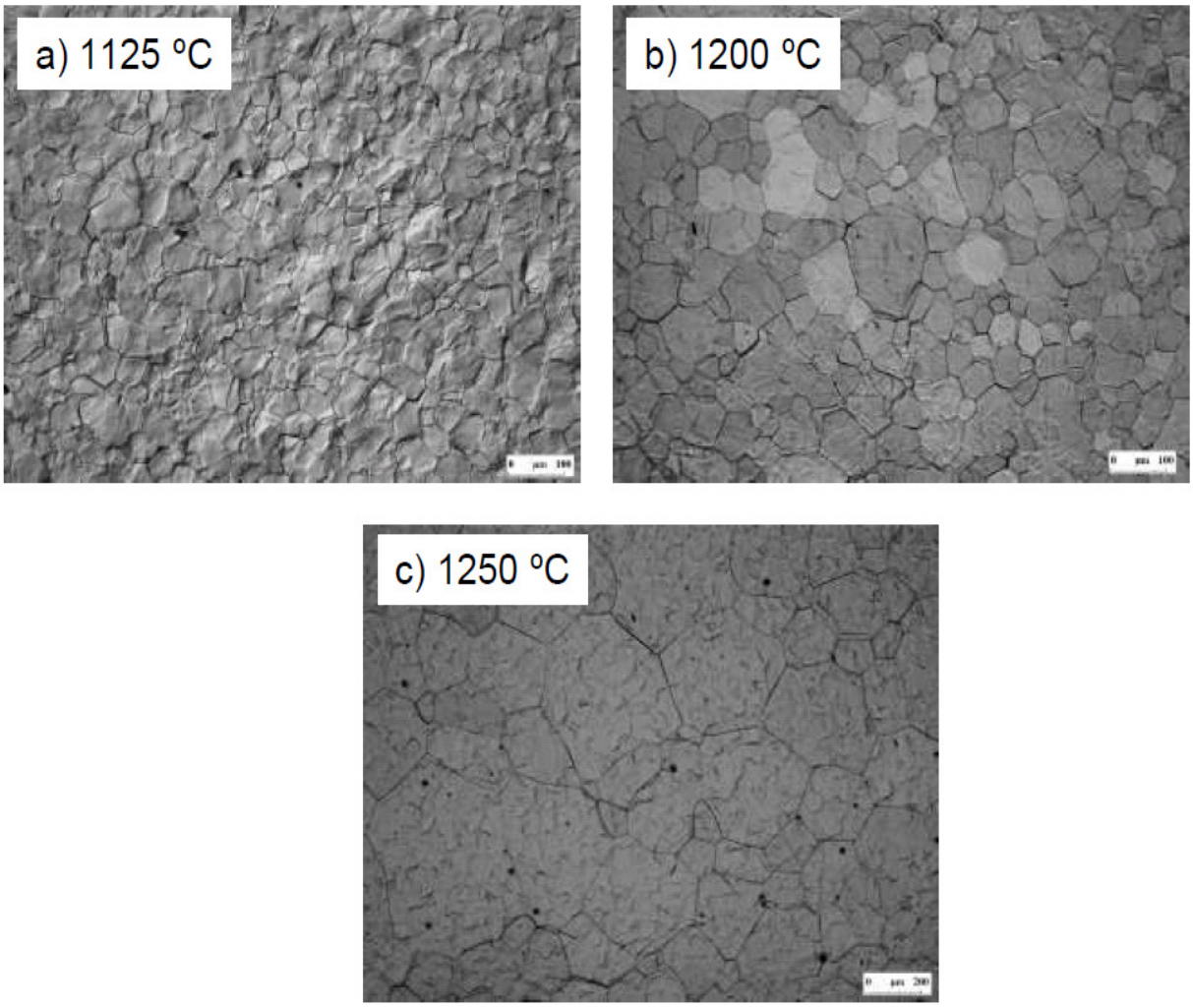

Figure 6.3 Optical micrographs showing the prior austenite grains for steel G at different austenetising temperatures

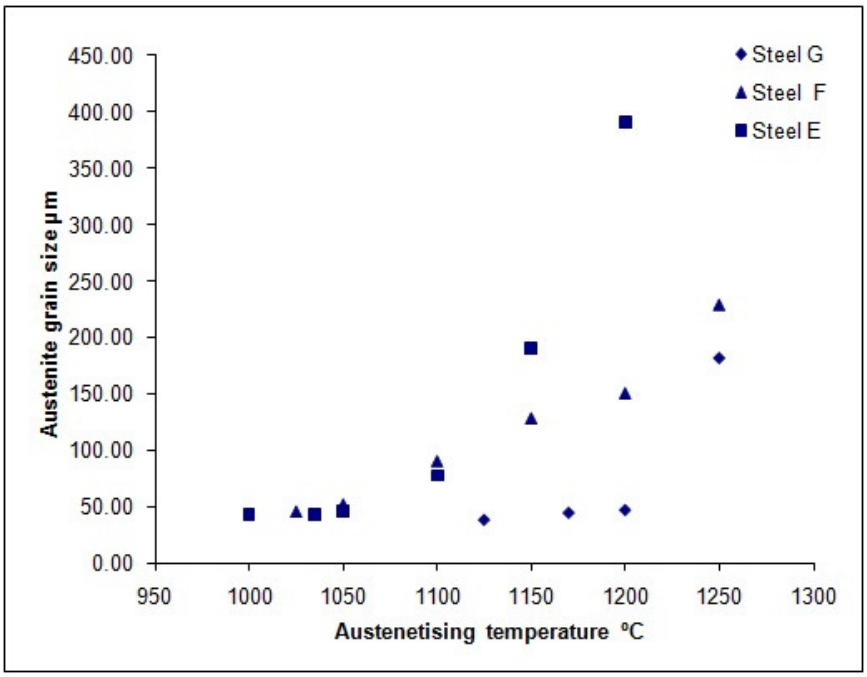

Figure 6.4 The effect of different austenetising temperature on austenite grain size in the investigated steels

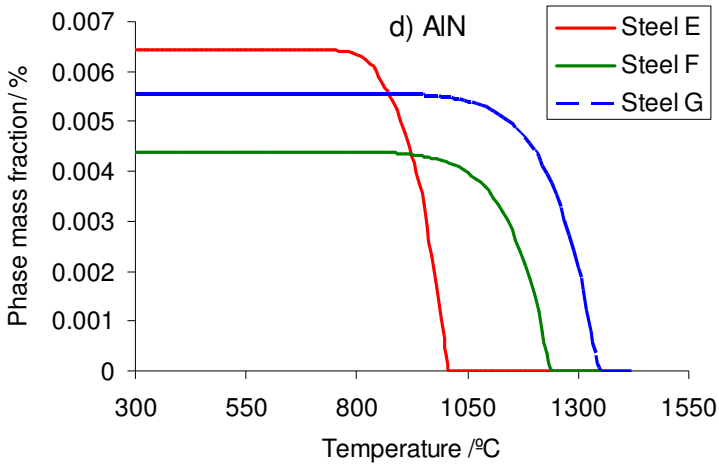

Figure 6.5 MTData calculation for presence of AlN in the investigated steels

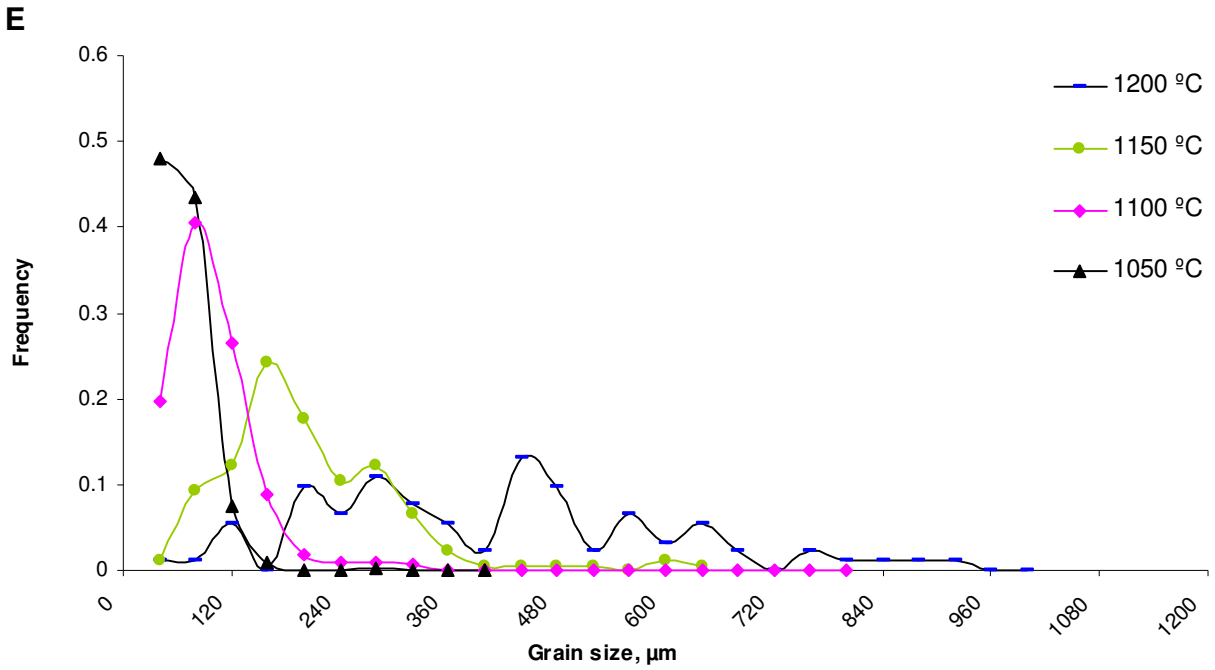

Figure 6.6 Prior austenite grain size distribution in steel E at different temperatures

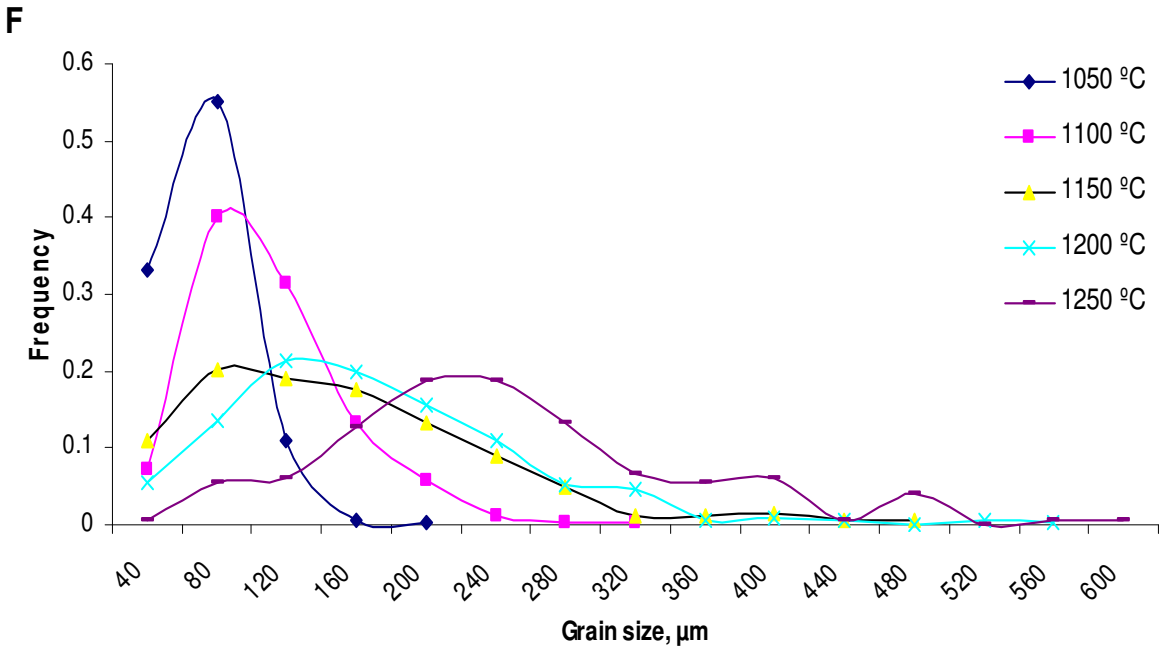

Figure 6.7 Prior austenite grain size distribution in steel F at different temperatures

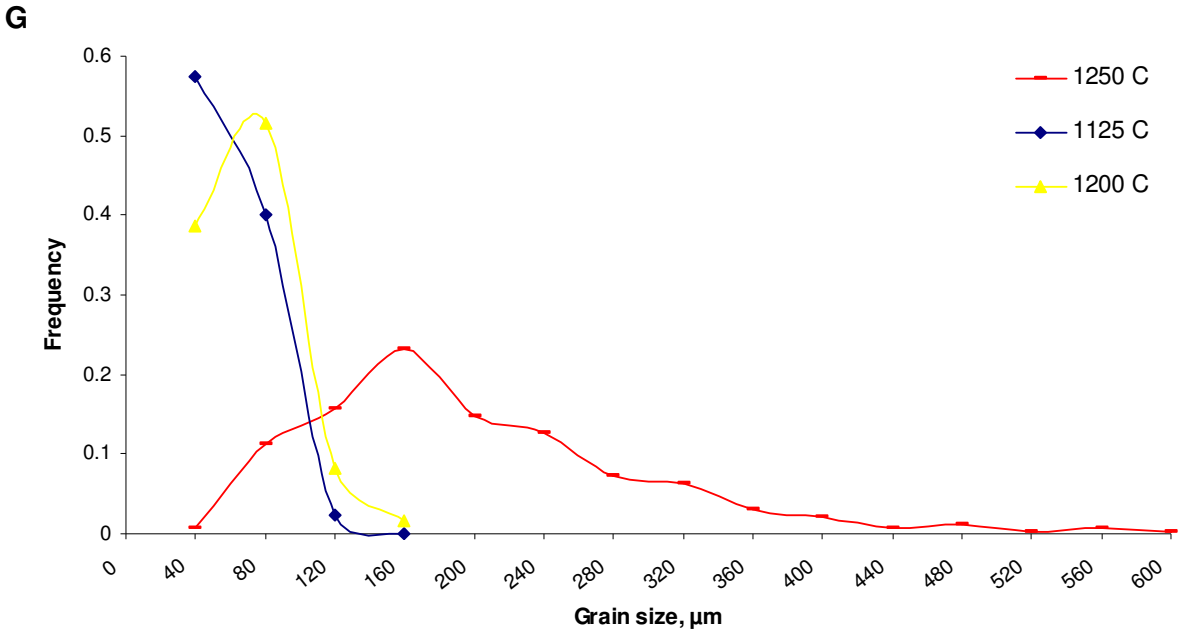

Fig 6.8 Prior austenite grain size distribution in steel G at different temperatures

6.3 Discussion

For steel E, Fig. 6.4 shows the typical behaviour of grain growth, commonly observed in steels without grain refining elements such as Al, Nb and V. As mentioned in preceding chapters the level of nitrogen was kept as low as possible to avoid the presence of AlN interfering with the results. It is believed that although as long as we have Al and N in solution the effect of AlN particles cannot be ruled out completely, since the level of nitrogen is extremely low, the influence of AlN on grain growth is somehow negligible due to the very low volume fraction of AlN. Therefore, since there are no other nitride or carbide forming elements present in steel E, the observed type of grain growth cannot be associated with any pinning effect.

As with steel E, which shows the typical grain growth, Fig. 4 shows broadly similar behaviour for steel F with some differences in grain growth slope. Figure 6.4 (steel F) illustrates the gradual grain coarsening with temperature. The comparison between the profile of grain size distribution in steel E and F shows less pronounced

difference between the proportion of finer and coarser grains in steel F i.e. a more uniform distribution even at high temperature. The peak in the grain size distribution appears relatively constant between 1050 and 1150. However, above this temperature a peak in grain size distribution changes markedly indicative of acceleration of grain growth. The grain growth regime does not show any clear sudden grain coarsening at a specific temperature; therefore it is considered that this behaviour cannot be associated with the dissolving or coarsening of AlN particles during the austenitising process. There are also some other reasons to rule out the possibility interference of AlN in grain growth process in this steel:

It was shown that additional Al up to 0.3 wt% can lead to very large AlN particles even in an as rolled microstructure [23]. Although the level of nitrogen in the investigated steels was kept as low as possible to avoid the formation of AlN, some very large AlN particles were still observed (chapter 3); this is a consequence of the formation of particles at high temperature due the levels of Al in steels F and G. According to current theory of grain growth, the larger the precipitate size results in a lower effectiveness. The size of these particles makes them less effective in inhibiting grain growth. Furthermore, the proposed model by Gladman and Pickering [19] can help to clarify the role of AlN in steel F. On the basis of this model, the critical radius of second phase particles, r_c, required to pin effectively grains of radius R was shown to be:

$$r_c = (^{6Rf}/_{\pi})(^{3}/_{2}-^{2}/_{z})^{-1} \qquad \text{(Equation 6.1)}$$

where is R the matrix grain radius, f is the volume fraction of the second phase particles i.e. the pinning particles and z is the grain size heterogeneity factor which is defined as the ratio of radii of growing grains and the matrix grains. To predict the grain size in the presence of specific particles, values of r_c, f and z are required. It has been suggested that a value of 2 for z are not unreasonable [19] and also f can be obtained from MTData results. The model predicts that for an average of 400 nm

AlN particle (from the TEM observations) the predicted grain size for steels F and G should be approximately 730 μm and 780 μm respectively.

Since the value of the grain size in these two investigated steels is much lower than the predicted values, it can be concluded that the AlN particles do not make a significant contribution to the grain size control process in these two investigated steels.

As seen in 6.4 steel G shows change in grain growth regime. In addition to the mean grain size, Fig. 8 shows a very narrow distribution of prior austenite grain size. However, at temperatures above 1200 ºC, grain coarsening can be observed. Hence, based on the discussion above, this is not believed to be related to the coarsening or dissolving of AlN in the austenite matrix. It is understood that segregation of Al atoms to prior austenite grain boundaries can be considered as an alternative interpretation for the observed grain growth. Theoretically, since the atomic radius of Al is 0.143 nm while Fe is 0.126 nm and the difference between these two atomic radii is about 13.5 %, it is more favourable for Al atoms to occupy regions of lattice expansion when they dissolve in the austenite matrix. Thus the distorted lattice within the grain boundaries grain boundaries can provide the driving force for the segregation of Al atoms from the bulk to grain boundaries to decrease the strain energy of grain boundaries. In addition to the theoretical justification for segregation of Al to austenite grain boundaries, Mabuchi el.at. [32-34] have shown significant segregation of Al atoms to grain boundaries in their steels and they suggested that Al is a significant element in suppressing grain boundary segregation of other alloying elements due to their solute interactions.

Based on the previous discussion, it can be deduced that there is enough evidence to justify the segregation of Al to prior austenite grain boundaries (PAGB) and it can also be concluded that the segregated Al atoms would affect the grain boundary mobility. It is well known that during the austenetising process, grain boundaries start to migrate due to temperature activation. However, Al segregated grain boundaries have to drag the Al atoms to move together with boundaries. Therefore the segregation of Al can slow down the mobility of austenite grain boundaries.

In addition to the driving force for segregation of Al atoms to grain boundaries, it is known that the distribution of solute atoms at grain boundaries and also in bulk is a function of temperature and can be defined by the following formula [104]:

$C_g = C_o \exp (E/ RT)$ (Equation 6.2)

Where C_g is the concentration of solute atoms at grain boundaries, C_o concentration of solute atoms in the bulk, E the difference of between the distortion energy of the solute atoms distributed at the grain boundaries and in the bulk, T the absolute temperature and R is the gas constant. According to equation 6.2, the concentration of Al at grain boundaries can be strongly affected by the temperature. In other words, increasing the temperature will lead to more uniform distribution of solute elements (in this case Al) between the matrix and the grain boundary region i.e. less segregated solute atoms at grain boundaries. This means that increasing the temperature can reduce the influence of Al atoms on the mobility of austenite grain boundaries, and at high temperatures there is less or no significant drag effect to inhibit grain boundary migration.

In addition to the concentration of solute atoms at gain boundaries, high specimen temperatures provide a strong high driving force for grain boundary migration. According to solute-drag theory, when the driving force of grain boundary migration is significantly more than the drag resistance of segregated solute element, grain boundaries can rapidly cast off the segregated atoms and move freely.

It is believed that a combination of the two aforementioned mechanisms, results in the austenite grain growth behaviour of steel G. As can be seen, in steel G, sudden grain growth occurs at a temperature of around 1200 ºC. This temperature can be identified as the temperature at which the austenite grain boundaries would be able to migrate regardless of the presence of the Al segregated atoms. It is worth mentioning that the same behaviour has been reported by Qingbo and Ying for Nb steels [104]. However, their work resulted in a very large grained microstructure far larger than for a Nb free steel at 1240 ^{o}C, while in this work steels F and G still have a significantly finer structure even after the onset of sudden grain growth.

6.4. Conclusions:

The results show that apart from AlN, Al as a solute element can affect austenite grain growth behaviour. Steels E and F show somehow typical austenite grain growth. Despite steels E and F, steel G shows completely different type of grain growth which involves sudden grain growth above specific temperature. It is believed that this grain growth regime cannot be associated with the coarsening or dissolving of AlN particles since it has been shown that additional Al content results in significantly coarser AlN particles which make them less effective in the grain pinning process. However, it can be suggested that the observed sudden grain growth regime in Al added steel G can be considered as the consequence of the solute drag effect on the prior austenite grain boundaries.

Chapter 7: The influence of additional Al on isothermal transformation of austenite to ferrite

Introduction

As mentioned in the preceding chapters, the effect of Al as a solute element on steel microstructure cannot be comprehensively studied unless there is a clear understanding regarding the role of additional Al on austenite to ferrite transformation. The broad aim of this chapter is to investigate the influence of Al (as a solute element) on austenite to ferrite transformation. The results from this chapter will help us to have clearer and better interpretation of the results obtained in chapter 3.

Prior to investigating the influence of Al addition on austenite to ferrite transformation, in order to have only the effect of solute Al on transformation behaviour, it was necessary to rule out any other interfering factors which may affect the experimental results. It is well known that prior austenite grain size may have a strong effect on the kinetics of austenite to ferrite transformation [105, 106]. A reduction in the austenite grain size should result in an increase in the rate of transformation since finer austenite grain structure can provide more suitable nucleation sites (grain boundaries) and consequently higher nucleation rate. However, it was shown that the change in prior austenite grain size does not influence on incubation time [105]. Alternatively, according to Capdevila and co-workers [106] prior austenite grain size does not affect the parabolic growth rate constant for allotriomorphic ferrite transformation, hence does not influence growth kinetics. However, since prior austenite grain size strongly affects the nucleation rate, in general it has a strong influence on transformation kinetics.

A series of isothermal experiments was designed to investigate the role of additional Al on austenite to ferrite transformation. Attempts were made to make sure that the results obtained are a direct influence of Al on transformation behaviour and there is

no interference by other factors such as heating procedure and, more importantly, prior austenite grain size on transformation kinetics.

7.1 Experimental

7.1.1 Isothermal Experiment

To investigate the effect of Al additions on isothermal transformation, cylindrical samples 5 mm in diameter and 12 mm in length were made. Subsequently, these samples were heated in the furnace of a Bahr D805 high resolution dilatometer at the same rate as detailed in chapter 6. The holding temperatures for steels E, F and G are 1150, 1220 and 1250 ºC respectively. Based on results presented in chapter 6, the selected holding temperatures led to approximately the same austenite grain size (~150 μm) and also approximately the same grain size distribution. Samples were held at their respective austenitising temperatures for 600 sec before being subsequently quenched to their isothermal temperatures. The chosen isothermal temperatures were as follows: 750 ºC for all steels plus two more isothermal temperatures only for steel G (810 and 940 ºC). A temperature of 750 ºC was chosen for all steels since it is close enough to A_1 to obtain mostly ferritic structure specifically in steel E and also it is not too low that it makes transformation too fast and almost instantaneous for Al added steels (F and G). However, the obtained results show that even at this temperature transformation takes place very quickly.

Two more isothermal experiments were carried out at 810 ºC and 940 ºC. The experiment at 810 ºC was conducted to study the effect of a higher isothermal temperature in steel G and the experiment at 940 ºC was designed to obtain approximately the same under cooling as (E 750 ºC) in steel G. Based on the results given in preceding chapters the critical transformation temperatures (A_{C1} and A_{C3}) especially in steels F and G are highly sensitive to the applied heating and cooling rates. Therefore, the critical transformation temperatures given by MTData were chosen as a zero point to calculate the under cooling for each experiment. In this sense, E 750 ºC and G 940 ºC experiments have the same under cooling, which is approximately 110 ºC. Following the quench to the respective isothermal temperatures, samples were held long enough to complete the transformation and then quenched. Conventional optical metallography was carried out to reveal the

microstructure. EBSD was employed to measure the grain size and grain size distribution. More details regarding the EBSD and metallography procedures can be found in chapter 3.

There are some other technical and practical concerns, uncertainties and limitations that need to be considered and addressed during the interpretation of the results. The most important of which are:

a) Temperature stability: One of the main concerns regarding the dilatometry experiments and specifically quench experiments is cooling rate and also temperature stability after reaching the pre-defined isothermal transformation temperatures. Clearly, size and shape of the sample as well as quenching medium define the applied cooling rate. A hollow sample instead of solid cylindrical one can be utilized to increase the cooling rate. In the case of a hollow sample, temperature gradients between the core and surface would have less of influence on kinetics.

b) Decarburization: The other practical concern which may affect the reliability of experiments is decarburization. It is quite common and sometimes unavoidable in dilatometry experiments. To lower the level of decarburization an improved vacuum and shorter holding times at high temperature (austenetization) may be applied.

In addition to the aforementioned uncertainties, the calculation of ferrite volume fraction from the dilation curve and also transformation starting point, .i.e. zero point of the ferrite volume fraction curve, need to be dealt with carefully. Generally, the dilation of the sample during a phase transformation can be assumed to be largely isotropic. Therefore, the lever rule can be used to calculate the ferrite volume fraction, f_α, from the recorded relative length change during the phase transformation [107, 108]. The final ferrite volume fraction for each sample was then compared to that from manual point counting [109]. Conventional metallography was carried out to reveal the microstructure and EBSD was employed to measure the grain size and grain size distribution. More details about EBSD and metallography can be found in chapter 3.

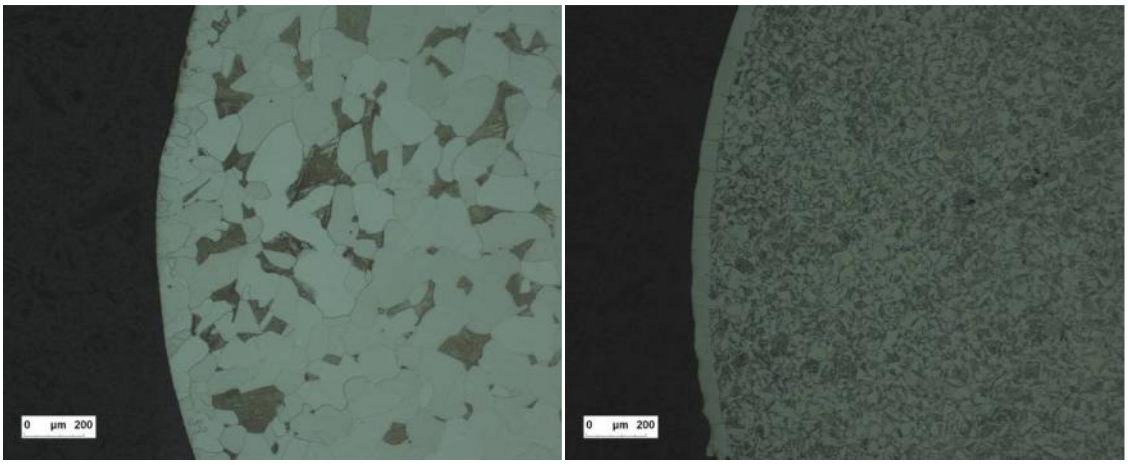

Figure 7.1 Steel E 750 ºC (left) and steel G 750 ºC (right) at low magnification

7.2 Results

As mentioned before, one of the main concerns regarding the dilatometry experiments is decarburization, which may affect the reliability of the obtained results. As figure 7.1 shows (two examples form isothermally transformed samples), in the majority of samples there is no significant sign of decarburization (see E 750 ºC). However, in G 750 ºC there is an approximate 50 µm decarburization layer which is about 2% of the bulk which needs to be taken into account in any interpretation of the results. The other main concern prior to interpretation of the dilation curves is setting the starting point for the isothermal dilation curve i.e. when and where the transformation started. The issue becomes more difficult when there is rapid transformation kinetics or experiments at low isothermal temperatures that accelerate the transformation kinetics. Figure 7.2 magnifies the quenching part of the dilation curves between austenetising and isothermal temperatures. It shows both changes in temperature and length during the quench time (2 s). As can be seen there are some deviations in the temperature versus time diagrams which become more pronounced at higher isothermal temperatures i.e. 810 ºC and 940 ºC in steel G. It is believed that this deviation cannot be interpreted as an indication of austenite to ferrite transformation since:

a) It can only be observed in the temperature/ time diagrams and not in length/ time change diagrams.

b) It takes place approximately at the same temperature for all isothermal experiments; whereas if it was anything to do with transformation, it should have taken place at different temperatures for different steels. It should be noted that based on previous chapters it is clear that additional Al has a very strong effect on A_3 and consequently each investigated steel should have totally different A_3.

c) Finally, it is believed that if it was anything to do with the starting point of the austenite to ferrite transformation, it should have appeared at significantly lower temperatures instead of somewhere between 1100-1000 ºC. Based on what has been discussed in chapters 4 and 5, a higher cooling rate would lead to lower critical transformation temperatures. However, these deviations in temperature diagrams occur far above Ae_3 for steel E and just about Ae_3 for steel F.

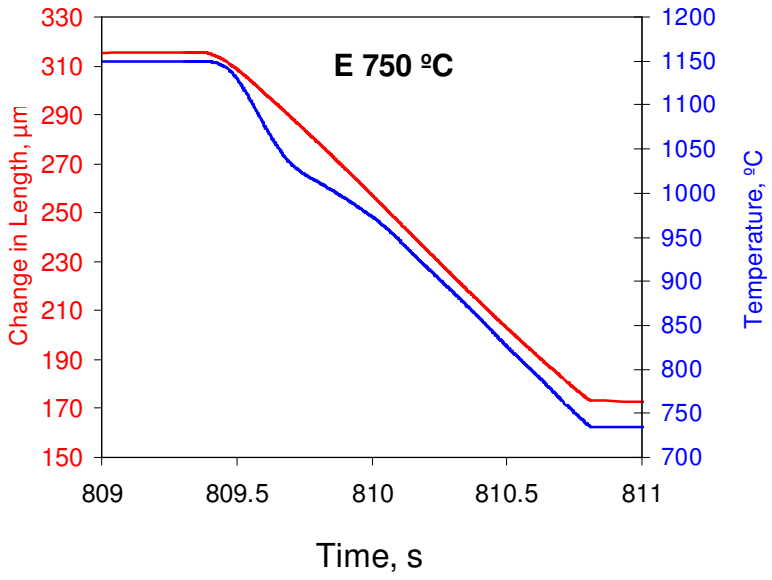

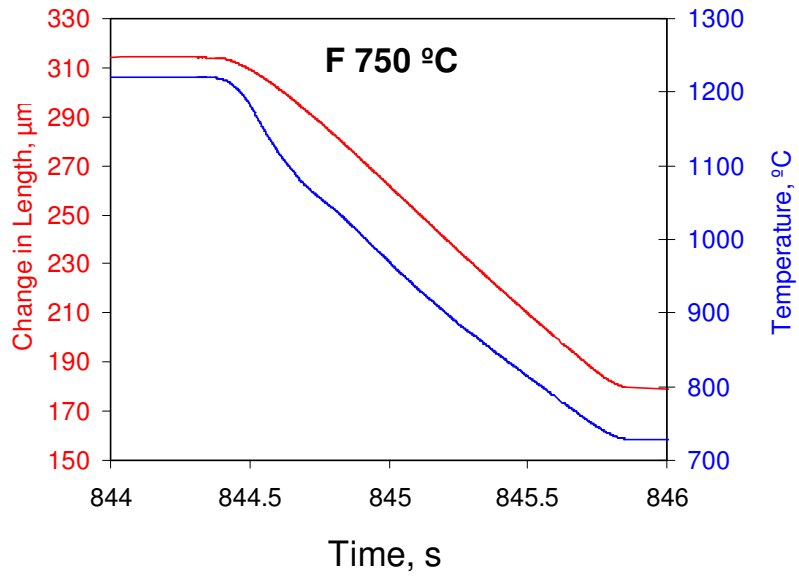
F 750 ºC
Change in Length, µm
Temperature, ºC
330
310
290
270
250
230
210
190
170
150
1300
1200
1100
1000
900
800
700
844
844.5
845
845.5
846
Time, s

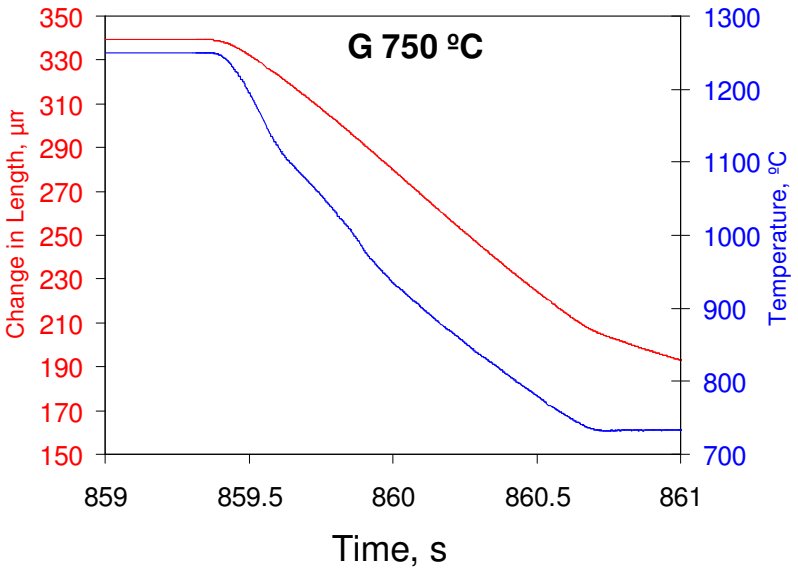
G 750 ºC
Change in Length, µm
Temperature, ºC
350
330
310
290
270
250
230
210
190
170
150
1300
1200
1100
1000
900
800
700
859
859.5
860
860.5
861
Time, s

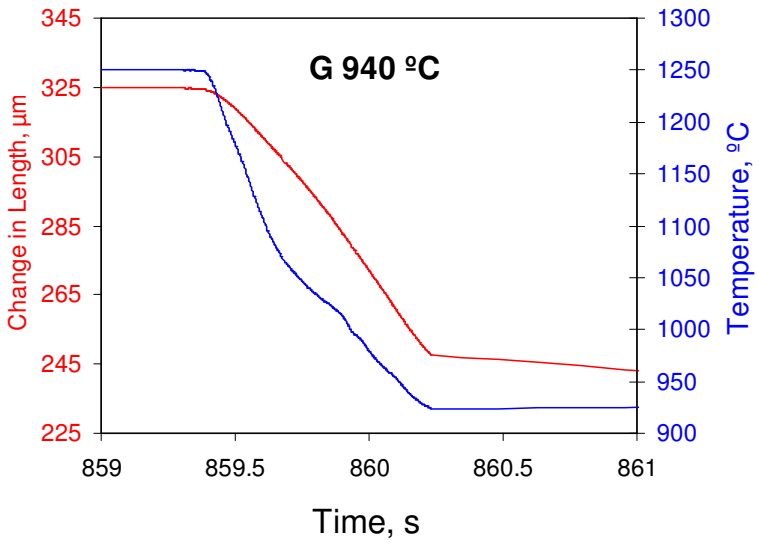

Figure 7.2 Change in length and temperature during the quench from austenetising temperatures to isothermal temperatures for each isothermal experiment.

Considering all the reasons mentioned above, the conclusion is that the transformation takes place at a very high rate in low carbon steels and cylindrical specimens do not provide the highest cooling rate (in comparison with hollow specimens); the deviations in the temperature diagrams during cooling prior to isothermal holding cannot be interpreted as a sign of transformation. Due to the fact that there is no other evidence to support the austenite to ferrite transformation throughout this specific time, it can be concluded that the transformation takes place just after reaching to the isothermal temperatures.

The other issue which needs to be considered is how the zero point for the dilation curves can be set. Since it is required to compare the effect of additional Al on austenite to ferrite isothermal transformation, it is necessary to be consistent in setting a zero point for each curve. The chosen zero point for each experiment is given in Fig. 7.3. Basically, the arrow in each diagram is the first point that the dilation curve begins to rise and this increase was taken as an indication of the beginning of the transformation. Figure 7.3 illustrates that the temperature variation at the start point is constant within +/- 1 °C and there is no significant change in recorded temperatures after reaching this point. Figures 7.4-7.6 show the metallography images of steels E, F and G respectively. There are significant

differences among the investigated steels as well as different isothermal temperatures which can only be associated with the effect of deliberately added Al in the investigated steels. Table 7.1 shows the ferrite grain size obtained by EBSD and the ferrite volume fraction obtained by the point counting method. The EBSD results as well as the metallography images show that aluminium additions result in a higher ferrite volume fraction and also finer structure. An approximately 1 wt% Al addition (steel G) leads to a 20% increase in ferrite volume fraction while resulting in significant grain refinement (28.1 μm to 12.2 μm). Furthermore, the results show that increasing isothermal temperature may lead to a fall in ferrite volume fraction as expected. However, in the case of steel G, we obtain a finer ferrite grain structure which was not expected.

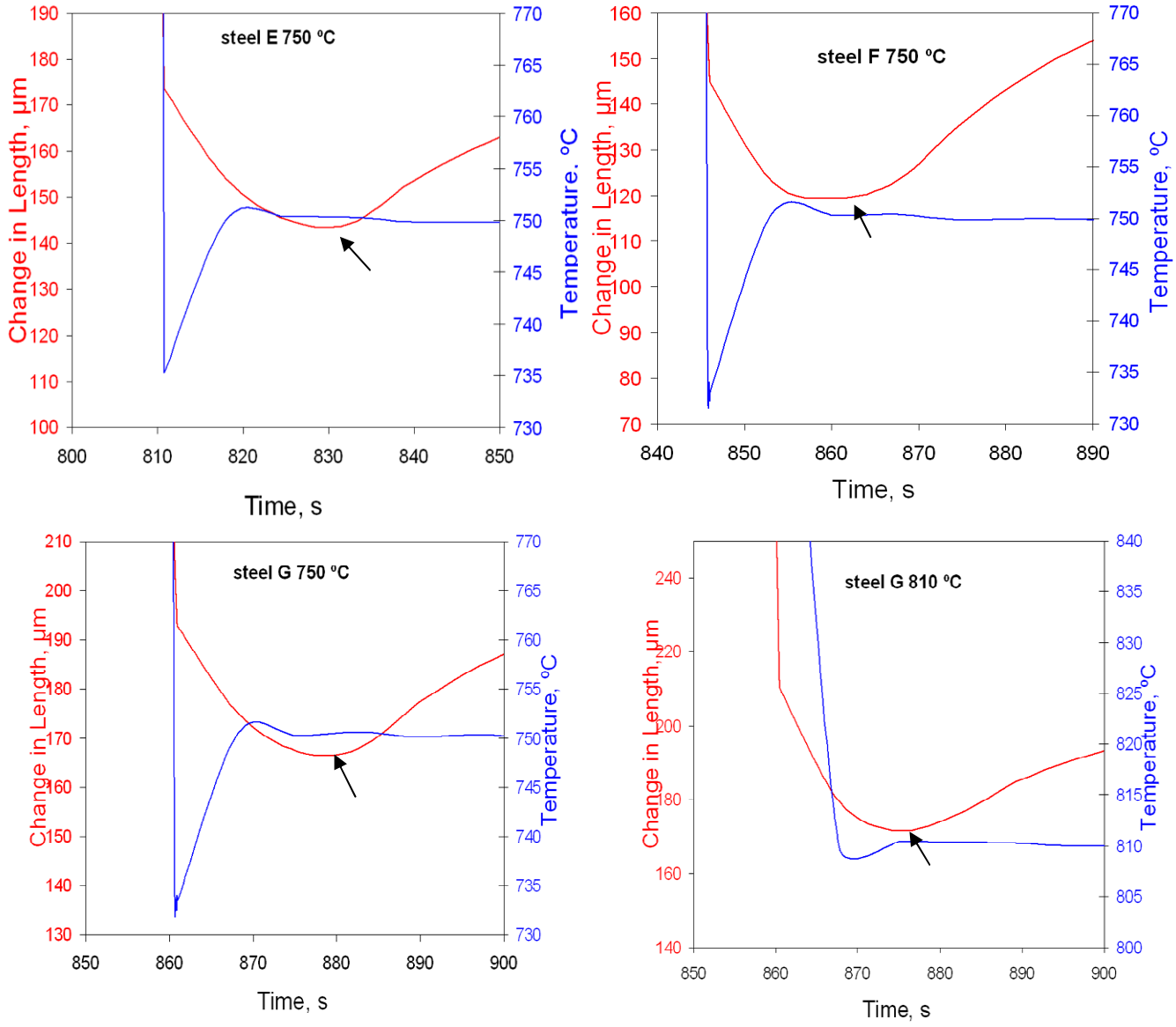

Figure 7.3 Temperature variation after allocated point is at a quite steady state.

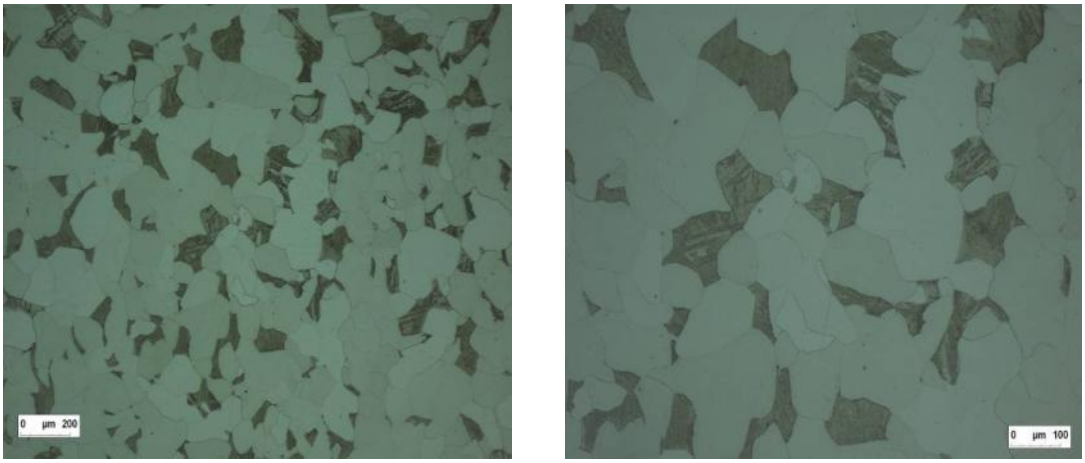

Figure 7.4 Metallography images for steel E transformed at 750 ºC

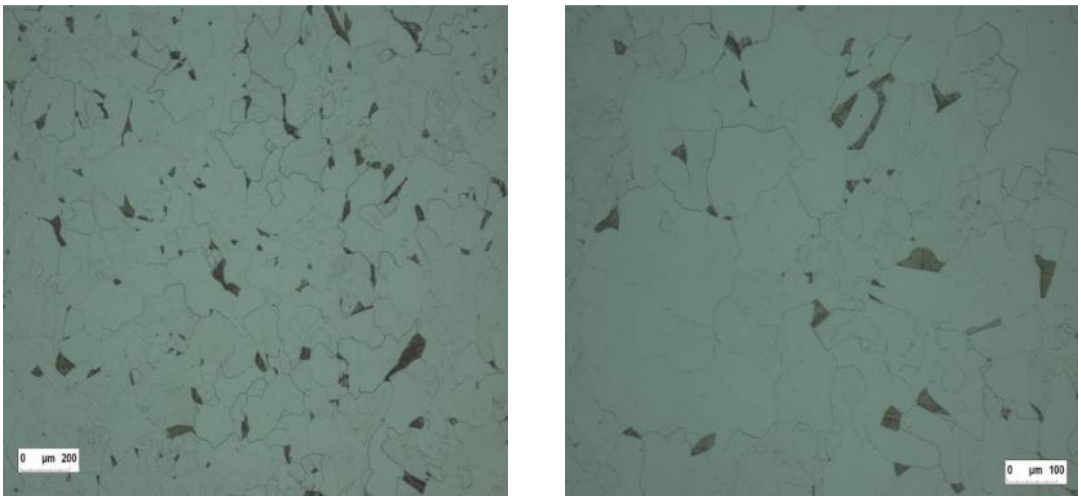

Figure 7.5 Metallography images for steel F transformed at 750 ºC

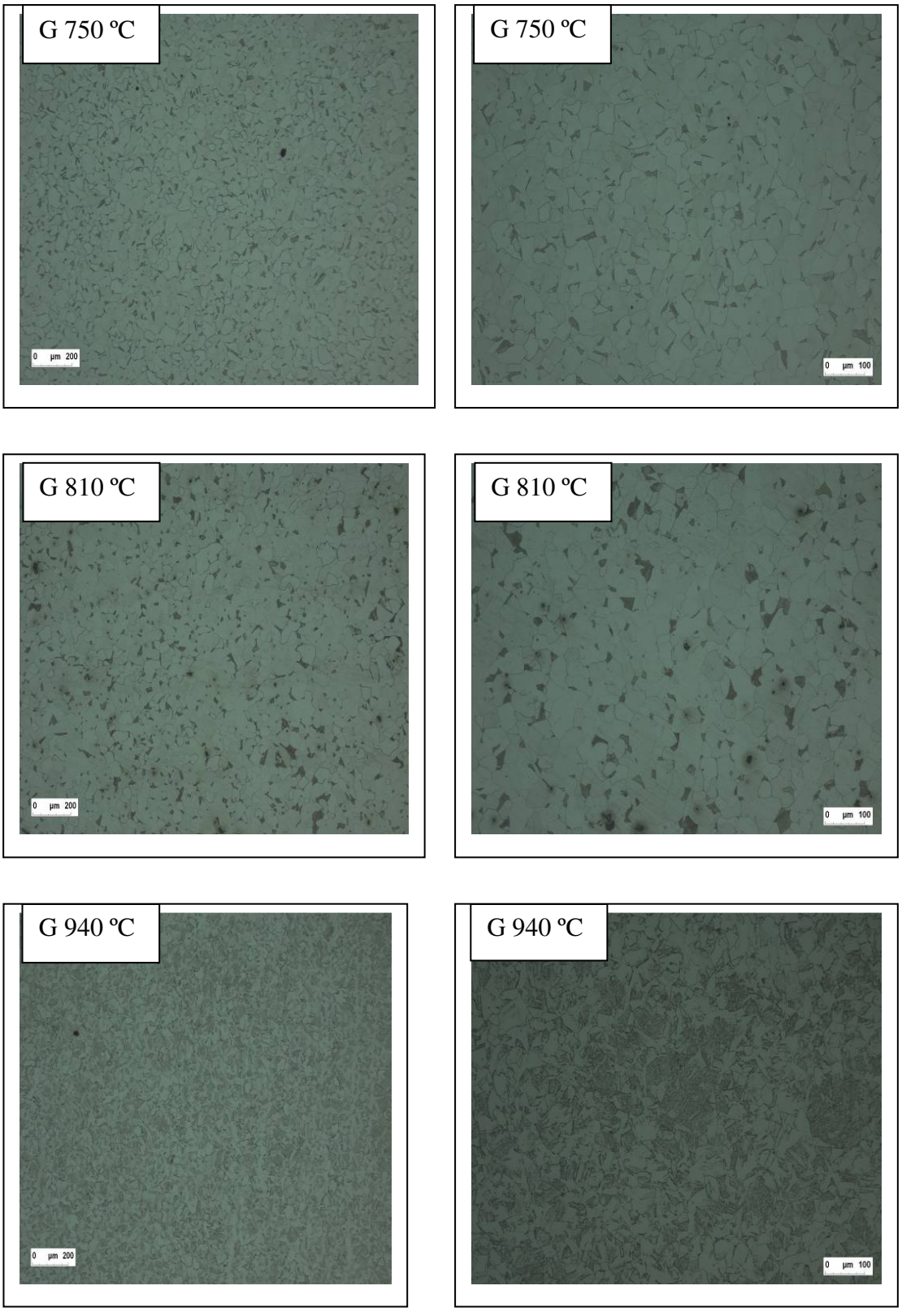

Figure 7.6 Metallography images for steel G transformed at 750 ºC, 810 ºC and 940 ºC

Table 7.1 Ferrite grain size and volume fraction for each isothermal experiment

	Ferrite volume fraction (point counting)	Ferrite grain size µm (EBSD)
E IT 750	75%	28.1
F IT 750	92%	22.8
G IT 750	94%	12.2
G IT 810	91%	13.1
G IT 940	76%	8

In addition to the effect of excess Al on ferrite grain size and volume fraction, the effect of excess Al on ferrite grain size distribution has been examined for each isothermal experiment. Figure 7.7 shows the grain size distribution for each steel sample investigated at 750 ºC and Fig. 7.8 shows the grain size distribution just for steel G but at different isothermal temperatures. The data reveals that steel E 750 ºC as well as steel F show very wide and somewhat bimodal (specifically steel E) grain size distributions whereas increasing the level of Al to 0.98 wt % leads to very narrow and sharp grain size distribution. Direct comparison between E 750 ºC and G 750 ºC shows that all the large grains (above 2000 μm^2) have been eliminated and the mean value shifted from ~2600 to 600 μm^2. In addition to the change in steel composition, the results show that the variation in isothermal temperature may result in a different ferrite grain size and grain size distribution. Although it was expected to obtain a coarser grain structure while the isothermal temperature is increased, in contrast significantly finer grain structures were obtained after raising the isothermal temperature from 750 ºC to 940 ºC in steel G . All isothermal temperatures in steel G show a very smooth distribution of the ferrite grains. This smooth distribution is not significantly affected by variation of the temperature.

Further to microstructural analysis, the dilation curves provide valuable information regarding the role of additional aluminium in austenite to ferrite transformation kinetics.

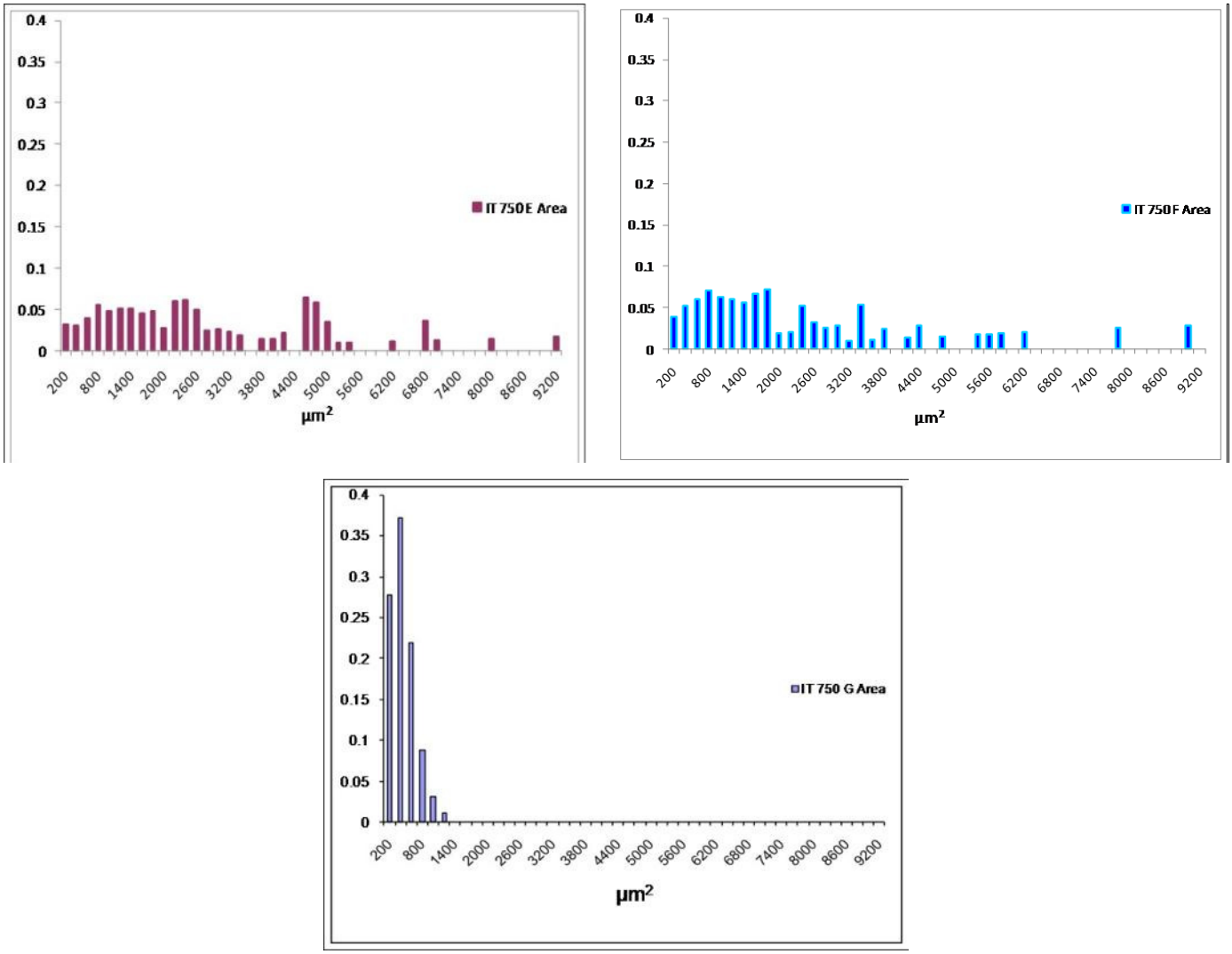

Figure 7.7 Grain size distribution for three investigated steels at 750 °C

Figures 7.9 and 7.10 show the effect of steel composition and also isothermal holding temperature on austenite to ferrite transformation respectively. The time axis has been presented on both linear and logarithmic scales in the figures in order to reveal more details of the transformation behaviour. It should be noted that the results from the dilatometry experiments have been normalized based on the given ferrite volume fraction in Table 7.1 and therefore the final ferrite volume fraction varies from experiment to experiment. The results show very fast transformation in all experiments. It should be born in mind that the initial point for each curve was chosen at the exact point where the change in length within the diagrams started to rise. In other words any incubation time (if there is any) would be missed.

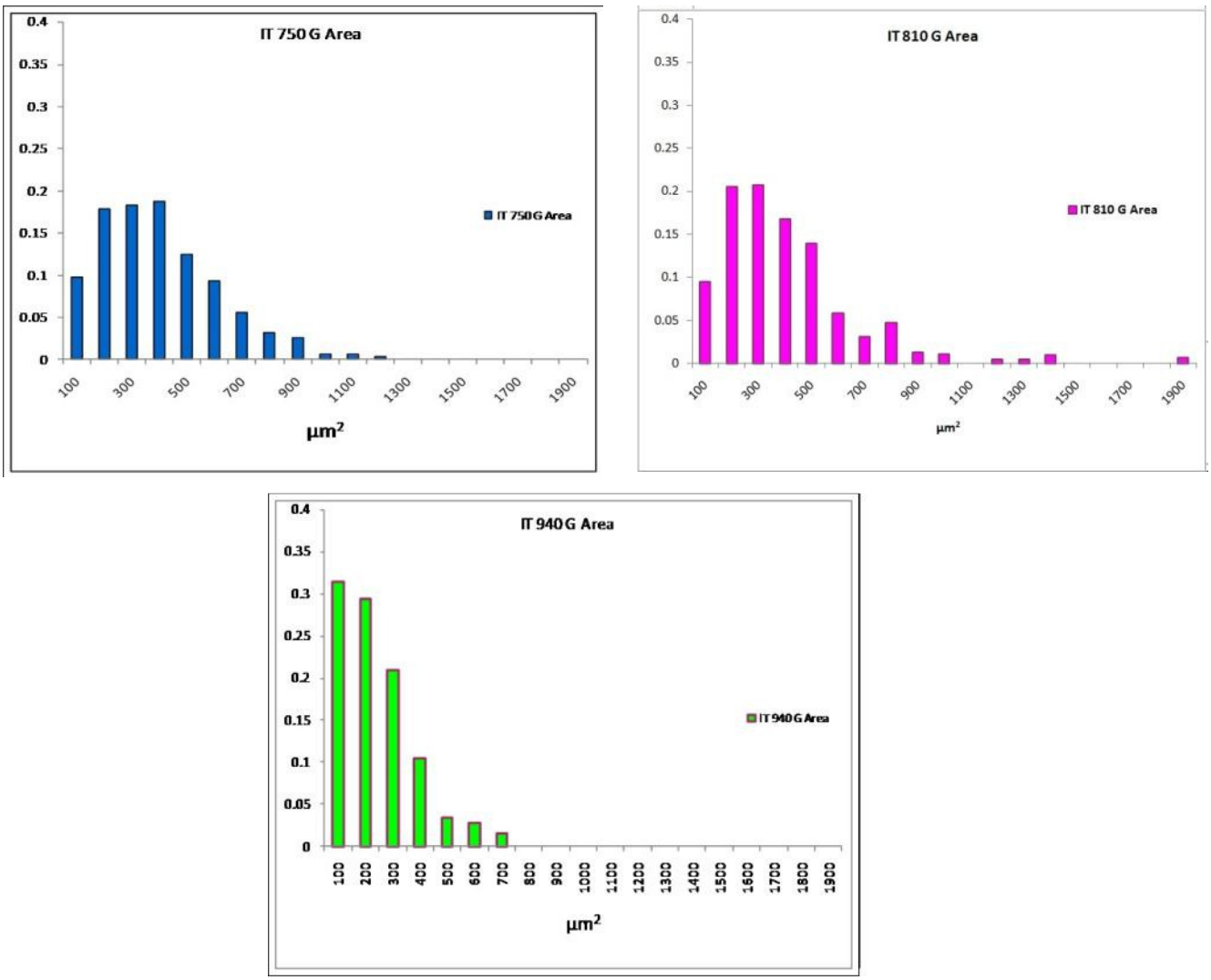

Figure 7.8 Grain size distribution for steel G at different isothermal temperatures 750 ºC, 810 ºC, 940 ºC.

As expected, increasing the amount of Al in the steel results in increase of the transformation kinetics in steels F and G as shown in Fig. 7.9. However, the results do not show any significant change in transformation behaviour between steel F (0.48 wt % Al) and steel G (0.94 wt % Al) in the 750 ºC isothermal experiment.

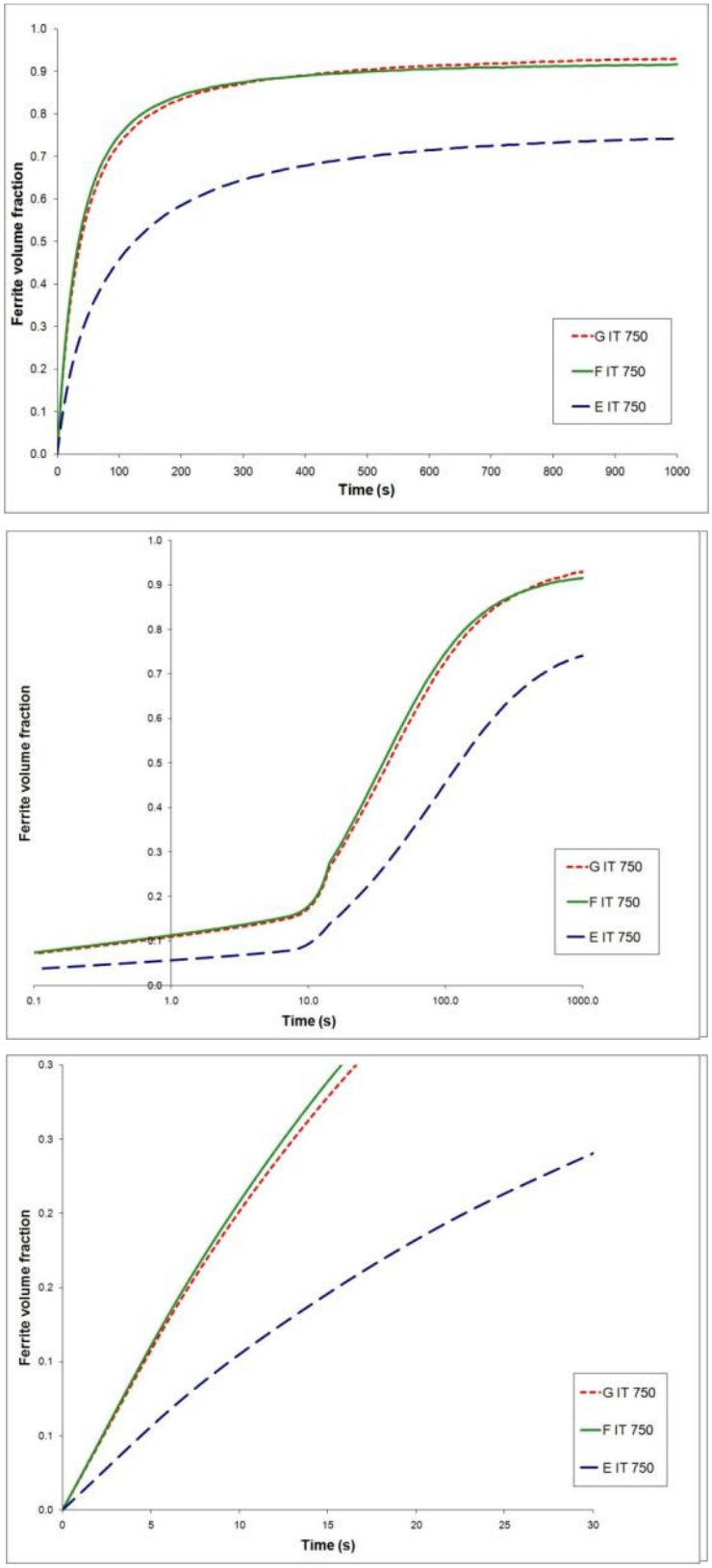

Figure 7.9 Dilation curve, ferrite volume fraction vs. time, for steels E, F and G at 750 ºC

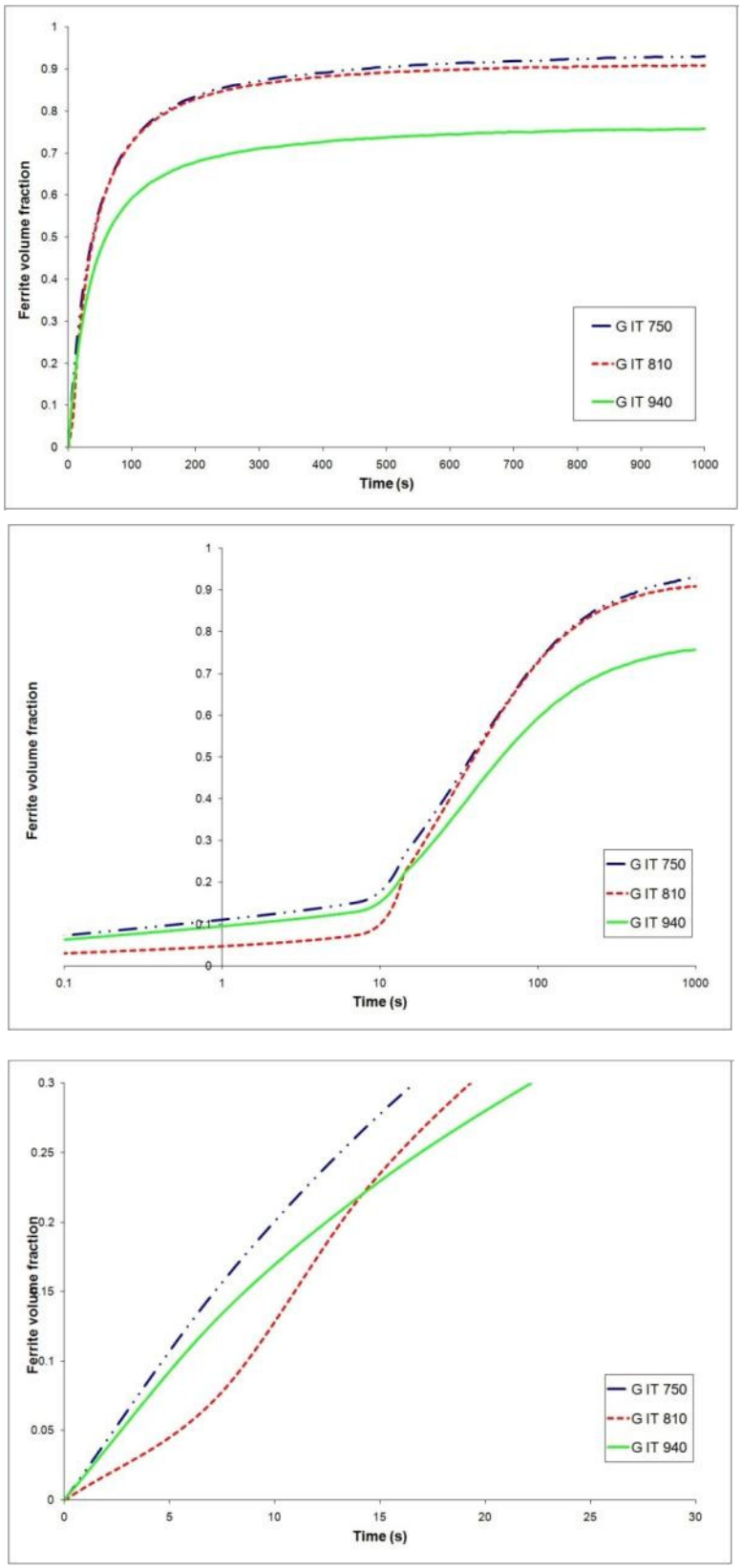

Figure 7.10 Dilation curve, ferrite volume fraction vs. time, for steel G at 750, 810 and 940 ºC

Based on the results observed, the transformation behaviour can be divided into two steps. The first step takes place during the first 10-15 sec of transformation. This step, which is possibly dominated by nucleation of ferrite, occurs very rapidly. For instance, for G or F at 750 ºC approximately 30% of the austenite transforms to ferrite in just the first 15 sec of transformation while the remaining 70% takes about 1000 sec to be transformed to ferrite. The same thing happens in steel E at 750 ºC, however it is less pronounced. As seen, Al additions have a significant effect in the first step of transformation. Comparison between steels E, F and G at 750 ºC shows that Al accelerates this phenomenon which results in a higher amount of transformed ferrite (this can possibly be interpreted as a higher nucleation rate) in the first step of transformation. Despite the influence of Al content on this first step of transformation, the isothermal holding temperature does not show a consistent influence on the first step of transformation in steel G. Comparison between G at 750 ºC and at 810 ºC shows that increasing the isothermal temperature may lead to lower rate in the first step of transformation. However, the result obtained from G 940 ºC is very similar to G 750 ºC and does not show the phenomenon i.e. at the first stage G at 810 ºC shows a slower transformation rate in comparison with G at 750 ºC; whereas increasing the isothermal transformation temperature form 810 to 940 ºC accelerates the transformation rate at this step.

Following the first step, the second step starts approximately after the first 10-15 sec of transformation in all steels. As illustrated in both Figs 7.9 and 7.10, the transformation rate in this step is not as high as the first one. By considering the transformation rate and also the volume fraction of ferrite at this stage, this step can be assumed to be controlled by the ferrite growth kinetics. Figure 7.9 shows very similar behaviour in this second step for steels F and G, whereas steel E shows significantly different behaviour in this step as well as the first one. In addition to the effect of excess Al on the second part of the dilation curve, the results show that increasing the isothermal temperature from 750 ºC to 810 ºC does not affect the second step of transformation. However, increasing the temperature to 940 ºC influences the transformation behaviour drastically at this stage.

7.3 Discussion

Prior to discussing the results obtained from the isothermal experiments, it is necessary to have an overview regarding the main factors and parameters which define the transformation behaviour.

Solid-solid transformation is a topic which has been subject to much research [8, 107, 108, 110-115]. One of the most common approaches to this type of transformation is based on the theory developed by Johnson, Mehl and Avrami [116]. This approach considers β as the precipitate particle forming in an existing phase γ, after an incubation time τ. This approach assumes that β grows isotropically with a constant rate *G*. According to this theory the volume fraction of the transformation product at a time *t* may be given as:

$$V_{f\beta} = 1 - \exp(-kt^n) \qquad \text{(Equation 7.1)}$$

where *n* and *k* are constants. An alternative form of above equation may be written as:

$$1\text{-}V_{f\beta} = \exp -(IGt)^n \qquad \text{(Equation 7.2)}$$

where *I* is the nucleation rate and *G* is the growth rate. It other words, the volume fraction of the transformation product is a function of nucleation and growth [115]. It has also been shown that the nucleation rate can be affected by various parameters such as the free energy required for formation of the critical embryo and the activation energy associated with diffusion across interface. The nucleation rate "*I*", may be expressed as [8]:

$$I = I_0 \exp(-\Delta G_t^* / kT) \exp(-\Delta G^* / kT) \qquad \text{(Equation 7.3)}$$

Where I_o is a constant, ΔG_t^* the activation free energy for diffusion across the interface and ΔG^* is the critical free energy for formation of a nucleus. Moreover, it

is known that the free energy required for formation of the critical sized embryo varies inversely as the square of the degree of supercooling (undercooling):

$$\Delta G^{*} = \frac{A}{\Delta T^{2}} \qquad \text{(Equation 7.4)}$$

Therefore, the free energy required to form a critical embryo decreases with supercooling. In other words, undercooling plays a very significant role in the nucleation rate and increasing the undercooling results in an increase in the nucleation rate. It should be born in mind that in addition to ΔG^{*}, the nucleation rate is also influenced by ΔG_t^{*} which represents the activation energy for diffusion across the interface. This activation energy increases continuously with decreasing temperature and therefore a large undercooling may result in a decrease in the nucleation rate.

As mentioned before, the austenite to ferrite transformation comprises three overlapping steps: nucleation, growth and impingement [108, 114]. This means that in addition to the nucleation step, the growth step can also define the final product of transformation in the austenite ferrite transformation.

Based on what has been discussed in section 1.2.2.1, the diffusion of carbon is the limiting factor for ferrite growth in austenite to ferrite transformation. According to Zener theory [103], the interface growth depends on the square root of the diffusion coefficient for carbon in iron. In addition to carbon diffusion, the interface position varies with the square root of the time and the growth velocity varies inversely with as the square root of time. However, the condition becomes more complicated when a substitutional element is added to the system [12, 13, 15, 117-119]. As discussed in chapter 1, the transformation may be controlled and slowed down depending on whether the substitutional atoms are partitioned between the austenite and the ferrite. The general overview concerned with three possible thermodynamic conditions for growth, i.e. local equilibrium with partitioning (P-LE), local equilibrium with negligible partitioning (NP-LE), and paraequilibrium (PE), was given in chapter 1. As mentioned there, the growth regime mechanism may differ even within the samples of the same composition. Also, the particular growth regime for each system

depends on the additional substitutional element. A clear classification based on the interaction between X (substitutional element) and C and X and the interphase boundary recently was suggested by Aaronson [12]. Based on this classification, those elements which have a weak interaction with carbon and have barely any interaction with the interface (Ni for example) can be expected to have only a very small influence (solute drag effect) on ferrite growth in the austenite to ferrite transformation. However, elements which show a stronger interaction with the moving interface (Mo for instance) are likely to display solute drag effects and have a proportionally greater influence on transformation. On the other hand, there are some elements such as Nb or V which exhibit a very strong carbide forming tendency. This group of elements can be classified as those elements which have very strong influence on austenite to ferrite transformation. However, regardless of the growth mechanism, addition of substitutional elements will not lead to an increase in growth rate in austenite to ferrite transformation.

7.3.1 Isothermal experiments at 750 ºC

As explained in the previous section, the additional Al shows a very strong effect not only on ferrite grain size and grain size distribution but also on ferrite volume fraction in each isothermal experiment for 750 ºC (see Table 7.1). As shown in the preceding chapters, Al is a strong ferrite stabilizer element that increases the Ac_3, and consequently, according to the lever rule, a more ferritic structure can be expected at 750 ºC in steels G and F rather than steel E. It is also expected that there will be higher nucleation rates for steel G and steel F than steel E respectively, simply because G 750 ºC has the highest ΔT among three experiments (since it has the highest Ac_3) and therefore highest ΔG^*. The same thing would be applicable for steel F in comparison with steel E. It should be noted that since the investigated steels have a more or less similar austenite grain size, the main remaining factor which influences the nucleation rate is ΔG^*. Figure 7.9 compares the dilation curve for these steels at 750 ºC. As illustrated, the dilation curves for steels F and G at the about first 20 sec of transformation are very similar. However, steel E shows significantly slower transformation kinetics and lower ferrite volume fraction. This

may suggest that the nucleation rate in steel F and G is significantly higher than in steel E.

The same observation has been reported by Enomoto and Aaronson in the case of Si added steels. They showed that addition of Si leads to acceleration in allotriomorph ferrite nucleation [120]. It should be mentioned that Al, like Si, is a ferrite stabilizer and it is very likely to behave as other ferrite stabilizers.

Therefore, the difference in the ferrite grain size and grain size distribution between steel E and two other Al treated steels can be associated with the difference in ΔT and consequently ΔG^* which leads to a higher nucleation rate.

There is also no obvious difference between the dilatometry results obtained from steels F and G at the very early stages of transformation; however, there is considerable difference in the final ferrite structure in terms of grain size and grain size distribution. In other words, based on the dilatometry results, the nucleation stage apparently shows little difference whereas the final transformation products show a considerable difference. There is one possible interpretation for this phenomenon which is the solute drag effect. As discussed in chapter 6, Al seems to be very influential in amounts of ~1 wt% in controlling the grain size. Therefore, the observation of a significant difference in final grain size, despite similarity in nucleation stage in steel F and G, can possibly be associated with the solute drag effect on ferrite grain growth in steel G. However, it should be born in mind that based on the discussion above, Aaronson [12] suggests that Al does not seem to have a remarkable solute drag effect in steel due to the lack of interaction between Al and C.

In addition, the possibility that steel G has a higher nucleation rate cannot be ruled out completely, simply because steel G at 750 ºC has a higher ΔT. Thus, it can be concluded that the difference in ferrite grain size can be attributed to the differences in growth and nucleation rate, despite the fact that the difference in nucleation rate cannot be deduced from the dilation curves.

7.3.2 Isothermal experiments for steel G at different temperatures

As can be seen in Table 7.1 that increasing the isothermal temperature results in having a less ferritic structure in each isothermal sample which was expected. Increasing the isothermal temperature does not have a consistent influence on ferrite grain size and ferrite grain size distribution.

Based on ΔG^* and ΔT arguments, an increase in isothermal temperature should lead to a lower ferrite nucleation rate and consequently a coarser ferrite grain size, which is more or less true between 750 ºC and 810 ºC. As shown in Fig. 7.8, the ferrite grain size distribution for G 810 ºC in general shows a slightly wider grain size distribution (existence of grains coarser than 1300 μm^2); however, the distribution profile for grains finer than 900 μm^2 is slightly shifted to the left (810 ºC).

In addition to the grain structure, the dilation curve (Fig. 7.10) shows a slower trend in the first part of transformation (about the first 20 sec of transformation) in 810 ºC than in 750 ºC. It seems that an increase in isothermal temperature decelerates the transformation or specifically nucleation rate. However, when transformation proceeds, the difference becomes progressively less and the two dilation curves come together more or less 80 sec after transformation begins.

In contrast, an increase in isothermal temperature from 810 ºC to 940 ºC does not show any further decrease in transformation kinetics. Based on the results obtained from 810 ºC, it was expected to get a coarser ferrite grain size and wider grain size distribution in comparison in 940 ºC simply because an increase in isothermal temperature should lead to a lower ferrite nucleation rate and consequently coarser ferrite grain size. However, the obtained grain size at 940 ºC is finer and the grain size distribution shifted to the left. In addition to ferrite grain size, the dilation curve shows that an increase in isothermal transformation temperature accelerates the transformation kinetics (specifically in the first part of transformation) and makes the dilation curve for 940 ºC comparable to 750 ºC which is in fact 190 ºC below this isothermal temperature. The results obtained from 940 ºC seems to be not quite in

line with the previous way of interpretation of the results just based on ΔG^* and ΔT argument. One might suggest that this effect might be attributed to the activation free energy for diffusion across the interface i.e. since the absolute temperature is higher in 940 ºC than 810 ºC; this might affect the nucleation rate and increase it. Nonetheless, if this was the case, it should have been observed when comparing 750 ºC and 810 ºC i.e. the nucleation rate should increase in the 810 ºC isothermal experiment. The other potential interpretation for this can be associated with different possible mechanisms for ferrite transformation i.e. interface controlled and diffusion controlled. Recently it has been shown that the transition from one mechanism to another one can affect the transformation kinetics but also may influence the grain size and grain size distribution [13, 108]. However, it is believed that further investigations need to be carried out to understand the mechanism in which Al affects the ferrite transformation and the results obtained from the isothermal experiments would not be enough to provide a full interpretation to obtain a comprehensive understanding regarding the effect of Al on ferrite transformation.

The other contradiction for the ΔT argument arises when we compare E 750 ºC with G 940 ºC. Based on MTData calculations presented in the preceding chapters, both the aforementioned isothermal experiments have approximately the same undercooling which basically means more or less the same nucleation rate. The fact that they have roughly same final ferrite volume fraction after completion of the transformation, (see Table 7.1) strengthens the argument that they have similar under-cooling. However, as Fig. 7.11 illustrates, there is a difference between the transformation kinetics of E 750 ºC and G 940 ºC. It shows that although they have the same ΔT, the transformation kinetics in G 940 ºC is significantly faster and also the obtained ferrite microstructure is significantly finer.

The reason for this phenomenon is unclear to the author. However, it can be suggested that this should be due to the influence of Al on transformation mechanism since the prior austenite grain size is more or less the same as is ΔT.

The other possibility could be segregation of Al into austenite grain boundaries. As mentioned in chapter 1, there is some literature concerned with the segregation of Al

to austenite grain boundaries [32, 34]. It is well established that austenite grain boundaries are preferential sites for ferrite nucleation and if Al segregates to these boundaries they will be more favourable for ferrite nucleation since Al is a ferrite stabilizer. However, there is no direct evidence available to support the effect of segregated Al on nucleation rate. Further dedicated research is required to examine this hypothesis further.

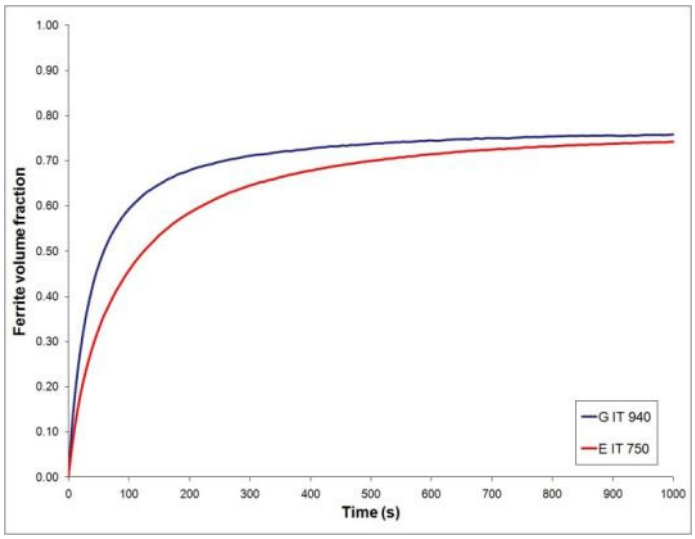

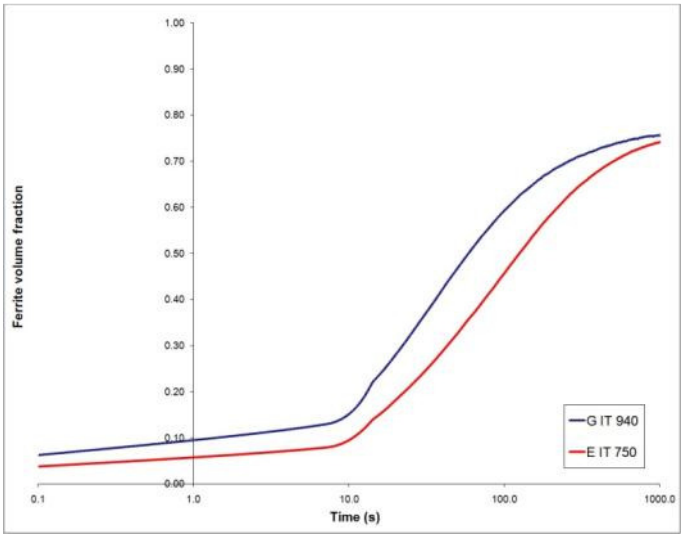

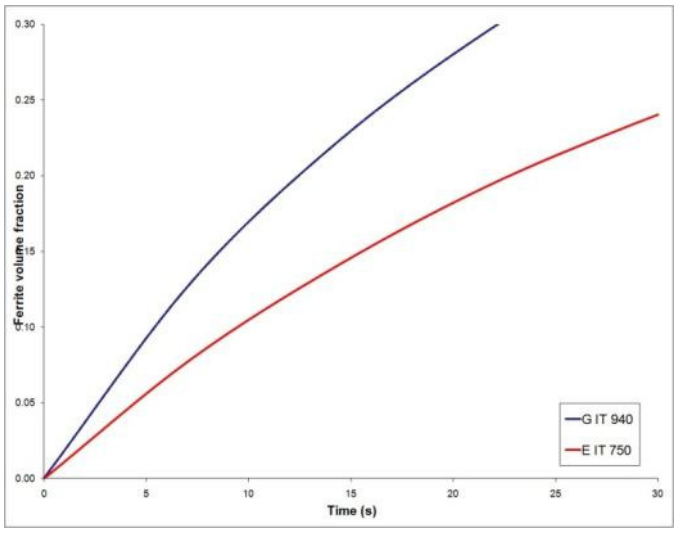

7.11 Comparison between E 750 º C and G 940 º C isothermal experiments (same ΔT)

7.4 Conclusion

From our results we come to the conclusion that additional Al increases the ferrite nucleation rate and possibly decelerates the ferrite growth rate which affects the ferrite transformation kinetics and consequently the transformation product (ferrite grain size and ferrite grain size distribution). This can be associated with the effect of Al on Ac_3 and consequently the effect of additional Al on ΔT (undercooling). However, the comparison between steel E transformed at 750 ºC and steel G transformed at 940 ºC, which have roughly the same undercooling with respect to their own Ac_3, shows a significant difference in transformation kinetics. In other words, undercooling is not the only factor which determines the transformation kinetics. Further investigation is needed to fully understand the effect of Al on ferrite transformation.

Chapter 8: Final conclusions

To investigate the role of Al in influencing steel microstructure, steels with three different Al compositions were designed and prepared. As mentioned in chapter 2 the level of nitrogen was kept as low as possible to avoid interference of AlN in the microstructure. As mentioned in chapters 3 and 6 although some AlN particles were observed in the steel microstructures, the presence of AlN cannot contribute to the changes in steel microstructure due to their particle size. The results on as the rolled microstructures led us to conclude that:

- Apart from the effect of Al as a nitride forming element (AlN), Al in solid solution can affect the ferrite grain size and ferrite grain size distribution in the as rolled structure. Higher Al content leads to a finer ferrite grain size and also to more uniform ferrite grain structure.

- In addition to ferrite grain structure, EBSD results showed considerable correlation between the amount of low angle grain boundaries and the difference between Ae_3 and FRT for each steel.

To understand the role of additional Al on steel microstructure and the influence of Al on ferrite grain size and ferrite grain size distribution it was required to understand the role of Al on austenite to ferrite transformation. Since it was believed that the austenite structure plays a significant role in the austenite to ferrite transformation, prior to investigating the role of Al on austenite to ferrite transformation it was decided to study the role of Al on austenite formation and specifically austenite grain growth. The study on the role of Al on austenite formation revealed the following points:

- It was observed that while temperature Ac_1 remains almost unaffected, temperature Ac_3 increases noticeably with the aluminium content of the steel. The experimental results were consistent with the MTData calculations.

- It was shown, in Al added steels, that the heating rate has a strong influence on Ac_3. The dilatometry results showed that a slower heating rate results in a higher temperature Ac_3.

The most likely interpretation for the effect of heating rate on Ac_3 temperature was the diffusion or partitioning of Al to the final remaining ferrite grains at temperatures close to Ac_3. To confirm this idea a series of experiments were designed and conducted based on steels with 0.48 wt% Al. The results showed that the increase in Ac_3 temperature in the Al alloyed steel during slow (0.05 ºC/s) heating as compared with fast (7 ºC/s) heating conditions is due to the partitioning of Al atoms from austenite to the untransformed ferrite, so further stabilizing this phase. In addition, the results show that partitioning of Mn takes place between austenite and ferrite during slow heating.

The other important factor in the austenite to ferrite transformation is austenite grain size. Following the investigation of the role of Al in austenite formation, the effect of Al on austenite grain size was studied. The results showed that apart from AlN, Al as a solute element can significantly affect austenite grain growth behaviour. The effect of Al was more profound in steel with 0.98 wt% Al. Since the observed effect could not be associated with AlN particles, the change in growth rate was assumed to be due to the solute drag effect of Al atoms on austenite grain growth.

Based on the obtained results from austenite formation and austenite grain growth experiments, a set of experiments were designed to investigate the role of additional Al on austenite to ferrite transformation. The heating cycle was designed to avoid partitioning and also the austenetisation temperature was chosen for each steel to obtain approximately the same prior austenite grain size. The results from the isothermal transformation experiments showed that Al as a solute element increases the ferrite nucleation rate and possibly slows the ferrite growth rate which affects the ferrite transformation kinetics and consequently ferrite grain size and ferrite grain size distribution. This can be associated with the effect of Al on Ac_3 and consequently the effect of additional Al on ΔT (undercooling). However, in the case of having the same undercooling, but different isothermal temperatures, the 0.02 and

0.98 wt% Al added steels still showed higher transformation kinetics. This may imply that undercooling is not the only parameter that affects the transformation kinetics in Al added steels.

Therefore, it can be concluded that additional Al not only affects the austenite grain size in the steel structure, which leads to finer ferrite grain structure, but also influences the austenite to ferrite transformation kinetics. Both of these mentioned phenomena may result in a finer ferrite grain structure in the as rolled Al added steels.

Future work

In order to have a better understanding in relation to the role of excess aluminium in steel microstructure, three low carbon low nitrogen steels have been investigated in the present research. As mentioned in chapter 2, in order to minimise the effect of carbon and nitrogen on steel microstructure and concentrate on the role of aluminium, it was decided to work on low carbon, low nitrogen steel. However, the next step will be for the author to focus on more industrial relevant compositions i.e. slightly higher carbon and higher nitrogen content in order to link the research to the steel industry.

The investigation of the aluminium segregation to prior austenite grain boundaries is the other topic which can be considered as potential future work. It was shown in chapter 7 that aluminium would accelerate ferrite nucleation. This increase in ferrite nucleation is partially related to the effect of aluminium on undercooling, however, it also can be related to the segregation of aluminium to prior austenite grain boundaries. The FIB/TEM technique, which was employed in chapter 5 to reveal the partitioning of aluminium in to ferrite, may be utilised to investigate the segregation of aluminium to prior grain boundaries.

The other potential future work would be to consider the effect of aluminium on austenite formation. The results presented in chapter 4 revealed the influence of aluminium on critical transformation temperature, however, the effect of aluminium on austenite growth and morphology needs to be investigated properly. Furthermore, the effect of aluminium on austenite grain growth is the other subject which needs further study. The austenite grain size was measured at several temperatures in order to have an overall view regarding the role of aluminium in austenite grain growth; however, more austenite grain size determinations at different temperatures need to be conducted in order to obtain a comprehensive overview of the role of excess aluminium in austenite grain growth.

Refrences

[1] D. S. Kristina Beskow, Scandinavian Journal of Metallurgy 32 (2003) 8.

[2] V. Massardier, V. Guétaz, J. Merlin and M. Soler, Materials Science and Engineering A 355 (2003) 299.

[3] A. Brahmi and R. Borrelly, Acta Materialia 45 (1997) 1889.

[4] B. T. N. Gao N. , ISIJ International 37 (1997) 8.

[5] B. T. N. Gao N. , ISIJ International 38 (1998) 7.

[6] R. Lagneborg, T. Siwecki, S. Zajac and B. Hutchinson, Scandinavian Journal of Metallurgy 28 (1999) 55.

[7] H. R.W.K. and B. H.K.D.H., Steels Microstructure and properties, (Edward Arnold, London, 1995).

[8] R. E. Reed-Hill and R. Abbaschian, Physical metallurgy principles / (PWS Pub. Co., boston, 1994).

[9] B. Predel, Physical chemistry, Phase equilibria, crystallographic and thermodynamic data of binary alloys (Springer-Verlag, Berlin, 1998).

[10] J. R. Bradley and H. I. Aaronson, Metallurgical Transactions a-Physical Metallurgy and Materials Science 12 (1981) 1729.

[11] M. Hillert and B. Sundman, Acta Metallurgica 24 (1976) 731.

[12] H. I. Aaronson, W. T. Reynolds and G. R. Purdy, Metallurgical and Materials Transactions a-Physical Metallurgy and Materials Science 35A (2004) 1187.

[13] C. R. Hutchinson, H. S. Zurob and Y. Brechet, Metallurgical and Materials Transactions a-Physical Metallurgy and Materials Science 37A (2006) 1711.

[14] H. I. Aaronson and H. A. Domian, Transactions of the Metallurgical Society of Aime 236 (1966) 781.

[15] M. Enomoto, Metallurgical and Materials Transactions a-Physical Metallurgy and Materials Science 37A (2006) 1703.

[16] H. Guo, G. R. Purdy, M. Enomoto and H. I. Aaronson, Metallurgical and Materials Transactions a-Physical Metallurgy and Materials Science 37A (2006) 1721.

[17] H. I. Aaronson, W. T. Reynolds and G. R. Purdy, Metallurgical and Materials Transactions a-Physical Metallurgy and Materials Science 37A (2006) 1731.

[18] F. G. Wilson and T. Gladman, International Materials Reviews 33 (1988) 221.

[19] T. Gladman and Pickerin.Fb, Journal of the Iron and Steel Institute 205 (1967) 653.

[20] T. Gladman, The physical metallurgy of microalloyed steels
(Institute of Materials, London 1997).

[21] T. Nakayama and N. Honjou, Magnetism and Magnetic Materials 213 (2000) 87.

[22] A. Saxena and S. K. Chaudhuri, Isij International 44 (2004) 1273.

[23] A. Saxena, A. Sengupta and S. K. Chaudhuri, Isij International 45 (2005) 299.

[24] W. C. Jeong, Metallurgical and Materials Transactions a-Physical Metallurgy and Materials Science 37 (2006) 3737.

[25] W. C. Jeong, Metallurgical and Materials Transactions a-Physical Metallurgy and Materials Science 40A (2009) 1280.

[26] B. Mintz, S. Yue and J. J. Jonas, International Materials Reviews 36 (1991) 30.
[27] M. F. Eldridge, in "IMR" (Leeds, Leeds, 2000).
[28] K. R. Kinsman and H. I. Aaronson, Metallurgical Transactions 4 (1973) 959.
[29] G. W. D. Mintz B., Su H. , materials Science and Technology (In press).
[30] M. F. Eldridge and R. C. Cochrane, Materials Science Forum 284-286 (1998) 7.
[31] J. E. Morral and T. B. Cameron, Boron hardenability mechanisms, in "Boron Steel, Proc. Int. Symp" (Metall. Soc. AIME, CT, USA, 1979).
[32] H. Mabuchi and T. Koseki, Isij International 40 (2000) 809.
[33] H. Mabuchi and R. Uemori, Isij International 38 (1998) 203.
[34] H. Mabuchi, R. Uemori and T. Koseki, Isij International 39 (1999) 937.
[35] H. Peng, X. Song, A. Gao and X. Ma, Materials Letters 59 (2005) 3330.
[36] X. Li, A. Watson, R. Brydson, A. Jha and R. C. Cochrane, Journal of Materials Science 35 (2000) 1051.
[37] N. H. Mabuchi H., ISIJ International 7 (1981) 6.
[38] N. H. Mabuchi H., ISIJ International 6 (1983) 8.
[39] B. Mintz, A. Williamson, H. Su and W. B. Morrison, Materials Science and Technology 23 (2007) 63.
[40] G. Frommeyer, E. J. Drewes and B. Engl, Revue de Metallurgie 97 (2000) 8.
[41] V. F. Zackay and E. R. Parker, Journal of Basic Engineering 89 (1967) 4.
[42] G. R. Chanani, V. F. Zackay and E. R. Parker, Metallurgical Transactions 2 (1971) 6.
[43] L. Zhao, J. Sietsma and S. Van der Zwaag, Phase transformations and microstructural evolution in aluminum-containing TRIP steels, in "EUROMAT 99" (Wiley-VCH Verlag GmbH, Weinheim, Germany, Munich, Germany, 1999).
[44] K.-i. Sugimoto, B. Yu, Y.-i. Mukai and S. Ikeda, ISIJ International 45 (2005) 6.
[45] S. C. P. Baik, Sung-Ho; Kwon, Ohjoon; Kim, Dong-Ik; Oh, Kyu Hwan, ISIJ International 46 (2006) 6.
[46] E. Girault, A. Mertens, P. Jacques, Y. Houbaert, B. Verlinden and J. Van Humbeeck, Scripta Materialia 44 (2001) 885.
[47] O. Grassel, L. Kruger, G. Frommeyer and L. W. Meyer, International Journal of Plasticity 16 (2000) 1391.
[48] H. Ding, Z. Y. Tang, W. Li, M. Wang and D. Song, Journal of Iron and Steel Research International 13 (2006) 66.
[49] B. K. Zuidema, D. K. Subramanyam and W. C. Leslie, Metallurgical Transactions a-Physical Metallurgy and Materials Science 18 (1987) 1629.
[50] H. J. Lai and C. M. Wan, Journal of Materials Science 24 (1989) 2449.
[51] F. C. Chen, C. P. Chou, P. Li and S. L. Chu, Materials Science and Engineering a-Structural Materials Properties Microstructure and Processing 160 (1993) 261.
[52] C. G. de Andres, F. G. Caballero, C. Capdevila and L. F. Alvarez, Materials Characterization 48 (2002) 101.
[53] C. G. de Andres, F. G. Caballero, C. Capdevila and D. San Martin, Materials Characterization 49 (2002) 121.
[54] W. W. Mullins, Journal of Applied Physics 28 (1957) 333.
[55] E. Rabkin and L. Klinger, Materials Science and Technology 17 (2001) 772.
[56] P. J. Goodhew, Thin foil preparation for Electron microscopy (Elsevier Science Oxford, 1985).

[57] A. F. Gourgues-Lorenzon, International Materials Reviews 52 (2007) 65.
[58] L. Ryde, Materials Science and Technology 22 (2006) 1297.
[59] P. J. Goodhew, J. Humphreys and B. Richard, Electron microscopy and analysis (Taylor & Francis, London, 2001).
[60] R. Bengochea, B. Lopez and I. Gutierrez, Metallurgical and Materials Transactions a-Physical Metallurgy and Materials Science 29 (1998) 417.
[61] R. Bengochea, B. Lopez and I. Gutierrez, Isij International 39 (1999) 583.
[62] R. Priestner and A. K. Ibraheem, in Materials Congress 2000 (I O M Communications Ltd Inst Materials, Cirencester, England, 2000) p. 1267.
[63] R. Priestner and P. D. Hodgson, Materials Science and Technology 8 (1992) 5.
[64] S. Piazolo, V. G. Sursaeva and D. J. Prior, Optical grain size measurements: What is being measured? Comparative study of optical and EBSD grain sizes determination in 2D AI foil, in "Icotom 14: Textures of Materials, Pts 1and 2" (2005) p. 213.
[65] F. J. Humphreys, Journal of Microscopy-Oxford 195 (1999) 170.
[66] N. Gao, S. C. Wang, H. S. Ubhi and M. J. Starink, Journal of Materials Science 40 (2005) 4971.
[67] J. A. Small and J. R. Michael, Journal of Microscopy-Oxford 201 (2001) 59.
[68] J. K. Mackenzie, Biometrika 45 (1958) 229.
[69] Thermodynamics and Phase Equilibrium Software, (the National Physical Laboratory).
[70] W. B. C. Morrison, J. A., Controlled rolling, in "Br. Steel Corp., Open [Rep.]" (Br. Steel, Sheffield 1975) p. 20.
[71] F. Vodopivec, M. Gabrovsek, M. Kmetic and A. Rodic, Metals Technology 11 (1984) 481.
[72] B. Eghbali, Materials Letters 61 (2007) 4006.
[73] K. J. Albutt and S. Garber, Journal of the Iron and Steel Institute 204 (1966) 1217.
[74] G. R. Speich, A. Szirmae and M. J. Richards, Transactions of the Metallurgical Society of Aime 245 (1969) 1063.
[75] C. I. Garcia and A. J. Deardo, Metallurgical Transactions a-Physical Metallurgy and Materials Science 12 (1981) 521.
[76] G. R. Speich, V. A. Demarest and R. L. Miller, Metallurgical Transactions a-Physical Metallurgy and Materials Science 12 (1981) 1419.
[77] E. Navara and R. Harrysson, Scripta Metallurgica 18 (1984) 605.
[78] F. G. Caballero, C. Capdevila and C. G. De Andres, Metallurgical and Materials Transactions a-Physical Metallurgy and Materials Science 32 (2001) 1283.
[79] T. Akbay, R. C. Reed and C. Atkinson, Acta Metallurgica Et Materialia 42 (1994) 1469.
[80] C. Atkinson, T. Akbay and R. C. Reed, Acta Metallurgica Et Materialia 43 (1995) 2013.
[81] F. G. Caballero, C. Capdevila and C. G. De Andres, Journal of Materials Science 37 (2002) 3533.
[82] F. G. Caballero, C. Capdevila and C. G. De Andres, Isij International 41 (2001) 1093.
[83] F. G. Caballero, C. Capdevila and C. G. De Andres, Isij International 43 (2003) 726.
[84] D. San Martin, T. de Cock, A. Garcia-Junceda, F. G. Caballero, C. Capdevila and C. G. de Andres, Materials Science and Technology 24 (2008) 266.

[85] D. San Martin, P. E. J. Rivera-Diaz-Del-Castillo and C. Garcia-de-Andres, Scripta Materialia 58 (2008) 926.
[86] M. M. Souza, J. R. C. Guimaraes and K. K. Chawla, Metallurgical Transactions a-Physical Metallurgy and Materials Science 13 (1982) 575.
[87] N. Pussegoda, W. R. Tyson, P. Wycliffe and G. R. Purdy, Metallurgical Transactions a-Physical Metallurgy and Materials Science 15 (1984) 1499.
[88] C. G. de Andres, F. G. Caballero and C. Capdevila, Scripta Materialia 38 (1998) 1835.
[89] D. P. Datta and A. M. Gokhale, Metallurgical Transactions a-Physical Metallurgy and Materials Science 12 (1981) 443.
[90] S. K. Jayaswal and S. P. Gupta, Zeitschrift Fur Metallkunde 83 (1992) 809.
[91] F. G. Caballero, C. Capdevila and C. G. de Andres, Scripta Materialia 42 (2000) 1159.
[92] A. Roosz, Z. Gacsi and E. G. Fuchs, Acta Metallurgica 31 (1983) 509.
[93] V. I. Savran, Y. Van Leeuwen, D. N. Hanlon, C. Kwakernaak, W. G. Sloof and J. Sietsma, Metallurgical and Materials Transactions a-Physical Metallurgy and Materials Science 38A (2007) 946.
[94] V. I. Zeldovich, I. V. Khomskaya and O. S. Rinkevich, Fizika Metallov I Metallovedenie (1992) 5.
[95] J. Lis, A. Lis and C. Kolan, Materials Characterization 59 (2008) 1021.
[96] S. J. Sun and M. Pugh, Materials Science and Engineering a-Structural Materials Properties Microstructure and Processing 276 (2000) 167.
[97] A. D. Romig and R. Salzbrenner, Scripta Metallurgica 16 (1982) 33.
[98] J. Y. Koo, M. Raghavan and G. Thomas, Metallurgical Transactions a-Physical Metallurgy and Materials Science 11 (1980) 351.
[99] M. Amirthalingam, M. Hermans and I. Richardson, Metallurgical and Materials Transactions a-Physical Metallurgy and Materials Science 40A (2009) 901.
[100] S. Maropoulos, S. Karagiannis and N. Ridley, Journal of Materials Science 42 (2007) 1309.
[101] C. S. Lee, K. A. Lee, D. M. Li, S. J. Yoo and W. J. Nam, Materials Science and Engineering a-Structural Materials Properties Microstructure and Processing 241 (1998) 30.
[102] W. J. Nam, C. S. Lee and D. Y. Ban, Materials Science and Engineering a-Structural Materials Properties Microstructure and Processing 289 (2000) 8.
[103] C. Zener, Journal of Applied Physics 20 (1949) 950.
[104] Q. B. Yu and Y. Sun, Materials Science and Engineering a-Structural Materials Properties Microstructure and Processing 420 (2006) 34.
[105] J. Barford and W. S. Owen, Journal of the Iron and Steel Institute 200 (1962) 49.
[106] C. Capdevila, F. G. Caballero and C. G. de Andres, Materials Transactions 44 (2003) 1087.
[107] Y. C. Liu, F. Sommer and E. J. Mittemeijer, Acta Materialia 51 (2003) 507.
[108] Y. C. Liu, D. J. Wang, F. Sommer and E. J. Mittemeijer, Acta Materialia 56 (2008) 3833.
[109] G. F. V. Voort, Metallography: principles and practice (McGraw-HillBook Company N.Y. USA, 1984).
[110] Y. C. Liu, F. Sommer and E. J. Mittemeijer, Acta Materialia 52 (2004) 2549.
[111] Y. C. Liu, F. Sommer and E. J. Mittemeijer, Acta Materialia 54 (2006) 3383.
[112] Y. C. Liu, F. Sommer and E. J. Mittemeijer, Metallurgical and Materials Transactions a-Physical Metallurgy and Materials Science 39A (2008) 2306.

[113] E. Kozeschnik and E. Gamsjager, Metallurgical and Materials Transactions a-Physical Metallurgy and Materials Science 37A (2006) 1791.
[114] F. Liu, F. Sommer, C. Bos and E. J. Mittemeijer, International Materials Reviews 52 (2007) 193.
[115] J. W. Christian, The Theory of Transformation in Metals and Alloys (Pergammon Press 1975).
[116] M. Avrami, Journal of Chemical Physics 7 (1939) 1103.
[117] C. G. de Andres, C. Capdevila, D. San Martin and F. G. Caballero, Journal of Materials Science Letters 20 (2001) 1135.
[118] J. B. Gilmour, G. R. Purdy and J. S. Kirkaldy, Metallurgical Transactions 3 (1972) 3213.
[119] T. Tanaka, H. I. Aaronson and M. Enomoto, Metallurgical and Materials Transactions a-Physical Metallurgy and Materials Science 26 (1995) 561.
[120] M. Enomoto and H. I. Aaronson, Metallurgical Transactions a-Physical Metallurgy and Materials Science 17 (1986) 1385.
[121] K. P. Mingard, B. Roebuck, E. G. Bennett, M. Thomas, B. P. Wynne and E. J. Palmiere, Journal of Microscopy-Oxford 227 (2007) 298.
[122] F. J. Humphreys, Journal of Materials Science 36 (2001) 3833.
[123] D. San Martín, Y. Palizdar, R. C. Cochrane, R. Brydson and A. J. Scott, Materials Characterization 61 (2010) 584.

Appendix 1

A Comparative Study of Steel Microstructure Using EBSD and Metallography

Introduction

It is well known that the mechanical and physical properties of metallic materials are frequently related to grain size via the Hall-Petch relationship where strength is inversely dependant on the square root of the grain size. The size and shape of grains are generally determined through optical or scanning electron microscopy of etched samples. These methods utilize the fact that grain boundaries (GB) can be made visible through careful etching. The underlying concept of such grain size measurements, assumes that GBs are etched to different degrees depending on their energy which is generally thought to be directly related to misorientation angle. Thus, a grain is defined as an area that is surrounded by etched boundaries of a specific minimum misorientation angle and energy. It should be noted that during metallographic investigation in the optical microscopy, the low energy grain boundaries produce weak contrast and are practically difficult to observe. Moreover, it is generally not known what is the minimum misorientation angle above which boundaries will be etched and below which they are not. Also, the etching procedure may vary slightly from sample to sample. In addition to metallography, EBSD is increasingly becoming one of the main characterisation techniques for the investigation of crystalline materials. The development of the EBSD technique began in 1973 with Venable and Harland introducing a new diffraction technique in a scanning electron microscopy (SEM) and continued with semiautomatic indexing in 1983 by Dingley et. al. Many of the structural parameters that control the properties and performance of materials can be derived from EBSD data e.g. grain size, phase constituents, misorientation distribution and microtexture which gives data for modelling and prediction of mechanical anisotropy and residual strain [1]. There is little in the literature comparing the relative merits and quantitative results of grain size measurements obtained with light microscopy and EBSD. In the present work the authors compare the grain sizes obtained by both standard metallography and EBSD.

Experimental

To obtain the grain size the metallography specimens of three investigated steels were polished and etched with 2% nital. The specimens were examined using a Nikon Optiphot reflected light microscope. Images were captured using a CCD camera and Zeiss Axiovision software. The average grain size was determined using the linear intercept method.

The relative error (E) in determining the grain size using the linear intercept method is related to the number of grains (n) by:

$$E = 0.7/n^{1/2} \qquad \text{(Equation 1) [2]}$$

A minimum of 1000 boundaries were measured for each specimen giving a precision of approximately 2%.

The samples were prepared for EBSD by polishing on a Buehler Vibromat vibratory polisher using non-crystallising colloidal silica. EBSD was then carried out using a Zeiss Leo FEGSEM with patterns detected using an Oxford Instruments camera. Patterns were analysed in real time using INCA software from Oxford Instruments. Maps were collected for each sample using a step size of approximately 0.7 μm.

Results and discussion

The metallography images of samples E, F and G are given in Fig. 1. It should be noted that several factors such as selected minimum grain boundary misorientation angle, analysis step size and also the minimum number of pixels deemed necessary to define a grain can all affect the grain size number obtained by EBSD [3-5].

Due to the size of the ferrite grains in the steel samples, we have assumed that the variation of step size and also the minimum number of pixels to define a grain will not greatly influence the grain size obtained by EBSD. However, it is believed that the selected minimum grain boundary misorientation angle can significantly affect the grain size. A grain is defined as an area completely surrounded by boundaries which have a misorientation greater than the selected minimum grain boundary misorientation angle. Different defined minimum misorientation angles give different

grain sizes and consequently different grain size distributions. The minimum misorientation angle was varied to obtain a grain size similar to that obtained by the standard metallographic methods. At present, there is little information in the literature about comparing these two methods for grain size measurement and no specific standard.

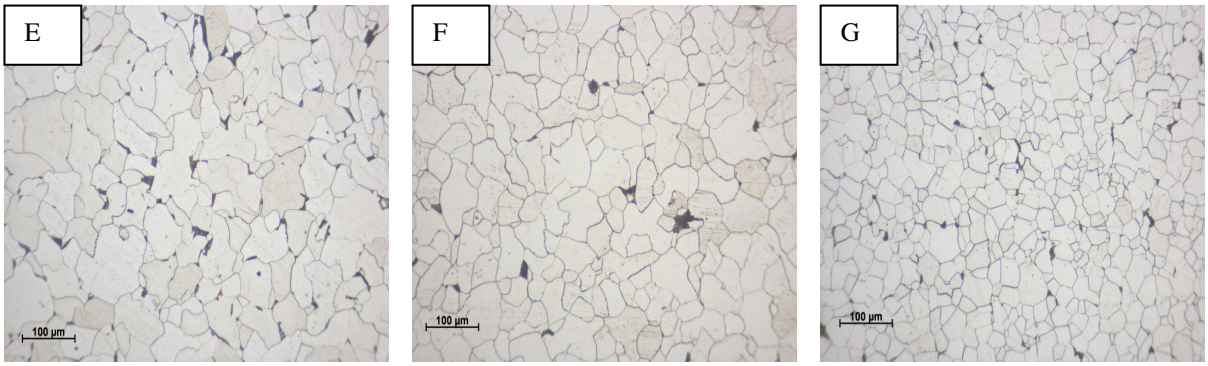

Figure 1: Optical micrographs of steels E (0.02 wt% Al), F (0.48 wt%Al) and G (0.94 wt% Al)

Figure 2 shows the EBSD grain maps for each sample as a function of minimum grain boundary misorientation angle for cut offs of 5º and 12º. Mean linear intercept and grain size measurements, determined using optical microscopy and EBSD, are shown in Table 1. The errors for the grain size are calculated using equation 1 and indicated in brackets.

Table 1: Grain size determination by EBSD and optical microscopy

EBSD misorientation angle	A	B	C
3˚	27 µm	25 µm	20 µm
5˚	28 µm	29 µm	21 µm
8˚	29 µm	30 µm	22 µm
10˚	31 µm	31 µm	23 µm
12˚	33 µm	32 µm	23 µm
14˚	34 µm	33 µm	24 µm
16˚	34 µm	33 µm	25 µm
Metallography	33 µm (+/- 0.5)	32 µm (+/- 0.5)	23 µm (+/- 0.5)

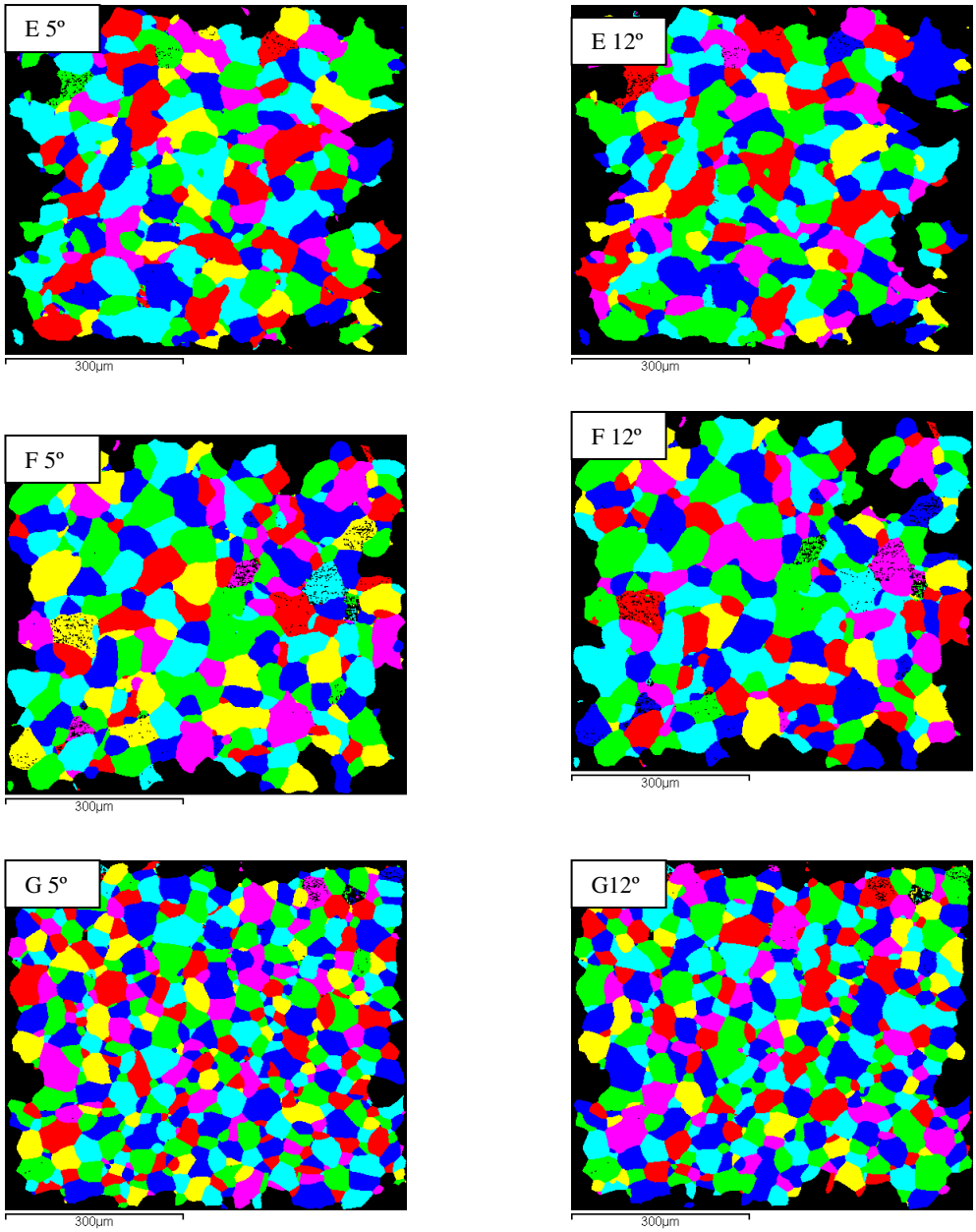

Figure 2: EBSD grain maps for each steel as a function of minimum grain boundary misorientation angle

The results show that grain sizes obtained using EBSD correspond most closely to optical microscopy results where the EBSD misorientation angle cut off is between 10º and 12º. This implies that in standard metallography grain size measurement we can reveal grain boundaries with more than 10º misorientation. It should be mentioned that results obtained in this study are in agreement with the results achieved by Piazolo and his co-worker [4]. They examined the effect of misorientation angle on grain size determination by EBSD and compared their results with metallography data for an aluminum alloy. However, it should be noted that our results are not in agreement with those of Gao et al work for steel [5]. They

concluded that EBSD grain size measurements are more accurate those obtained by conventional imaging methods and give smaller average grain sizes. However, as seen in Table 1, grain size results depends on the selected misorientation angle cut off and at times a coarser grain size may be achieved.

Conclusion

EBSD is becoming one of the main characterisation techniques for crystalline materials. However, it needs to be standardized if we are able to compare results with other established methods when for example obtaining grain size information. We have shown that careful analysis of the EBSD data is necessary, in particular when defining the minimum grain boundary misorientation angle, if we want to compare results with those obtained using metallography. For low carbon hot rolled steel, it was found that 10º to 12º cut off misorientation angle would be the best condition to compare the metallography and EBSD results.

References

1) A.F. GOURGUES-LORENZON, Int. Mater. Rev., 52, (2007), p.62.
2) T. GLADMAN, The physical metallurgy of microalloyed steels, Institute of Materials, London (1995).
3) K.P.MINGARD, B. ROEBUCK, E. G. BENNETT, M. THOMAS, B. P. WYNNE and E. J. PALMIERE, J. Microsc.227, (2007), p.298.
4) S. PIAZOLO, V. G. SURAEVA and D. J. PRIOR, Mater. Sci. Forum, 495-497, (2005), p.213.
5) N.GAO, S. C. WANG, H.S.UBHI and M. J. STARINK, Mater. Sci., 40, p. 4971.

Appendix 2

Accurate Analysis of EBSD Data for Phase Identification

Introduction

Electron backscatter diffraction (EBSD) in the scanning electron microscope (SEM) is now a well established technique for examination of the crystallographic microstructure of single and multiphase materials [1]. The ability to rapidly analyse large areas of samples and the ease of specimen preparation when compared to transmission electron microscopy (TEM) is a major advantage promoting its use. However, in certain instances it can be difficult to detect and differentiate second phases which may be present in small amounts, especially when present as small or finely dispersed particles.

It should be noted that EBSD is becoming an increasingly popular characterisation technique with many researchers inexperienced in this area. It is well known that optimisation of hardware and the microscope set up such as accelerating voltage, specimen tilt and probe size together with good sample preparation are essential to obtain good quality results [1, 2]. Since EBSD data analysis is computer based to obtain reliable and accurate results we must pay particular attention to certain processing parameters such as the minimum number of indexed bands and the maximum solution error, questioning the given default values. The maximum solution error is a measure of the allowed angular error between the collected and predicted patterns i.e. the pixel will be unindexed if the angle between the pattern and solution is greater than the selected maximum solution error). In this paper the effect of these parameters on the EBSD results will be discussed.

Experimental Methods

A series of EBSD investigations were designed and carried out on a steel F. The samples were prepared for EBSD by polishing on a Buehler Vibromat vibratory polisher using non-crystallising colloidal silica. EBSD was then carried out using a Carl Zeiss SMT Leo 1530 FEG-SEM operated at 30 kVFEGSEM from the centre of specimens with patterns detected using an Oxford Instruments camera. Patterns were analysed in real-time using the INCA software from Oxford Instruments. Maps were

collected using different step sizes from approximately 2 μm down to 100 nm. To investigate the size of AlN particles, TEM has been employed. AlN particles were extracted by the carbon replica technique and examined using a Philips CM20 TEM operated at 200 kV.

Results and discussion

EBSD pattern quality and phase maps were obtained at different levels of magnification using step sizes of approximate 2, 0.5 and 0.1μm, with analysis for the expected phases of ferrite, cementite and AlN; these are shown in figures 1a-c respectively.

The default settings of the INCA crystal software were used with the minimum number of bands for indexing being 5 and the maximum solution error 2 degrees. The microstructure is indexed as being fully ferritic with some AlN and cementite particles.

The corresponding pattern quality maps are shown to be of high quality. The AlN particle distributions look feasible since thermodynamic calculations performed using either the equation proposed by Seiverts [3] or the Thermocalc software suggest that the solvus temperature of aluminium nitride for this specific composition would not be lower than 1250 ºC.

This suggests that relatively large AlN particles should be expected within the bulk. In addition, TEM shows the AlN particle size to be approximately 500 nm (Fig. 2). Therefore in theory, EBSD results obtained using a 100 nm step size can be expected to be reliable since at this step size there would be more than 4 pixels covering one particle which facilitate the phase identification process. The other issue which needs to be considered is spot size. However, since EBSD has been performed using a FEGSEM, the spot size and consequently special resolution is small.

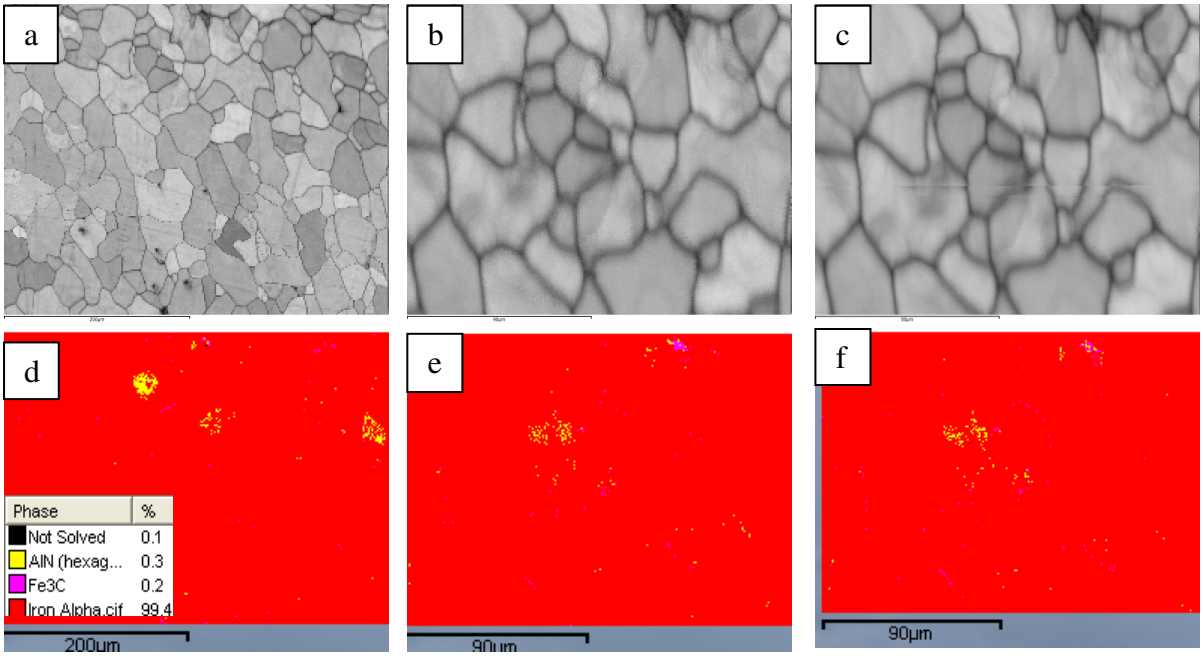

Figure 1. Pattern quality maps with expected phases of ferrite, cementite and AlN. The minimum number of bands and maximum error are the default settings of 5 and 2 respectively. Approximate 2 µm step size applied for "a" and "d" and 0.5 and 0.1 performed for "b" and "e" and "c" and "f" respectively.

Following the EBSD analysis of the steel which indicated the presence of AlN, both EDX mapping and backscattered imaging within the SEM were employed to add further confirmation. However, no contrast indicative of the presence of different phases within the ferrite matrix was found by BS-SEM and also no aluminium was detected using EDX. This could be attributed to the poor spatial resolution for both backscattered imaging and EDX analysis but since the attempt to show the presence of AlN by back scatter imaging and EDX technique did not succeed it was thought that more investigation was required to confirm the presence of AlN.

To examine the reliability of the EBSD results, reprocessing of the data was performed with analysis solely for the phases, ferrite and cementite. However, the pixels previously indexed as AlN do not now appear as unindexed points but are indexed as ferrite. This could be the consequences of overlapping two patterns. On the other hand, it could be an indication of using inappropriate tolerances when processing the EBSD data. To examine the suitability of the default tolerances, the raw data were reprocessed with the expected phases being Al_3Ni_2, Al_3Zr and the

silicate mineral, Augite; these “nonsense” phases possess a range of different crystal structures and are most definitely not present in the sample. Figure 3a shows the subsequent phase map. The majority of the sampled area has been indexed as one of these three phases. Therefore, it was believed that the applied tolerances used to process the EBSD data were not tight enough to avoid mis-indexing of the data.

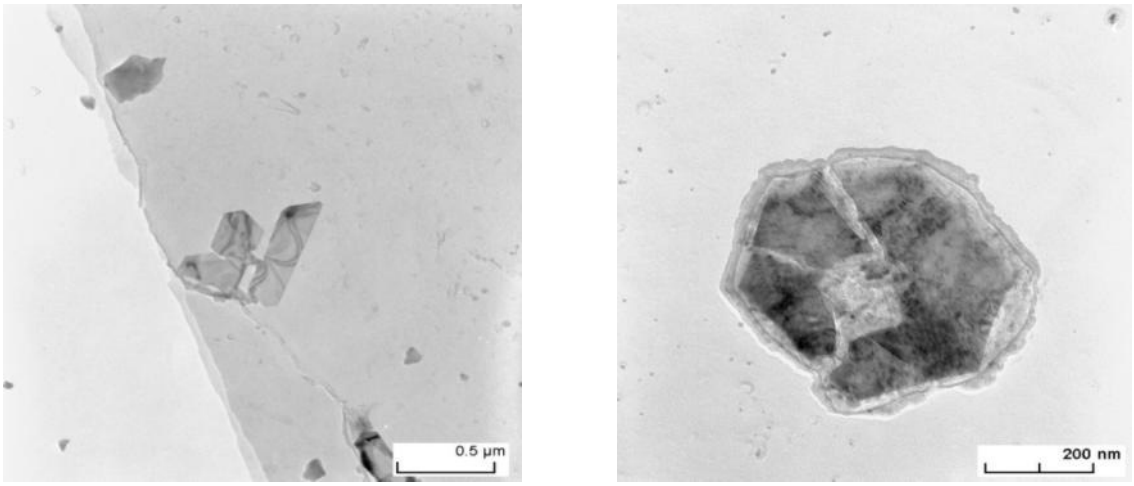

Figure 2: TEM micrograph of AlN particles

We believe that the two key parameters which can affect the accuracy of the pattern indexing are the minimum number of indexed bands and the maximum solution error. Figure 3b shows the the effect of varying these parameters on pattern indexing. As can be seen, with the minimum number of bands set to 7 and a maximum allowable error of 2^{o}, a significant number of data points are still mis-indexed, implying that the values of these parameters are insufficient to give reliable results. Increasing the number of matching bands to 9 reduces the number of mis-indexed pixels, and a further reduction is made by lowering the allowed angular error to 1.5^{o}; the number of indexed points with these inappropriate phases now falls to almost zero. However, some pixels (0.3%) are still being indexed as one of these clearly incorrect phases.

Figures 4a and 4b show the examination of the same parameters to reprocess the initial sample. Based on given results the optimum minimum indexed bands can be a range between 7 and 9 and the optimum value for maximum error solution could be around 1.5. It should be noted that after reprocessing the initial data with new

obtained criteria (9 minimum indexed band and 1.5 maximum solution error) negligible number of pixels indexed as AlN particles and also the indexed ratio fall to 95 %.

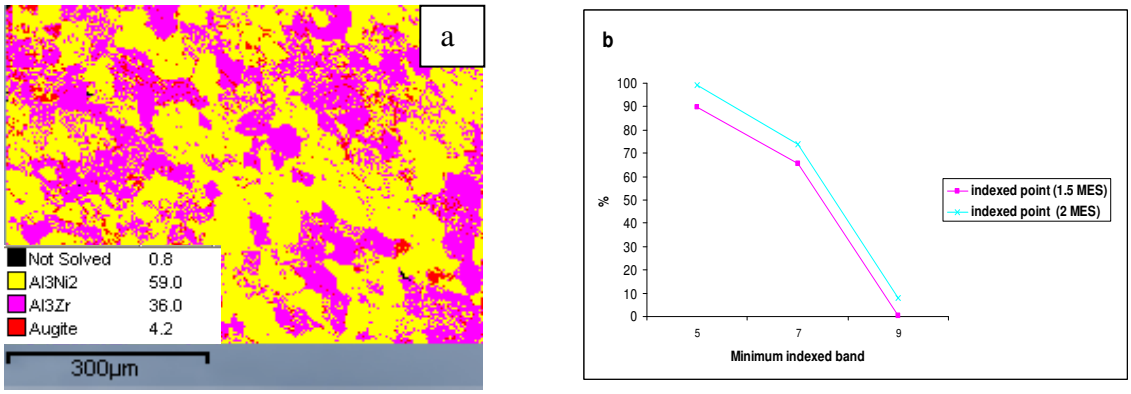

Figure 3: EBSD data reprocessed with the expected phases being Al_3Ni, Al_3Zr and Augite. Figure 3a shows reprocessed EBSD data with 5 minimum indexed bands and a maximum solution error of 2^o together with the relative assignments (% of the indexed pixels). Figure 3b shows the effect of the minimum indexed bands and maximum error solution on the percentage of indexed pixels.

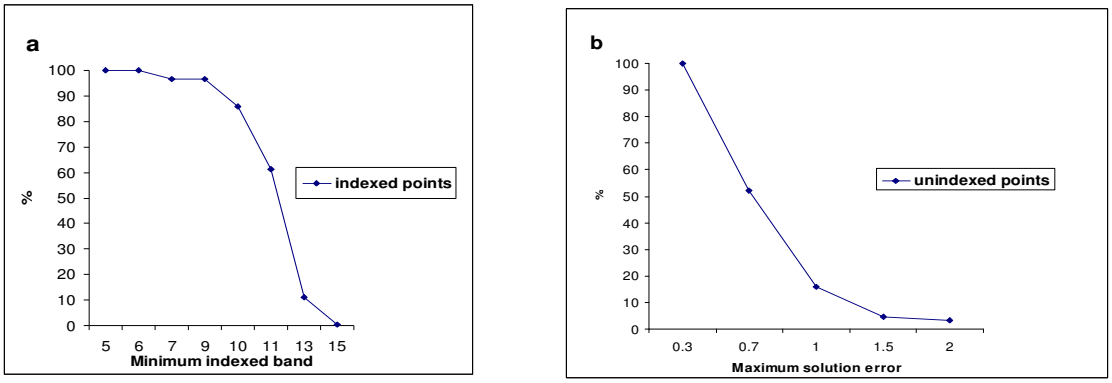

Figure 4: The effect of the minimum number of indexed bands (a) and the maximum solution error (b) on the percentage of indexed and unindexed pixels respectively as either ferrite, AlN and cementite as the expected phases.

Conclusions

The obtained results from this study show that although the importance of hardware set up cannot be ignored the used data processing criteria plays remarkable role to make the EBSD results reliable and reproducible. For instance minimum indexed band and maximum error solution play significant role to make EBSD results reproducible and reliable. Thus treating automated ESBD as a standard "package" which will provide quick and easy data is not on its own adequate to produce good quality results. In addition authors did succeed to observe the AlN distribution by ESBD while FEGSEM with 100nm step size have been used and expected AlN particle size was estimated more than 500nm.

References

1) A.F. GOURGUES-LORENZON, International Materials Reveviews,52, (2007), p 62.
2) F. J. HUMPHREYS, Journal of Materials Science 36 (2001, p 3833.
3) T. GLADMAN, The physical metallurgy of microalloyed steels, Institute of Materials, London (1997).

Appendix 3
Reliability of Thermal Etching Technique

Introduction

Austenite grain size plays significant role in determination of the microstructure and properties of steels. However it is not always easy to reveal prior austenite boundaries and consequently determine the prior austenite grain size. By considering the fact that every year some new steels are being introduced to the market, reliable procedures to reveal prior austenite grain boundaries are required.

Among different etching techniques, thermal etching methods has been shown as a reliable and relatively fast methods to reveal the prior austenite grain boundaries in carbon microalloyed steels [1] . However, this technique can be applied to any other alloy. In principles it only requires the preparation of a finely polished surface of the specimen (1 μm diamond cloth) and the application of high vacuum conditions during the heat treatment to avoid oxide formation that would darken the polished surface. Athigh temperatures, preferential diffusion takes places at the intersection of the austenite grain boundaries and the free polished surface, forming grooves of approximately 1–2 μm in width which makes prior austenite grain boundaries visible by light microscopy. After heating, slow cooling is generally preferred to fast cooling because the latter promotes the formation of surface relieves due to martensitic and/or bainitic transformations. However in certain cases, the phase transformed during cooling (ferrite, pearlite, and precipitates) can hinder/mask the prior austenite grain boundaries formed at high temperature [1, 2]. However there are always some uncertainties about the thermal etching technique and there is always a debate based on the reliability of the obtained results from this techniques.

As a part of research concerning the effect of Al as a solid solution on the steel microstructure, it was required to determine the prior austenite grain size. Chemical etching with different etchants was applied to the investigated steels but the results obtained were not satisfactory. Thermal etching was employed and the result achieved was promising. However, there were still some uncertainties regarding the reliability of the technique practically whether it is possible to associate each groove with prior austenite boundary and whether the boundaries are still connected to the

groove or not. To tackle these issues a series of experiments were designed and some thermally etched boundaries were examined by different techniques such as AFM, confocal light microscopy and combination of FIB and TEM examination.

Experimental methods

To investigate the reliability of thermal etching technique, a thermally etched sample was prepared at 1170 °C from steel G. The heating cycles preformed and also other experimental details can be found in chapter 6, however instead of slow cooling, sample was quenched after revealing austenite boundary at 1170 ºC. The main concern regarding this technique is whether each groove can be associated with one boundary. In other words, whether we can consider each groove as representative of a single grain boundary and whether a "real" boundary exists underneath or the grooves are some topographies on the surface which sometimes do not have any connection with the real grain boundaries. One way that those uncertainties regarding this technique can be studied, is to prepare FIB sections from randomly selected boundaries and reveal what lies underneath of the polished surface and then show whether there is a relationship between the surface grooves and grain boundaries or not. Therefore a number of grain boundaries were selected and FIB sections were prepared from them. Details of FIB sectioning process can be found in chapter 5.

The other technique that can indirectly confirm that each groove is representative of one boundary is EBSD. By undertaking EBSD on thermally etched samples and superimposing the obtained grain map from EBSD and light microscopy we should be able to assess the reliability of thermal etching technique.

Results and discussion

Two out of four selected boundaries are shown in figure 1. As can be seen boundaries are remarkably clear and well revealed. Figures 2 and 3 illustrate the sequence of making FIB sections from each boundary A and B respectively. Although SEM images show the clear contrast between two grains in both FIB sections, TEM was utilised to obtain more promising results to confirm the relation

between each groove and grain boundary. Figures 4 and 5 show the TEM micrographs obtained from each thermally etched boundary (A, B).

TEM examination provides clear evidence that examined grooves can be expected as representative of one boundary. In addition to FIB/TEM investigation, EBSD has been employed to somewhat indirectly relate the formed grooves to grain boundaries. Figure 6 shows EBSD grain map and misorientation map on the same selected area for FIB sectioning. As shown, obtained results from EBSD are consistence with FIB/TEM observation i.e. ESBD confirmed those obtained results from FIB/TEM observation and also it enables us to have an idea regarding the misorientation angle of examined boundary. Moreover, the well known advantage of EBSD technique is that we would be able to extend the investigated area from few micron, in FIB/TEM, to reasonably large area (500x500 μm in this case) which enables us to examine more grooves and consequently obtain more statistically correct answer regarding the relation between the formed grooves in thermal etching technique and present boundaries. Figure 7 shows the EBSD grain map results from several grains and the SEM images from the same examined area by EBSD. As can be seen, there is considerable agreement between the position of each groove and the position of grain boundary revealed by EBSD.

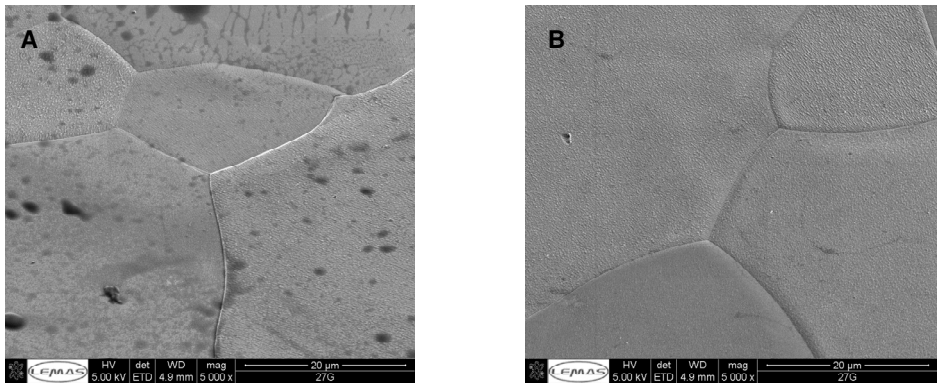

Figure 1 the SEM image of two boundaries in thermally etched samples at 1170 ºC

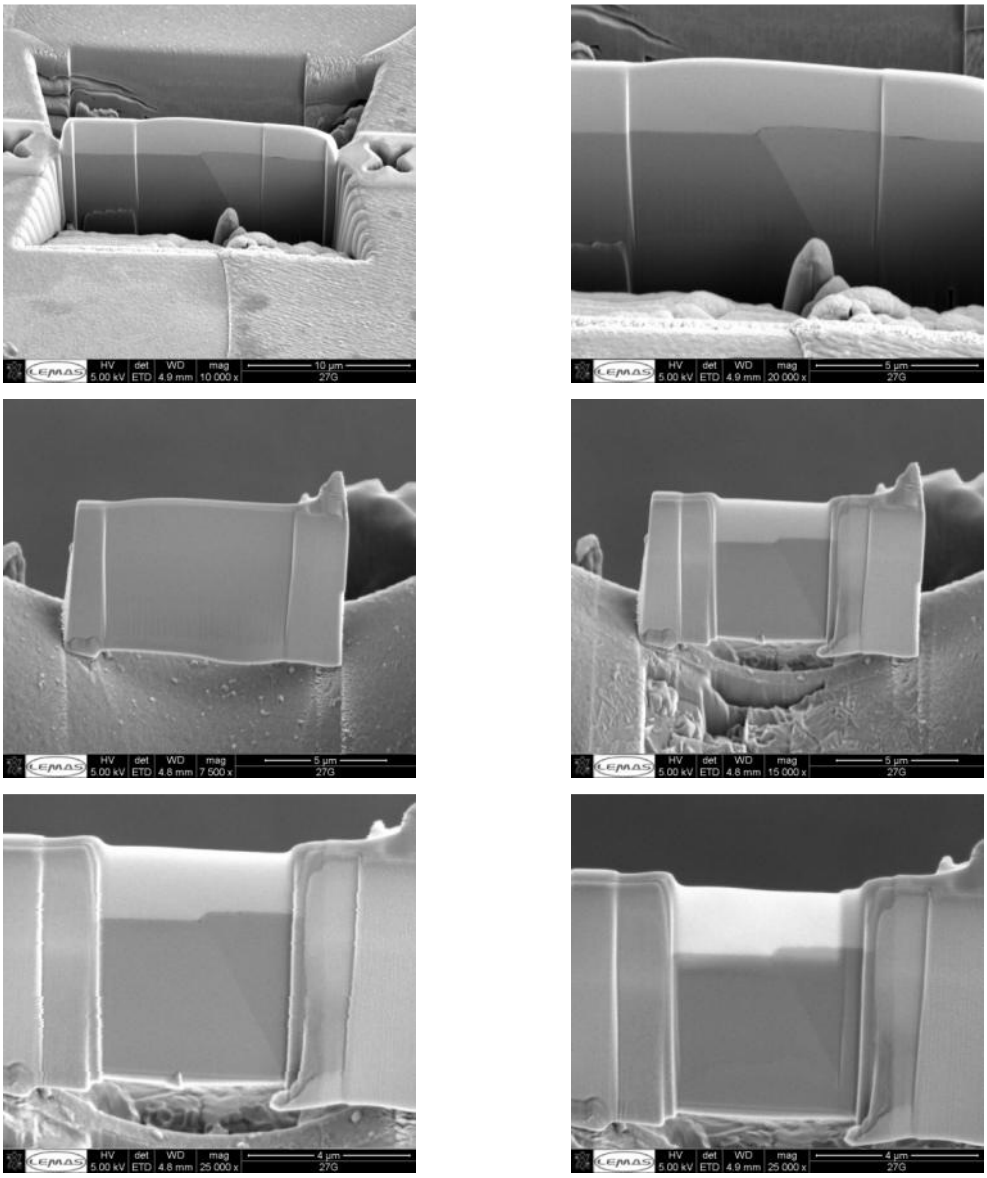

Figure 2 Sequence of preparing FIB section from boundary A

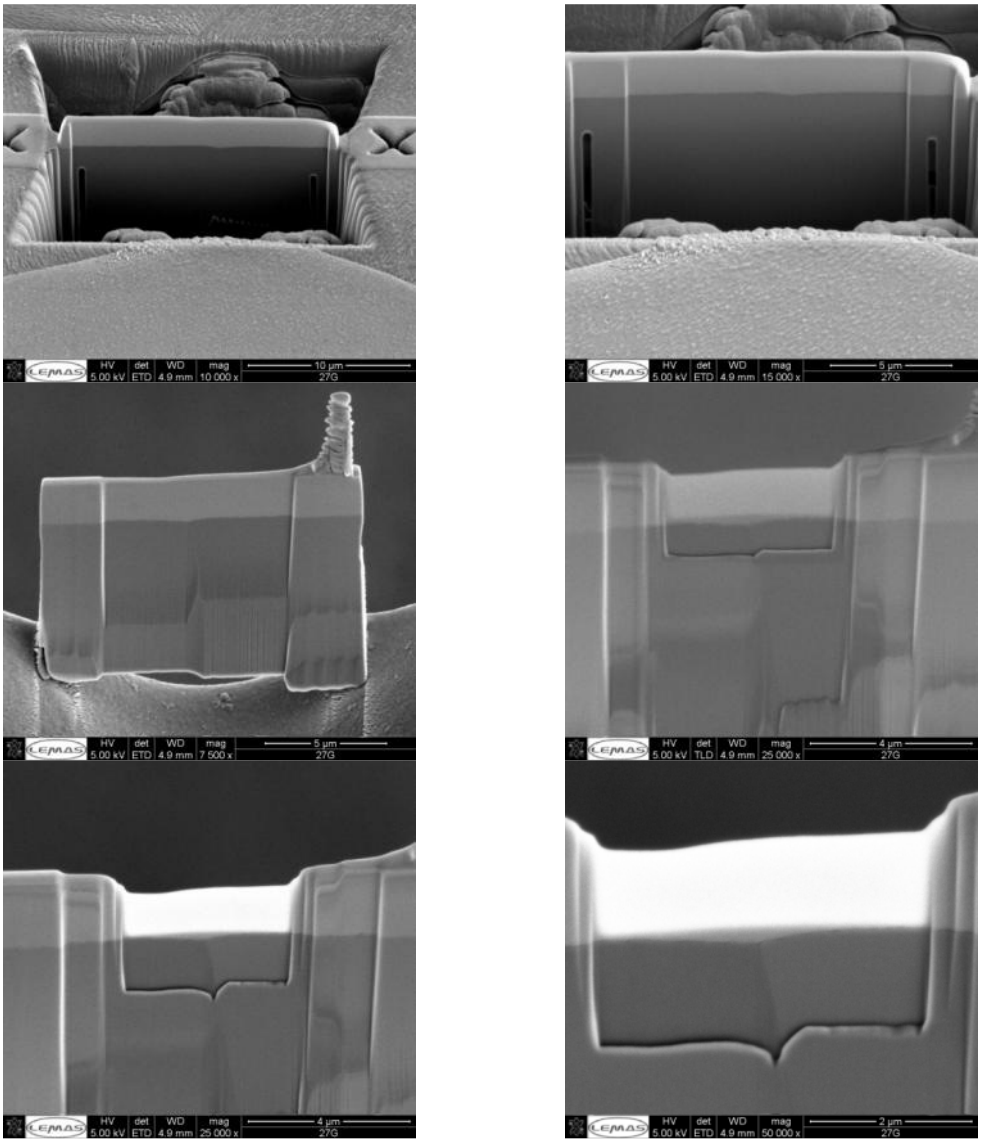

Figure 3 Sequence of preparing FIB section from boundary B

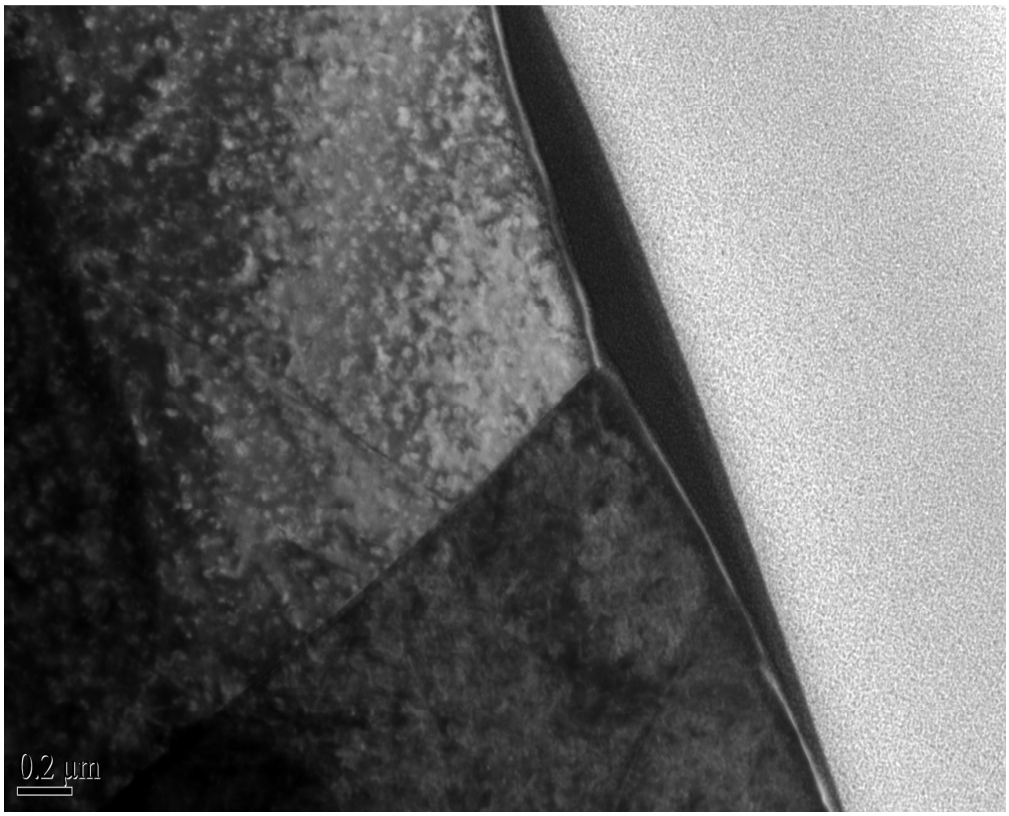

Figure 4 The TEM micrographs obtained from each thermally etched boundary A

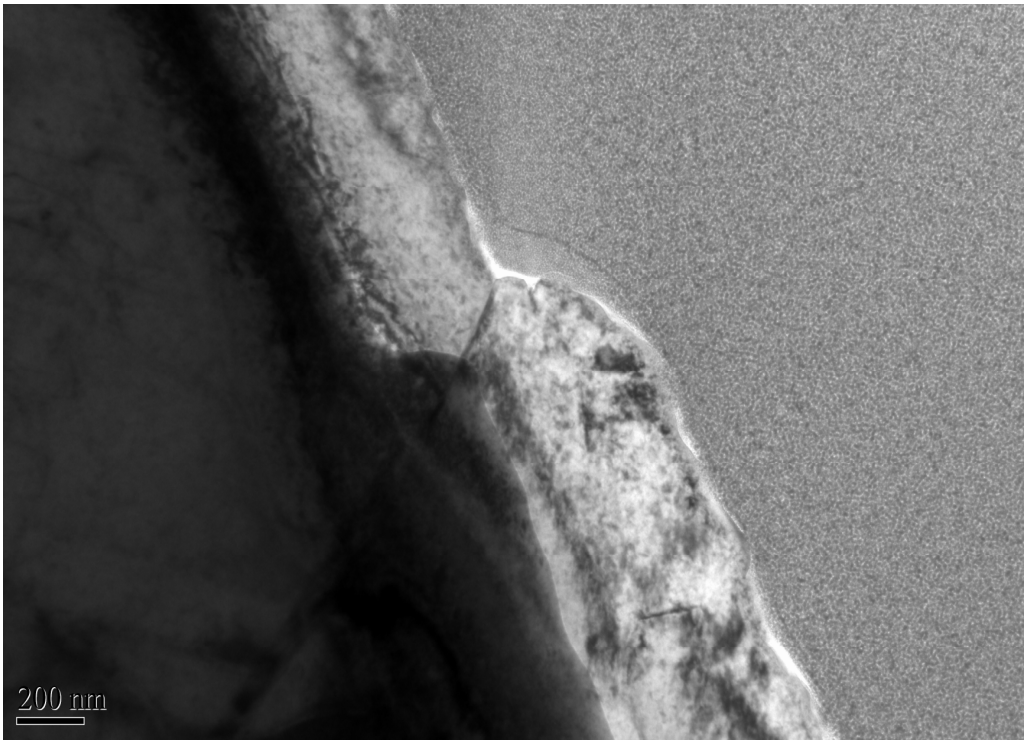

Figure 5 The TEM micrographs obtained from each thermally etched boundary B

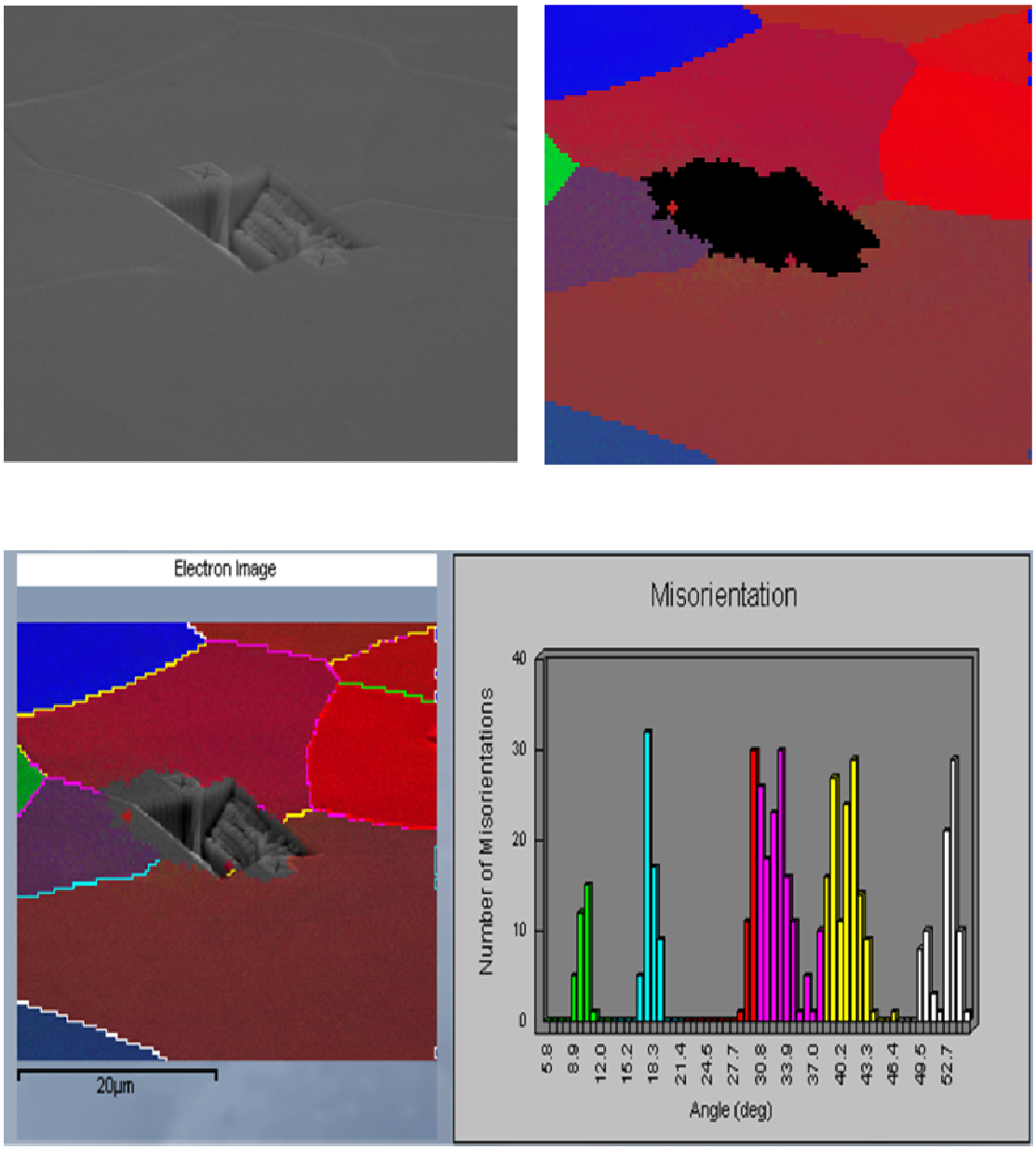

Figure 6 EBSD grain map and misorientation map on the same selected area for FIB sectioning (section A)

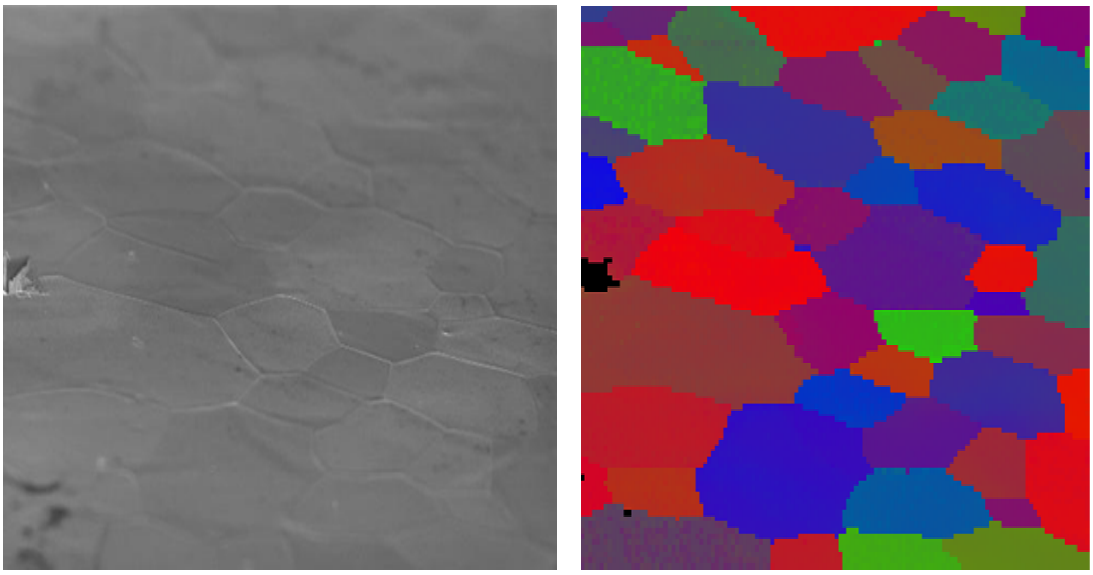

Figure 7 EBSD grain map and misorientation map on several grains

Conclusion

Although there have been always doubt concerned with the obtained austenite grain size results via thermal etching technique, using FIB/TEM in addition to EBSD demonstrated that in the investigated type of steels thermal etching is reliable and accurate way to reveal the prior austenite grain boundaries.

References

1) C. G. DE ANDRES, F. G. CABALLERO, C. CAPDEVILA, D. SAN MARTIN, Materials Characterization 49 (2002) p 121.

2) D. SAN MARTIN, Y. PALIZDAR, R. C. COCHRANE, R. BRYDSON, A. J. SCOTT, Materials Characterization 61 (2010) p 584.

Appendix 4

Reviewed Publications

Journal Publications:

- Palizdar, Y., A. J. Scott, et al. (2009). "Understanding the effect of aluminium on microstructure in low level nitrogen steels." Materials Science and Technology **25**(10): 1243-1248
- Palizdar, Y., R. C. Cochrane, et al. "The effect of deliberate aluminium additions on the microstructure of rolled steel plate characterized using EBSD." Materials Characterization **61**(2): 159-167
- San Martin, D., Y. Palizdar, et al. "Application of Nomarski differential interference contrast microscopy to highlight the prior austenite grain boundaries revealed by thermal etching." Materials Characterization **61**(5): 584-588
- Palizdar, Y., D. S. Martin, et al. "Demonstration of elemental partitioning during austenite formation in low-carbon aluminium alloyed steel." Journal of Materials Science **46**(7): 2384-2387
- San Martin, D., Y. Palizdar, et al. " Influence of aluminum alloying and heating rate on austenite formation in low carbon-manganese steels" Metallurgical & Materials Transaction A, accepted for publication
- Palizdar, Y., D. S. Martin, et al. "The effect of deliberate aluminium additions on austenite grain size in low nitrogen low carbon-manganese steel" submitted to Materials and Design

Conference Publications:

- Palizdar, Y., R. C. Cochrane, et al. (2008). "Understanding the role of aluminium in low level nitrogen steels via microstructural characterisation - art. no. 012019." Emag: Electron Microscopy and Analysis Group Conference 2007 **126**: 12019-12019
- Palizdar, Y., R. C. Cochrane, et al. "Accurate analysis of EBSD data for phase identification." Electron Micrscopy and Analysis Group Conference 2009 (Emag 2009) **241**